Title
Directed Assembly of Functionalized Carborane Analogs

Author
Auluck, Harsharn Singh

Publication Date
2015

Peer reviewed|Thesis/dissertation

UNIVERSITY OF CALIFORNIA

Los Angeles

Directed Assembly of Functionalized Carborane Analogs

A thesis submitted in partial satisfaction

of the requirements for the degree Master of Science in

Chemistry

by

Harsharn Singh Auluck

2015

ABSTRACT OF THE THESIS

Directed Assembly of Functionalized Carborane Analogs

by

Harsharn Singh Auluck

Master of Science in Chemistry

University of California, Los Angeles, 2015

Professor Paul S. Weiss, Chair

Controlling molecular building blocks and their placement at the nanoscale is an important issue for assembly from the bottom up. Manipulating single molecules on the surface using self-assembly can be used in creating novel molecular devices. Self-assembled monolayers (SAMs) form when molecules spontaneously assemble on a surface from either solution or vapor deposition. Cage molecules, specifically carboranethiols have many advantages such as rigid three-dimensional structures, high-stability to chemical and heat degradation, symmetry, rigidity, straightforward functionalization and controllable intermolecular interactions. Using the unique properties, we can fine tune SAMs and gain a fundamental chemical and physical understanding at the nanoscale. Assembling carboranethiols onto Au{111}, creates pristine monolayers with minimal defects and are made rigid through intermolecular interactions. Difunctionalized carboranes have gained interest due to the second thiol group. Assembling carboredithiol on Au{111} reveals a hexagonally close packed monolayer with two different intensity protrusions. We attribute these two protrusions as two distinct binding sites on the surface: with both thiols

bound or one thiol bound and one unbound. Controlling the directionality of these binding sites is possible through protonation. Using strong acids and bases we can direct binding modalities in either direction. Functionalizing carboranethiols provides even greater tunability over the surface. *P*-carborane and its functionalized analog, *p*-mercaptobenzoic acid are analyzed using STM. These assemblies pack in a hexagonally close packed lattice which adsorb primarily as thiolates and thiols. Contact angle measurements confirm the hydrophilic character of *p*-mercaptobenzoic acid monolayers containing the carboxylic acid group. Mixed monolayers of *p*-carborane and *p*-mercaptobenzoic acid provide an excellent foundation for two and three dimensional structures. Using STM's local barrier height (LBH) mode we can track dipoles on a surface. Assembling various carboranes with different dipoles allows us to visualize how these dipoles align and interact with neighboring molecules. Dipoles align based on intermolecular interactions with surrounding molecules and across different monolayer and surface defects, and locally align at low temperatures. Finally we look at place-exchange reactions involving alkanethiolates and alkaneselenoates through STM. Alkanthiolates are rapidly replaced by alkaneselenoates, as selenol coverage increases. The monolayer structure changes as selenoate coverage increases and with positive sample bias in STM, the selenolate-gold complex becomes labile and exchanges positions with neighboring thiolates.

.

The thesis of Harsharn Singh Auluck is approved.

William M. Gelbart

Richard B. Kaner

Paul S. Weiss, Committee Chair

University of California, Los Angeles

2015

TABLE OF CONTENTS

LIST OF ACRONYMS AND SYMBOLS

12CDT	1,2-dicarba-*closo*-dodecaboranethiol
12CDS	1,2-dicarba-*closo*-dodecaboraneselenol
912CDT	9,12-dicarba-*closo*-dodecaboranethiol
2D	two-dimensional
3D	three-dimensional
AC	alternating current
AFM	atomic force microscopy
C10	1-decanethiolate
C12	*n*-dodecanethiolate
C12Se	1-dodecaneselonolate
D12	perdeuterated dodecanethiolate
d*I*/d*V*	differential conductance spectroscopy
FTIR	fourier transform infrared spectroscopy
IETS	inelastic electron tunneling spectroscopy
IRRAS	infrared reflectance absorption spectroscopy
I/V	conductance spectroscopy
JMAK	Johnson, Mehl, Avrami, and Kolmogorov model
LBH	local barrier height
LDOS	local density of states
M1	*m*-1-carboranethiolate
O9	*o*-9-carboranethiolate
SAM	self-assembled monolayer

STM	scanning tunneling microscope
STS	scanning tunneling spectroscopy
Å	Ångström
eV	electronvolt
h	hour
I	constant-current
I_T	tunneling current
min	minute
mM	millimolar
pA	picoampere
s	second
t	time
V	volt
V_S	sample bias
z	tip-surface distance
κ	rate constant
Θ_{adv}	advancing contact angle
Θ_{rec}	receding contanct angle

LIST OF FIGURES

LIST OF TABLES

ACKNOWLEDGMENTS

I would like to begin by thanking my advisor Professor Paul Weiss for allowing me to join his lab. Through his guidance, support, and patience this work was possible. He always encouraged me when things did not work in lab. His expertise in the field of nanoscience is astounding. He always has a positive outlook on everything, even when experiments fail. His advice during group meetings was really helpful, especially on how to communicate our research effectively with various types of audiences. I am humbled and honored to have worked in his lab.

I would like to thank my thesis committee, Professors William Gelbart and Richard Kaner for their continuous support and helpful advice during my academic career. Professor Gelbart was extremely encouraging and was supportive in a time of need. Professor Kaner was immensely helpful in advising me all the way from my undergraduate years through now. I cannot thank him enough for his hospitality and support.

I would like to thank all the Weiss group members I have met in my graduate career: John C. Thomas, Dr. Nate Hohman, Dr. Sarawut Cheunkar, Dr. Shelley Claridge, David McMillan, Logan Stewart, Qing Yang, Domonic Grongzy, Andrew Serino, Garrett Wadsworth, Jeffrey Schwartz, Dr. Yuxi Zhao, Andrew Guttentag, Huan Cao, Dr. Jay Kim, Dr. Patrick Han, Miles Silverman, Dr. Bala Pathem, Dr. Yuebing Zheng, Yasuyuki Yakota, Dr. Tomáš Baše, Alexandra Mendoza, Diana Yugay, John Abendroth, Nako Nakatsuka, Kris Barr, Thomas Young, Brandon Matthews, and everyone else for sharing their knowledge and insight. Thank you everyone for providing a fun and stimulating environment to work in.

There are a few people I would especially like to thank. The first is my mentor, John C. Thomas, the UHV master. He taught me everything I know about ambient and UHV STM. With his guidance, we were able to do some interesting science. I learned a lot about how research experiments are designed and conducted under his mentorship. I would like to thank David McMillan for teaching me about machining

and instrumentation. I would like to thank Logan Stewart for pushing me and always trying my best. I would like to thank Dr. Sarawut Cheunkar for teaching me how to think about science and looking at the bigger picture. I'm thankful to have worked with you guys.

I am grateful for the support provided by the National Science Foundation, U.S. Department of Energy, the Kavli Foundation, the Chemistry and Biochemistry Department at UCLA, and the California NanoSystems Institute.

I have made so many friends during my academic career at UCLA. I want to thank all of them for their advice and support in school and life. I would like to thank Robert Boutelle, Abbas Mulla, Jonathan Shaw, Dr. Anthony Shoji Hall, Devin Brandt, Michael Tyrone Yeung, Jordan Aguirre, Eric Farr, Abraham Buditama, and Johnny Dadras.

Finally, I would like to thank my parents, who raised me, and continuously supported me during graduate school. I want to mention one thing to you guys in Punjabi: Dhan Guru Nanak Tera Shukar Hai.

Life is very mysterious; you never know where it will end up taking you. I am grateful to have crossed paths with everyone here and hope to meet all of you again in the future.

CHAPTER 1

Nanoscale Studies of Cage Molecules Using Scanning Tunneling Microcopy

1.1 Introduction

Scientific research exists solely to investigate novel systems and to seek answers to fundamental problems in order to broaden our understanding of the physical world. Nanoscience allows us to study properties of materials and various molecules from the bottom up and to break new frontiers with more advanced capabilities. Using new techniques, we can analyze structural, electrical properties at the nanoscale, which gives us greater understanding at the molecular level. Being able to control molecular systems at the nanoscale will give precise control at the macroscale when creating new materials or devices. This ability to fine tune at such an intricate scale will allow new materials and devices to be created for various types of applications [1-4].

1.2 Self Assembled Monolayers

Molecular self-assembly occurs by means of spontaneous chemisorption at the adsorbate-substrate interface resulting in highly ordered, closed-packed monolayers [5]. Many different types of materials that are composed of organic/inorganic molecules, nanoparticles, and biological molecules exploit self-assembly in order to create designer specific nanomaterials that have distinguishing features at the nanoscale. Taking advantage of the various properties of molecules and surfaces allows one to create different types of SAMs by simply altering physical conditions. Many types of surfaces, typically coinage metals can be functionalized with different types of molecules with various types of head groups such as: (-OH, -NH2, -COOH, -SH) [6, 7]. Altering either head or tail groups can affect the interaction between other molecules and the surface [8]. Probing and understanding the adsorbate-surface interaction at the nanoscale, especially for single molecules still remains a difficult task. One of the most common SAMs that

has been widely studied and is relatively well understood are alkanethiols on Au{111} [9-11]. Alkanethiolate SAMs form by spontaneous chemisorption of the sulfur head group and the gold surface as seen in figure 1.1 and described by the following chemical equation[12-14]:

$$RS - H + Au(s) \rightarrow RS - Au(s) + 0.5\ H_2,$$

where R is the molecule backbone. Chemisorption of alkanethiols to gold is a two-step process: first, a kinetics-based step involves rapid adsorption to the surface occurs within seconds to minutes [15]; second, the alkyl chains align and crystallize which typically takes minutes to hours as governed by the transition from molecules in a lying down phase to an ordered standing up phase [12, 13, 15-17]. Three main forces behind alkanethiolate assembly are: the favorable sulfur gold bond (~45 kcal/mol), van der Waals interactions between methylene groups on the alkyl chains (~1 kcal/mol per methylene groups), and interactions between end groups [5, 12, 13, 15, 18].

Alkanethiol monlayers can be visualized at the molecular level using STM. Images acquired with an STM reveal characteristic features of alkanethiolate SAMs, such as domains, domain boundaries (tilt and phase boundaries), step edges, substrate adatoms, and substrate vacancy islands, as shown in figure 1.1. When *n*-alkanethiol molecules form a SAM, each individual molecule tilts at a 30° angle with respect to the gold surface normal in order to maximize van der Waals interactions. [10, 19-21]. Full monolayers of *n*-alkanethiolates form close-packed lattices $\left(3\ x\ \sqrt{3}\right)$R30° with respect to the underlying gold surface and c(4x2) superlattices. The $\left(3\ x\ \sqrt{3}\right)$R30° lattice is common for shorter alkanethiols (10 carbons or less) whereas longer chain alkanethiols (11 carbons or more) form c(4x2) superlattices that have domains of $\left(3\ x\ \sqrt{3}\right)$R30° [22-24]. Longer chains form these superlatticles due to the strong intermolecular interactions between alkyl chains more so than the sulfur-gold interaction [5, 10,

18, 25, 26]. Ordered regions where alkanethiolate molecules tilt in the same direction are called domains, which are on the order of several hundred Ångstroms and have a lattice spacing of 4.99 Å [10, 13, 27]. Tilt domains result from molecules oriented in different azimuthal directions converging upon another whereas phase boundaries result from different crystallographic orientations in the substrate. Domain boundaries are defined as the region between two different domains with different tilt directions or binding sites [27-29]. The largest types of defects are caused by the underlying gold surface, step edges, which naturally exist on the gold surface and are caused by the roughness of the substrate [27]. Self-assembled monolayers can be made using various methods such as solution and vapor deposition. Alkanethiolate SAMs are made by adsorbing *n*-alkanethiolate molecules to the surface, either through solution or vapor deposition. Solution deposition involves submerging the sample into a molecular solution (diluted alkanethiols in ethanolic solution), as shown in figure 1.2. Vapor deposition involves sealing the sample with a small amount of the molecular solution. Self-assembled monolayers demonstrate more order when left in solution for longer periods of time at room temperature or at eleveated temperatures, often 78 °C. This is due to molecules becoming more mobile, which minimizes defects [27-32]. When molecules are deposited, alkanethiol molecules increase the surface energy of gold atoms, which allows these sulfur-gold complexes to be more mobile and migrate across the surface creating small areas one atom lower than a gold terrace known as a substrate vacancy island, or one atom above gold terraces known as a substrate adatom. [27-30, 32]. Controlling the amount and types of defects is critical in device fabrication and having even greater control at the adsorbate-surface interface as shown in Chapter 2.

1.3 Scanning Tunneling Microscopy

Scanning tunneling microscopy was first developed in 1981 by Binnig and Rohrer, which enabled imaging of coinage metals at the atomic level [33]. Since its development, STM has played a major role in probing electronic and topographic information of various systems at the nanoscale [33-38]. Further developments and modifications have been made to allow STM to give greater chemical information about molecular systems such as ultra high vacuum (UHV) systems with various spectroscopic techniques [39-42]. Scanning tunneling microscopy is similar to other probe techniques such as atomic force microscopy (AFM) in that an atomically sharp tip is rastered across the surface collecting information at every point, which is then converted to pixels that combine to make a image that allows one to visualize topographic and electronic information. The research that is discussed in this thesis uses ambient STM and UHV low-temperature STM, which provides a broader range of information about the chemical systems studied herein [43].

1.3.1 General Operation

Scanning tunneling microscopy takes advantage of a well understood quantum mechanics concept called quantum tunneling. An atomically sharp conducting tip is brought close to a conducting surface (typically coinage metals) and a bias (positive or negative) is applied between the two, which results in net current due to quantum tunneling to occur. Switching the bias polarity allows electrons to tunnel from the tip to the sample or the sample to the tip. The tip and surface each have electronic wavefunctions that overlap with each other when brought close together and electrons can tunnel through this vacuum resulting in a tunneling current. The tunneling current is extremely sensitive to the position of the tip and the height and electronic properties of the features on the surface.

Quantum tunneling primarily deals with electrons of non-zero probability that are able to tunnel through a potential barrier when they have less energy than the potential barrier, as shown in figure 1.3. The wave function of an electron can be modeled by the following function in a one-dimensional system:

$$\Psi(z) = \Psi(0)e^{-kz}, \qquad \text{(Equation 1.1)}$$

where *k* is the decay constant as the electrons tunnel through the potential barrier, and *z* is the tip-sample distance.

$$k = \sqrt{\frac{2m(V-E)}{\hbar}}, \qquad \text{(Equation 1.2)}$$

The overall wavefuntion of an electron includes various parameters when tunneling, where *m* is the mass of an electron, *V* is the potential energy of the barrier, and *E* is the energy of the electron. We can obtain the probability density of electrons that are able to tunnel through the potential barrier from the tunneling current I_T:

$$I_T(z) = |\Psi(z)|^2 \sim e^{-2kz}, \qquad \text{(Equation 1.3)}$$

As shown in Equation 1.3, the tip-sample separation (z) and tunneling current (I_T) are exponentially related. This allows for extremely precise imaging of the surface at the atomic level due to miniscule changes that can be detected in the current or tip-sample distance [37, 38, 44, 45]. The tip-surface distance can be set to two distinct modes of measurement: either constant-current mode or constant-height mode as shown in figure 1.4. In constant-current mode, it is possible to acquire precise (atomic-scale) topographic information where the tip rasters across the surface while the feedback loop maintains a constant current by adjusting the tip-sample distance. Constant-height mode keeps the tip at a constant distance from the surface allowing accurate analysis of surface atoms. Constant-current mode gives high precision but slower scans while constant-height mode gives faster scans but relatively low precision [38].

1.3.2 Local Barrier Height and Scanning Tunneling Spectroscopy

In addition to ambient STM, which allows topographic information to be obtained, UHV STM has some specific techniques that provide additional information of chemical systems such as scanning tunneling spectroscopy (STS) and local barrier-height (LBH) imaging. In addition to ambient STM, which measures a convolution of topographic and electronic information of the surface, STS allows additional electronic information to be acquired including conductance spectroscopy (*I*/*V*), differential conductance spectroscopy (d*I*/d*V*), and inelastic tunneling spectroscopy (IETS). In d*I*/d*V* spectroscopy, a sinusoidal modulation is applied to the bias voltage by the lock-in amplifier. The first and second harmonic frequencies can be extracted by the lock-in amplifier from the modulated current signal and then compared to a reference signal. The first harmonic of the current signal corresponds to dI/dV, which provides local density of states (LDOS) of the sample. The second harmonic of the current signal corresponds to d^2I/dV^2, which can provide vibrational information of molecules on the surface.

Local barrier-height imaging measures the local work function of the surface. The LBH(Φ) is proportional to the square of the derivative of the current signal with respect to the tip-sample distance as shown below:

$$\Phi \propto \frac{1}{8}\left(\frac{d\ln I}{dz}\right)^2, \qquad \text{(Equation 1.4)}$$

It can be seen that LBH affects the decay constant (k) and the tunneling current (I_t). The magnitude of the LBH is measured by modulating the tip-sample distance. In order to record LBH, the tip-sample distance is modulated sinusoidally using an AC voltage applied to the z direction piezo elastic translator allowing the imaging of buried interfaces [45, 46]. Apparent barrier height is usually compared with the average work function(Φ_{av}), which consists of the sample work function (Φ_S) and the tip work function (Φ_T)[37, 47]:

$$\Phi_{av} = \frac{(\Phi_S + \Phi_T)}{2}, \qquad \text{(Equation 1.5)}$$

In this thesis, we use LBH imaging to probe the interfaces of carboranethiolate SAMs in order to show a new method of molecular control at the nanoscale.

1.4 Thesis Overview

This thesis will describe new ways of phase control and systems involving novel cage molecules, such as carboranedithiols and adsorbate-surface interactions in exchange reactions between molecules with sulfur and selenol head groups. Chapter 2 focuses on phase control of carboraneditiols involving different binding modalities. Chapter 3 will explore how *p*-carborane and its functionalized derivative, known as *p*-mercaptobenzoic acid assemble and interact in a monolayer. Chapter 3 has been adapted and reprinted with permission from (Thomas, J. C.; Boldog, I.; Auluck, H. S.; Bereciartua, P.; Dušek, M.; Macháček, J.; Bastl, Z.; Weiss, P. S.; Baše, T. Self-Assembled *p*-Carborane Analog of *p*-Mercaptobenzoic Acid on Au{111}. *Chem. Mater.* **2015**, *27*, 5425–5435.). Copyright (2015) American Chemical Society. Chapter 4 describes a new way of controlling molecules at the nanoscale using temperature. Chapter 4 has been adapted and reprinted with permission from (Thomas, J. C.; Schwartz, J. J.; Hohman, J. N.; Claridge, S. A.; Auluck, H. S.; Serino, A. C.; Spokoyny, A. M.; Tran, G.; Kelly, K. F.; Mirkin, C. A.; Gilles, J.; Osher, S. J.; Weiss, P. S. Defect-Tolerant Aligned Dipoles within Two-Dimensional Plastic Lattices. *ACS Nano*. **2015**, *9*, 4734–4742.). Copyright (2015) American Chemical Society. Chapter 5 focuses on how alkanethiols and alkaneselenols exchange with each other on Au{111}. Chapter 5 has been adapted and reprinted with permission from (Hohman, J. N.; Thomas, J. C.; Zhao, Y. X.; Auluck, H.; Kim, M.; Vijselaar, W.; Kommeren, S.; Terfort, A.; Weiss, P. S. Exchange Reactions between Alkanethiolates and Alkaneselenols on Au{111}. *J. Am. Chem. Soc*. **2014**, *136*, 8110-8121.). Copyright (2015) American Chemical Society.

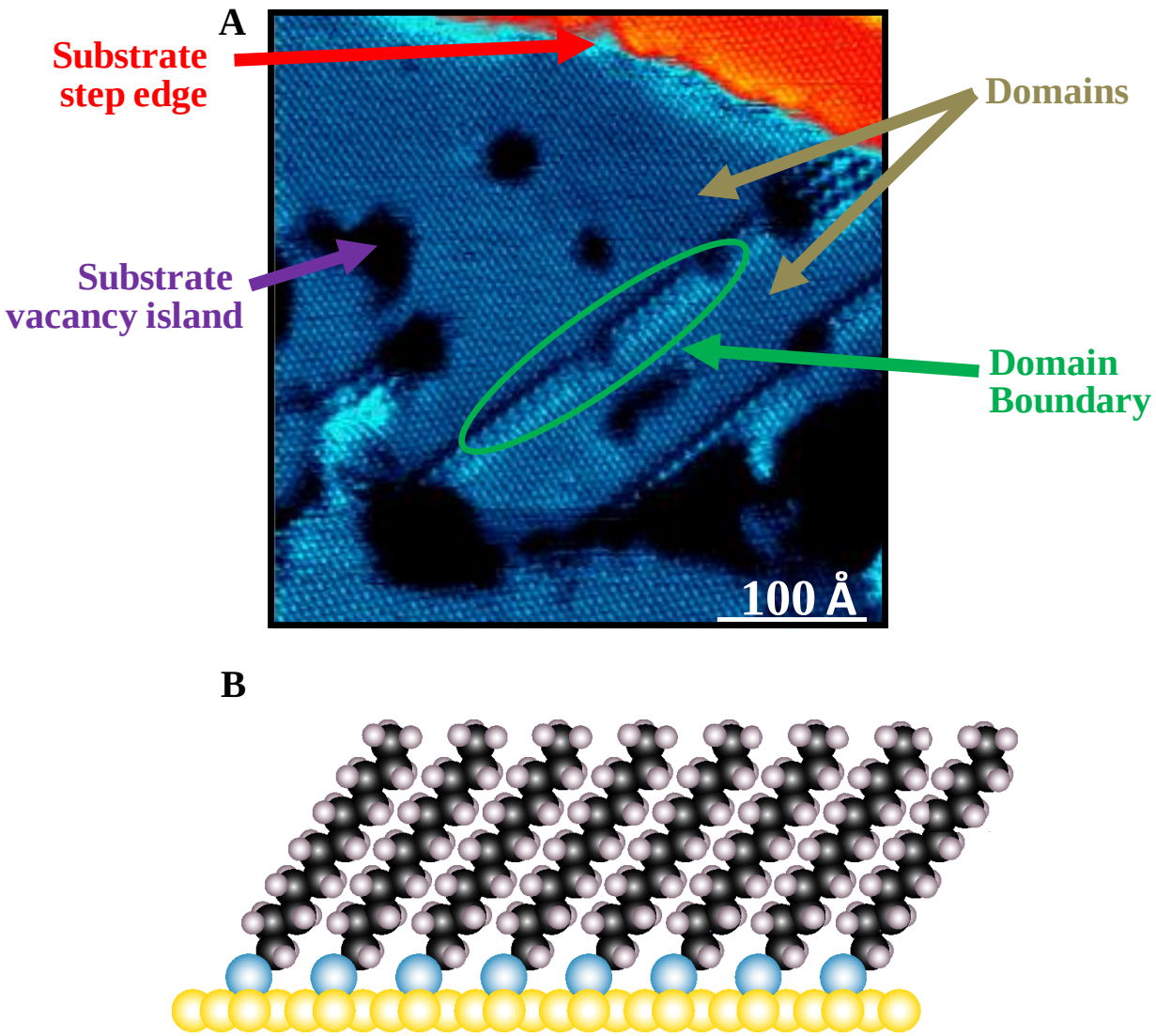

Figure 1.1: (A) Scanning tunneling microscopy image of 1-dodecanethiolate (C12) SAM assembled on a Au{111}/mica substrate. Characteristic defects within the monolayer are intrinsic to ordered SAMs and the underlying substrate. Defects include vacancy islands (red arrow), step edges (purple arrow), domain boundary (green arrow), and 1-dodecanethiolate domains (brown arrow). Image is recorded with a sample bias, V_S = -1 V and tunneling current, I_T = 1 pA [48]. **(B)** Schematic of a C12 monolayer, illustrating the packing and tilt of the molecules. Gold is depicted by the gold circles, sulfur by the blue circles, carbon by the black circles, and hydrogen by the white circles.

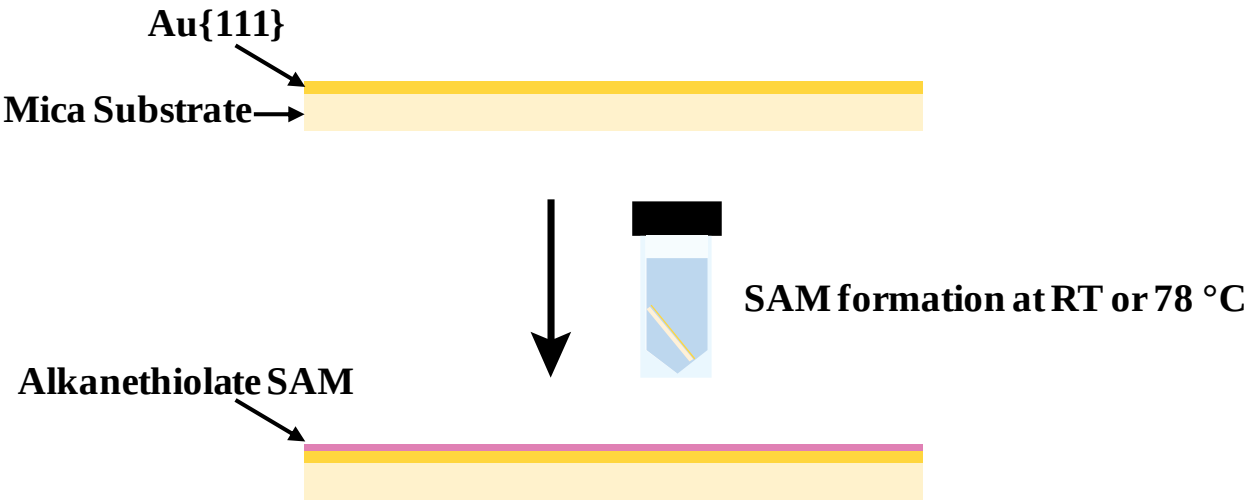

Figure 1.2: Schematic of alkanethiol SAM formation on Au{111}/mica via solution deposition. Au{111}/mica is placed in a molecular solution (diluted alkanethiols in a ethanolic solution) after flame-annealing which results in SAM formation.

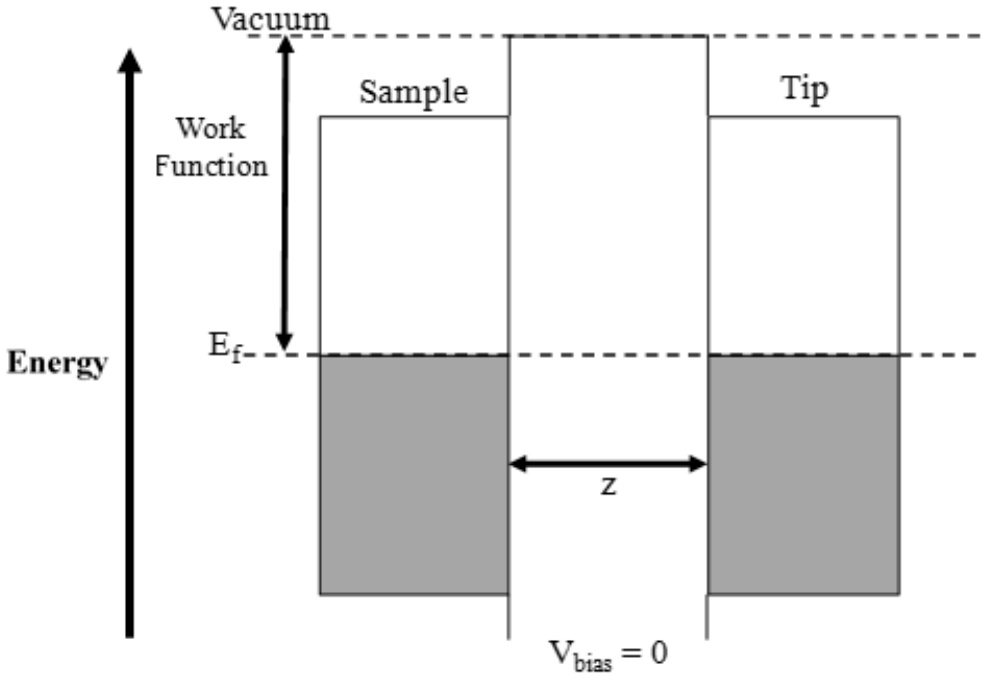
Vacuum
Sample
Tip
Work
Function
Energy
E_f
z
$V_{bias} = 0$

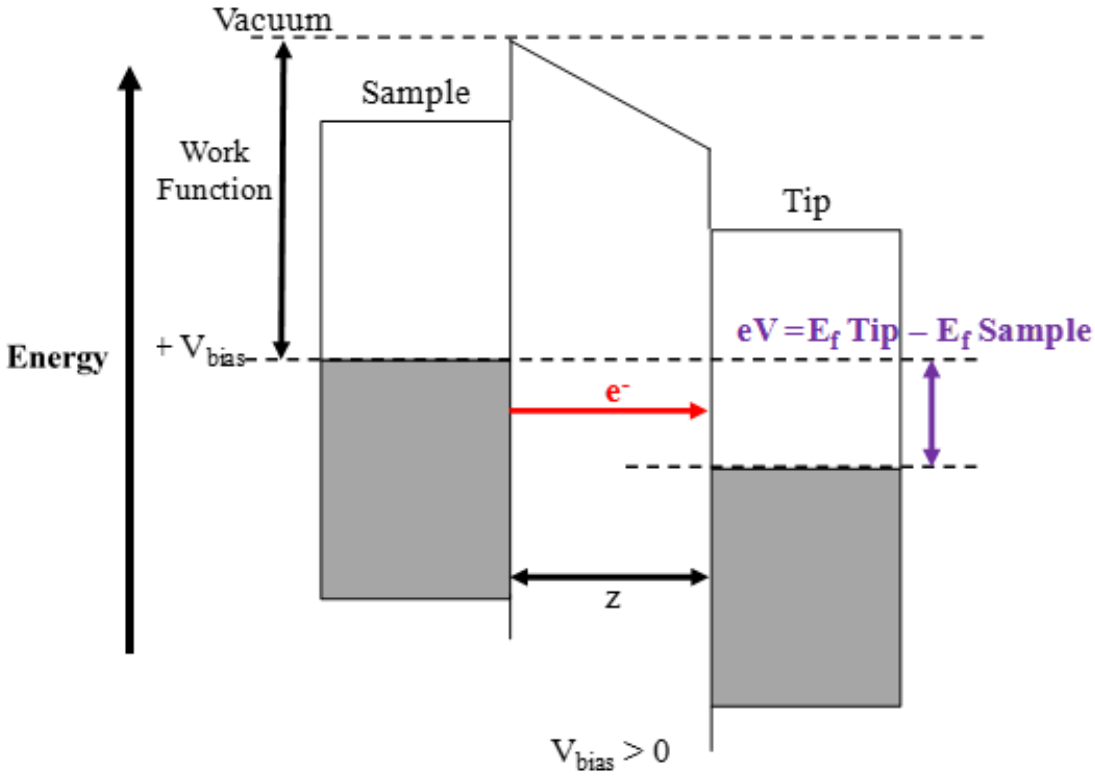
Vacuum
Sample
Work
Function
Tip
Energy
$+ V_{bias}$
$eV = E_f$ Tip $- E_f$ Sample
e^-
z
$V_{bias} > 0$

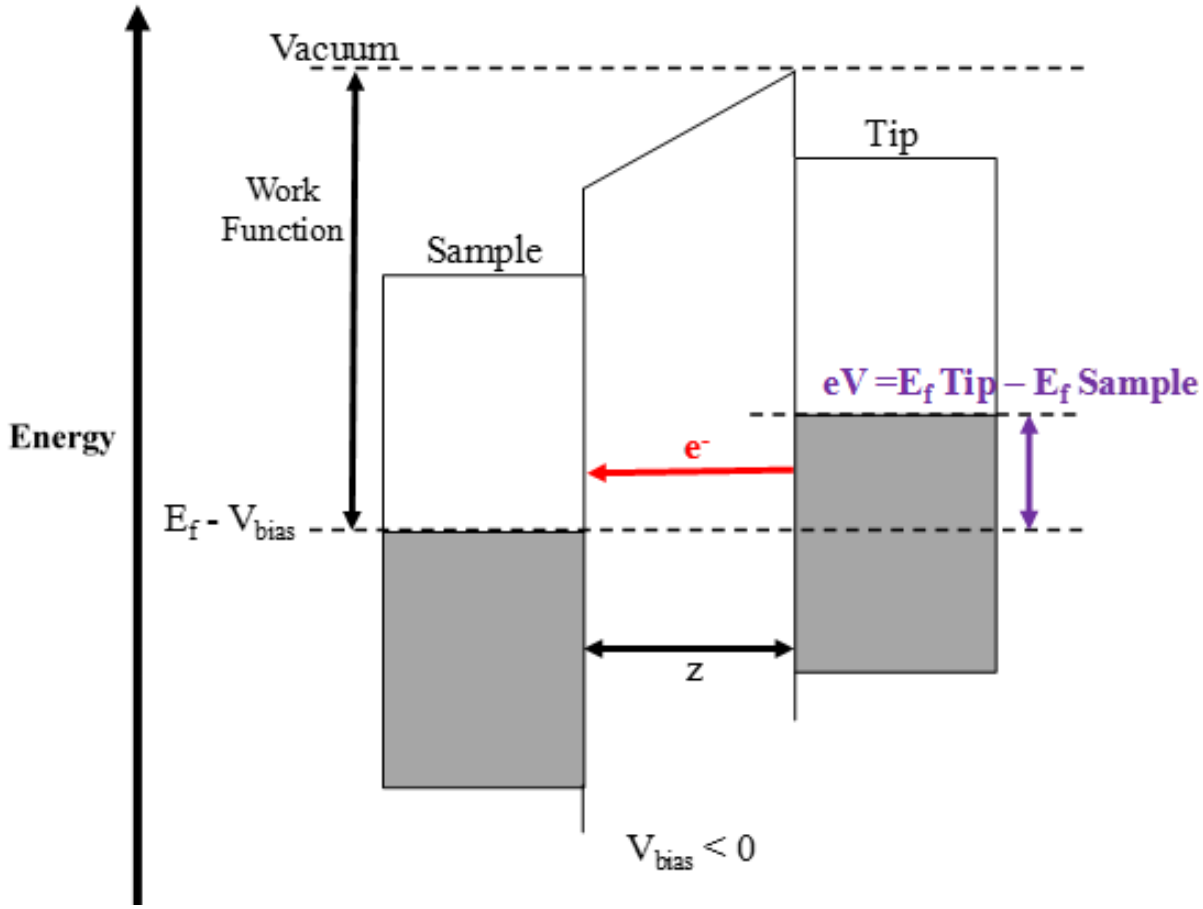

Figure 1.3: Schematic of a tunneling junction between the STM sample and tip. The grey area represents electron filled states and the white area represents empty states. Electrons can generate a tunneling current if the tip-sample distance (z) is relatively small. **(A)** There is no net current since the Fermi level, E_f, of the sample and tip are equal. **(B)** When applying a positive bias ($V_{bias} > 0$) the Fermi level of the sample increases by eV_{bias} and electrons tunnel from the sample to the tip. **(C)** When applying a negative bias ($V_{bias} < 0$) the Fermi level of the sample decreases by eV_{bias} and electrons will tunnel from the tip to the sample.

A – Constant-Current Mode

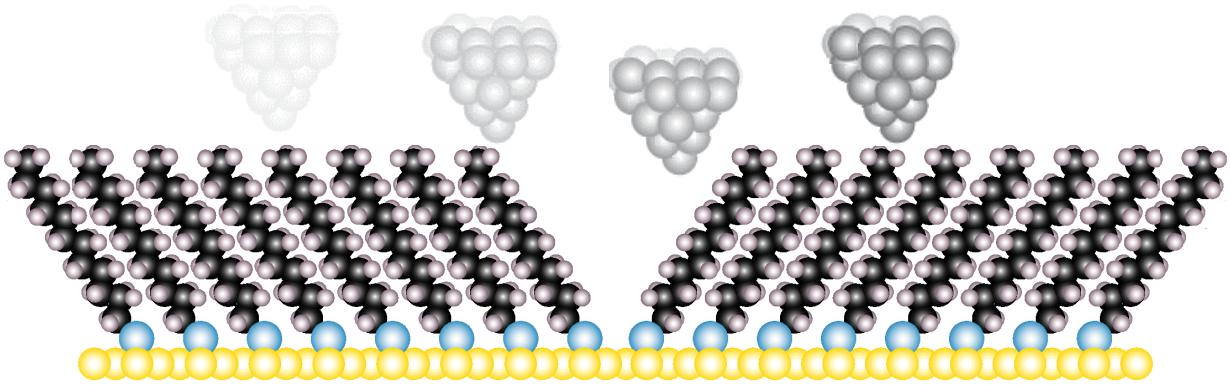

B – Constant-Height Mode

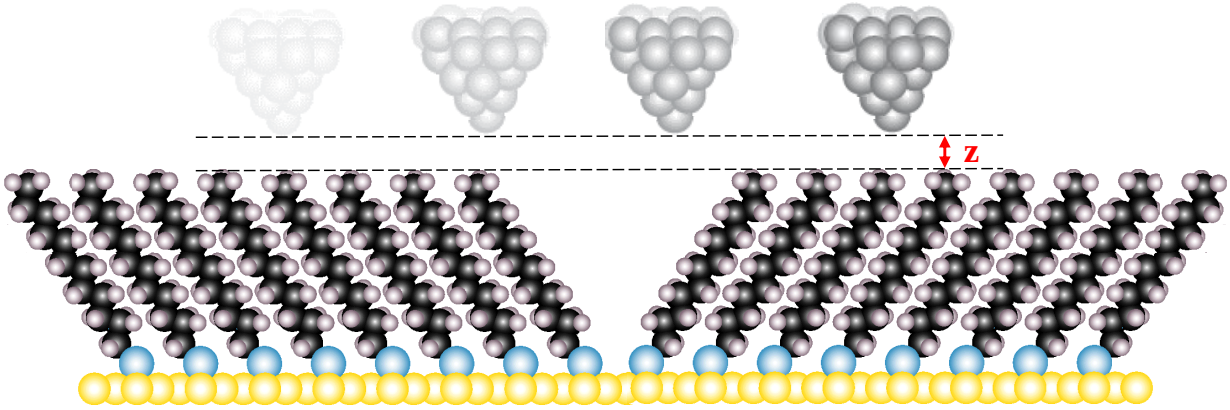

Figure 1.4: Schematic of a STM tip rastering across a 1-dodecantiolate SAM in two different acquisition modes **(A)** Constant-current mode where the tip-sample distance (z) changes due to surface features are collected while tunneling current stays constant. **(B)** Constant-height mode where the current changes are recorded while the average tip-sample distance (z) stays constant.

1.5 References

1. Saini, R.; Saini, S.; Sharma, S. Nanotechnology: the future medicine. *J. Cutan. Aesthet. Surg.* **2010**, *3*, 32-33.

2. Balzani, V. Nanoscience and nanotechnology: the bottom-up construction of molecular devices and machines. *Pure Appl. Chem.* 2008, *80*, 1631-1650.

3. Whitesides, G. M. Nanoscience, nanotechnology, and chemistry. *Small* **2005**, *1*, 172-179.

4. Heath, J. R. Nanoscale materials. Accounts of chemical research. **1999.** *32*, 388-388.

5. Love, J. C.; Estroff, L. A.; Kriebel, J. K.; Nuzzo, R. G.; Whitesides, G. M. Self-assembled monolayers of thiolates on metals as a form of nanotechnology. *Chem. Rev.* **2005**, *105*, 1103-1169.

6. Madou, M. Fundamentals of microfabrication: the science of miniaturization. *CRC* **2002**, 62-63.

7. Saliterman, S. Self-assembled monolayers (sams). Fundamentals of biomems and medical microdevices. *SPIE Press*. **2006,** 94–96.

8. Hohman, J. N.; Kim, M.; Shüpback, B.; Kind, M.; Thomas, J. C.; Terfort, A.; Weiss, P. S. Dynamic double lattice of 1-adamantaneselenolate self-assembled monolayers on au{111}. *J. Am. Chem. Soc.* **2011**, *133*, 19422-19431.

9. Nuzzo, R. G.; Allara, D. L. Adsorption of bifunctional organic disulfides on gold surfaces. *J. Am. Chem. Soc.* **1983**, *105*, 4481-3.

10. Nuzzo, R. G.; Dubois, L. H.; Allara, D. L. Fundamental-studies of microscopic wetting on organic-surfaces. 1. Formation and structural characterization of a self-consistent series of polyfunctional organic monolayers. *J. Am. Chem. Soc.* **1990**, *112*, 558-569.

11. Nuzzo, R. G.; Zegarski, B. R.; Dubois, L. H. Fundamental studies of the chemisorption of organosulfur compounds on gold(111). Implications for molecular self-assembly on gold surfaces. *J. Am. Chem. Soc.* **1987**, *109*, 733-40.

12. Ulman, A. Formation and structure of self-assembled monolayers. *Chem. Rev.* **1996,** *96*, 1533-1554.

13. Ulman A. An introduction to ultrathin organic films from langmuir–blodgett to self-assembly. *Academic Press*, **1991,** Boston.

14. Reed M. A.; Tour, J. M. Computing with molecules. *Sci. Am.* **2000.** 86-93.

15. Bain, C. D.; Troughton, E. B.; Tao, Y-T.; Evall, J.; Whitesides, G. M.; Nuzzo, R. G. Formation of monolayer films by the spontaneous assembly of organic thiols from solution onto gold. *J. Am. Chem. Soc.* **1989**, *111*, 321–335.

16. Grunze M. Preparation and characterization of self-assembled organic films on solid substrates. *Phys. Scr.* **1993.** *T49B*, 711-717.

17. Noh, J.; Hara, M. Final phase of alkanethiol self-assembled monolayers on Au(111). *Langmuir* **2002,** *18*, 1953-1956.

18. Dubois, L. H.; Nuzzo, R. G. Synthesis, structure, and properties of model organic surfaces. *Annu. Rev. Phys. Chem.* **1992**, *43*, 437-63.

19. Han, P.; Kurland, A. R.; Giordano, A. N.; Nanayakkara, S. U.; Blake, M. M.; Pochas, C. M.; Weiss, P. S. Heads and tails: simultaneous exposed and buried interface imaging of monolayers. *ACS Nano* **2009**, *3*, 3115-3121.

20. Porter, M. D.; Bright, T. B.; Allara, D. L.; Chidsey, C. E. D. Spontaneously organized molecular assemblies. 4. Structural characterization of n-alkyl thiol monolayers on gold by optical ellipsometry, infrared spectroscopy, and electrochemistry. *J. Am. Chem. Soc.* **1987**, *109*, 3559-3568.

21. Atre, S.V.; Liedberg. B.; Allara, D. L. Chain-length dependence of the structure and wetting properties in binary composition monolayers of oh-terminated and ch_3-terminated alkanethiolates on gold. *Langmuir* **1995**, *11*, 3882-3893.

22. Camollone III, N.; Chidsey C. E. D.; Liu, G.-y.; Scoles, G. Superlattice structure at the surface of a monolayer of octadecanethiol self-assembled on au(111). *J. Chem. Phys*. **1993,** *98*, 3503-3511.

23. Fenter, P.; Eisenberger, P.; Liang, K. S. Chain-length dependence of the structures and phases of $CH_3(CH_2)$ *n*-1-SH self-assembled on Au(111). *Phys. Rev. Lett*. **1993**, *70*, 2447-2450.

24. Poirier, G. E.; Tarlov, M. J. The *c*(4 × 2) superlattice of *n*-alkanethiol monolayers self-assembled on Au(111). *Langmuir* **1994**, *10*, 2853-2856.

25. Allara, D. L.; Nuzzo, R. G. Spontaneously organized molecular assemblies. 1. Formation, dynamics, and physical-properties of normal-alkanoic acids adsorbed from solution on an oxidized aluminum surface. *Langmuir* **1985.** *1*, 45-52.

26. Allara, D. L.; Nuzzo, R. G. Spontaneously organized molecular assemblies. 2. Quantitative infrared spectroscopic determination of equilibrium structures of solution-adsorbed normal-alkanoic acids on an oxidized aluminum surface. *Langmuir* **1985.** *1*, 52-66.

27. Poirier, G. E. Characterization of organosulfur molecular monolayers on Au(111) using scanning tunneling microscopy. *Chem. Rev.* **1997**, *97*, 1117-1127.

28. Poirier, G. E. Butanethiol self-assembly on Au(001): the 1×4 au missing row, c(2×8) molecular lattice. *J. Vac. Sci. Technol., B* **1996**, *14*, 1453-1460.

29. Poirier, G. E.; Pylant, E. D. The self-assembly mechanism of alkanethiols on Au(111). *Science* **1994**, *272*, 1145-1148.

30. Poirier, G. E. Mechanism of formation of au vacancy islands in alkanethiol monolayers on Au(111). *Langmuir* **1997,** *13*, 2019-2026.

31. Bumm, L. A.; Arnold, J. J.; Cygan, M. T.; Dunbar, T. D.; Burgin, T. P.; Jones, L.; Allara, D. L.; Tour, J. M.; Weiss, P. S. Are single molecular wires conducting? *Science* **1996**, *271*, 1705-1707.

32. Vericat, C.; Vela, M. E.; Salvarezza, R. C. Self-assembled monolayers of alkanethiols on Au(111): surface structures, defects and dynamics. *Phys. Chem. Chem. Phys.* **2005**, *7*, 3258-3268.

33. Bining, G.; Rohrer, H. Scanning tunneling microscopy. *IBM J. Res. Dev.* **1986,** *30*, 355-369.

34. Bining, G.; Rohrer, H. Scanning tunneling microscopy. *Helv. Phys. Acta* **.1982**, *55*, 726-735.

35. Binning, G.; Rohrer, H. Scanning tunneling microscopy: from birth to adolescence. *Rev. Mod. Phys.* **1987,** *59*, 615-625.

36. Griffith, J. E.; Kochanski, G. P. Scanning tunneling microscopy. *Annu. Rev. Mater. Sci.* **1990**, *20*, 219-244.

37. Binning, G.; Rohrer, H. Scanning tunneling microscopy. *Surf. Sci.* **1983**, *126*, 236-244.

38. Chen C. J. Introduction to scanning tunneling microscopy. *Oxford University Press: New York*, **1993**.

39. Eigler, D. M.; Weiss, P. S.; Schweizer, E. K..; Lang, N. D. Imaging Xe with a low-temperature scanning tunneling microscope. *Phys. Rev. Lett.* **1991,** *66*, 1189-1192.

40. Golubok, A. O.; Tiofeey, V. A. STM combined with SEM without SEM capability limitations. *Ultramicroscopy* **1992,** *42*, 1558-1563.

41. Sawada, D.; Hirai, A.; Sugimoto,Y.; Abe, M.; Morita, S. Simultaneous atomic imaging of atomic force microscopy and scanning tunneling microscopy using metal coated cantilevers. *Mat. Trans*. **2009,** *50*, 940-942.

42. Moore, A. M.; Yeganeh, S.; Yao, Y.; Claridge, S. A.; Tour, J. M.; Ratner, M. A.; Weiss, P. S. Polarizabilities of adsorbed and assembled molecules: measuring the conductance through buried contacts. *ACS Nano* **2010**, *4*, 7630-7636.

43. Ferris, J. H.; Kushmerick, J. G.; Johnson, J. A.; Yoshikawa Youngquist, M. G.; Kessinger, R. B.; Kingsbury, H. F.; Weiss, P. S. Design, operation, and housing of an ultrastable, low temperature, ultrahigh vacuum scanning tunneling microscope. *Rev. Sci. Instrum.* **1998,** *69*, 2691-2695.

44. Tersoff, J.; Hamann, D. R. Theory and application for the scanning tunneling microscope. *Phys. Rev. Lett.* **1983,** *50*, 1998-2001.

45. Garcia, N. Theory of scanning tunneling microscopy and spectroscopy – resolution, image and field states, and thin oxide layers. *IBM J. Res. Dev.* **1986,** *30*, 533-542.

46. Pitarke, J. M.; Echenique, P. M.; Flores, F. Apparent barrier height for tunneling electrons in STM. *Surf. Sci.* **1987**, *217*, 267-275.

47. van de Leemput, L. E. C.; van Kempen, H. Scanning tunneling microscopy. *Rep. Prog. Phys.* **1992**, *55*, 1165-1240.

48. Weiss, P. S. Functional molecule and assemblies in controlled environments: formation and measurements. *Acc. Chem. Res.* **2008**, *41*, 1772-1781.

CHAPTER 2

Phase Control of Carboranedithiols

2.1 Introduction

Creating nanoscale devices and materials that push current technological limits requires precision at the nanoscale. Controlling the tunable properties of nanoscale devices can be achieved through self-assembly. *n*-Alkanethiolates are prototypical SAMs that have various types of domains and defects due to the conformational flexibility of the alkyl chains. Minimizing and controlling these defects at the nanoscale allows for optimal device fabrication. This can be achieved through precise control of molecular building blocks and their placement at the nanoscale using bottom-up assembly. Domains and defects form due to the specific chemical properties between molecules and the molecule-substrate interface. These defects hinder the arrangement of molecules and surface atoms within monolayers, hindering device efficiency. We can minimize defects and take advantage of them by using upright, symmetric cage molecules, such as carboranes. Cage molecules allow for more directed assembly due to their rigid three-dimensional structures, high stability to chemical and heat degradation, symmetry, rigidity, controllable intermolecular interactions, and straightforward functionalization [1]. These cage molecules do not contain tilt domain defects as seen in *n*-alkanethiol monolayers, thus minimizing the types of defects in these two-dimensional plastic lattices. We can exploit the symmetry of cage molecules, specifically carboranes in order to reduce the types of defects and create more efficient materials and devices.

Carboranethiols are derived from cage molecules, known as icosahedral dicarba-closo-dodecaboranes, with the molecular formula $C_2B_{10}H_{12}$ and have been used in boron chemistry since the 1960's [2-5]. The unique characteristic of the icosahedral carborane structure is that the

boron and carbon atoms are hexacoordinated, which gives them unique chemical properties. This expanded valence of boron causes them to be electron deficient. The carbon atoms in the icosahedral carborane structure can be positioned adjacent to each other (ortho), at opposite ends of the icosahedrons (para), or separated by a boron atom (meta); this flexibility in positioning the carbon atoms and electronegativity difference with boron causes the dipole moment to change drastically without changing the molecular geometry. Carboranethiols have been designed with molecular dipoles in mind; the dipoles are the result of charge separation in the molecule and can contribute favorably or unfavorably to intermolecular interactions. Carboranethiols can be functionalized in many ways, especially with thiol or selenol groups, enabling them to be used in SAMs and forming two-dimensional plastic lattices. These molecules form monolayers with tunable properties while maintaining rigid and well-defined morphologies [6, 7-10].

It has previously been shown by Hohman et al. that monothiolated carboranes create rigid two-dimensional plastic lattices, where the tunable the properties of these carboranes play a significant role. The dipole moment can be tuned in such a way that allows for greater intermolecular dipole-dipole interactions resulting SAMs, which are resistant to exchange with *n*-alkanethiols or SAMs that have minimal intermolecualar interactions and are easily displaced with *n*-alkanethiols. Molecular interactions in monothiolated carborane SAMs are significant due to carboranethiols with laterally interacting dipole moments dictating surface coverage when codeposited along with carboranethiols with weaker intermolecular interactions [6]. While monothiolated carboranes have been studied and characterized, carboranedithiols have yet to be fully characterized and understood in terms of their adsorbate-surface interface. Carboranedithiols have two thiol groups in comparison to monothiolated carboranes resulting in SAMs which are possibly more resistant to exchange by *n*-alkanethiols due the second S-Au

bond. In this chapter, we are going to explore 1,2-dicarba-*closo*-dodecaboranedithiol and 1,2-dicarba-*closo*-dodecaboranediselenol; henceforth 1,2-carboranedithiol (**12CDT**) and 1,2-carboranediselenol (**12CDS**), respectively; both molecules are shown in figure 2.1.

2.2 Methods and Materials

2.2.1 Materials

The chemicals *n*-dodecanethiol, benzene, nitric acid, hydrochloric acid (Sigma-Aldrich, St. Louis, MO), sodium hydroxide (UCLA Chemistry), 1,2-dicarba-*closo*-dodecaboranedithiol, 1,2-dicarba-*closo*-dodecaboraneditselenol (Tomas Base, IICA Czech Republic) were used as received. All carboranedithiol monolayers were fabricated by immersing flame-annealed Au{111}/mica substrates (Agilent Technology, Tempe, AZ) into 1mM benzoic solutions. Acidic and basic carboranedithiol monolayers were immersed in 1:1 **12CDT**:HCl, 1:1 **12CDT**:HNO_3 and 1:2 **12CDT**:NaOH ethanolic solutions respectively. The *n*-dodecathiolate SAMs were prepared from 1mM ehtanolic solution. The Au/mica substrates were flame-annealed with 10 passes of a hydrogen flame (rate: 1 Hz). Samples were deposited in solution for 24 h, rinsed thoroughly with benzene three times and blown dry with high purity gaseous nitrogen. Perdeuterated n-dodecanethiolate SAMs were used as background references for normalization of FTIR spectra.

2.2.2 Scanning Tunneling Microscopy Measurements

All STM measurements were conducted using a custom beetle-style STM and a platinum/iridium tip (80:20) at ambient conditions [11]. Piezoelectric scanners were calibrated using the known lattice of 1-dodecanethilate on Au{111}. Carboranedithiolate and carboranediselnoate lattice spacing's were measured from the Fourier transforms of single-domain images. The sample was held between -1 V to -0.1 V sample bias range, and 256 x 256

pixel images were collected in constant-current mode with a tunneling current ranging from 1 to 200 pA. There is a strong tip dependence for imaging cage molecules [6].

2.2.3 Grazing Incidence Fourier Transform Infrared Spectroscopy

Vibrational spectra were collected using a Nicolet 8700 FTIR spectrometer (Thermo Electron Corp., Waltham, MA) which is equipped with a liquid-nitrogen cooled mercury-cadmium-telluride detector and a Seagull variable-angle reflection module (Harrick Scientific, Inc., Ossining, NY). Nitrogen gas was used to purge the system in order to remove water and carbon dioxide. Data were collected at a grazing incidence angle of 82° (normal to the surface) with *p*-polarized light and a mirror speed of 1.27 cm/s, with a resolution of 8 cm^{-1}. All spectra were averaged over 1024 scans and were normalized with a perdeuterated *n*-dodecanthiolate on Au{111} spectra.

2.3 Results and Discussion

2.3.1 Morphological Characterization of 1,2-dicarba-*closo*-dodecaboranethiol and Phase Control

The STM is capable of molecular- and atomic-scale resolution and provides chemical information regarding the relative size and conductance of molecules that are measured [12-14]. Here, we report the preparation of self-assembled monolayer's of **12CDT** and **12CDS**. The **12CDT** and **12CDS** molecules differ in their head groups which bind to the gold surface. Both of their dipole moments are normal to the surface with large dipole moments (~4 D), resulting in the modification of Au and Ag work functions [8, 15]. Herein we present our analysis of the lattice structures of **12CDT** and **12CDS** on Au{111} as determined by STM. Both SAMs appear structurally similar, but have significant differences in stability, which needs to be studied more closely. Previous studies have shown that some monofunctionalized carboranes are displaced by

1-dodecanethiolate (**C12**), but due to **12CDT** and **12CDS** being difunctionalized, the SAMs are more stable, as shown in the molecular exchange of these difunctionalzied SAMs with **C12** using FTIR.

Ambient STM images of molecular resolved **12CDT** and **12CDS** SAMs as shown in Figure 2.2 **12CDT** and **12CDS.** Both pack by a hexagonally close-packed lattice with a spacing of 7.2 Å, with minimal defects. Both SAMs are indistinguishable by STM and have round protrosions with similar apparent heights. As seen in figure 2.2A for the **12CDT** SAM, there are two different intensity protrusions with an apparent height difference of ~1 Å at these conditions; these differences in intensities correspond to two different binding sites [16]. We propose that the two different binding sites are as follows: more intense protrusions are one thiol and one thiolate bound to the surface versus the less intense protrusions having two thiolates bound to the surface. The 1 Å apparent height difference between the two different intensity protrusions can be attributed to the protonation state of the adsorbate causing the molecule to have different binding sites such as: two-fold bridge, three-fold hollow, and directly on top of the gold surface.

Taking a closer look, we propose that using either acid or base can change the protonation state of the adsorbate resulting in different binding sites. In order to control these binding modalities we used 2 equivalents of 1 mM NaOH in order to deprotonate the thiols. Imaging the **12CDT** sample again resulted in predominantly the lower intensity binding sites, as shown in figure 2.3. Similarly, in order to test for the higher intensity site, we exposed the surface to 1 equivalent of 1 mM of HCl in order to protonate one thiol, which resulted in the surface shown in figure 2.4. Using HCl to protonate the adsorbate was not successful in demonstrating phase control of binding modalities possibly due to unfavorable interactions of the Cl^- ions with the gold surface. Due to HCl yielding inconclusive results, another strong acid,

nitric acid (HNO_3) was used in order to protonate one thiol and avoid any possible side interactions with the gold substrate. Imaging the sample resulted in predominantly the higher intensity binding site, as seen in figure 2.5. Nitric acid did not interfere with the gold as chloride possibly did for HCl, successfully allowing phase control of both binding modalities independently.

2.3.2 Stability of Carboranedithiol Self Assembled Monolayers

Grazing incidence FTIR spectra of **12CDS** and **12CDT** SAMs were obtained from 800 to 4000 cm^{-1}, as shown in figure 2.6. Peaks in the region between 2500 to 2700 cm^{-1} are related to B-H stretches. Vibrational stretches in this region are characteristic of carboranes and are used as markers for these types of borane cluster cage molecules due to the intensity of the B-H stretch. This vibrational spectroscopy technique reveals the chemical fingerprint of the adsorbates on the surface and allows one to study the kinetics of displacement in order to understand the stability of **12CDT** and **12CDS** monolayers.

We monitor the exchange of **12CDT** and **12CDS** SAMs with **C12** by grazing incidence FTIR to determine the resistance to exchange and stability of the monolayers. As shown in figure 2.7, the FTIR spectra from 2500 to 3100 cm^{-1} are depicted. Single component **12CDT** and **12CDS** SAMs were immersed in 1 mM solutions of 1-dodecanethiol for 24 h intervals and 1 h intervals, respectively. At the end of each interval, spectra were collected and placed back into solution. Over the course of 120 h, the intensity of the B-H stretch near 2600 cm^{-1} had no substantial decrease in intensity for the **12CDT** SAM. For the **12CDS** SAM, the B-H stretch had no substantial decrease in intensity either. We do see a shift of about ~30 cm^{-1} in the B-H stretch indicating minimal insertion of **C12** into defects in the carborane lattice. This insertion of **C12** is seen by the increase in the symmetric and asymmetric CH_3 and CH_2 stretches in the spectral

data. Overall **12CDT** and **12CDS** SAMs are very stable and resistant to exchange due to the additional S/Se bond to Au and the low defect density of both **12CDT** and **12CDS** SAMs.

Additional FTIR studies were conducted in order to study the differences in how the carboranedithiols bind to the surface under neutral, acidic and basic conditions. As shown in figure 2.8, the carboranedithiolates under acidic and basic conditions show shifts in the B-H stretch relating to the change in binding modality whereas the neutral sample shows both vibrational shifts. Through STM and FTIR analysis it has been shown that phase control for carboranedithiolates is possible but further analyses need to be conducted to elucidate the binding modalities.

2.4 Conclusions and Future Prospects

In this work, carboranedithiols on gold film substrates have shown promising results in having control of molecules at the nanoscale. The molecule **12CDT** was characterized using STM and FTIR. When assembled on Au{111}, this molecule organizes itself into a hexagonal close-packed lattice with a spacing of 7.2 Å. The second thiol plays a key role in stabilizing the monolayer and allows precise control over different binding configurations. Studying the adsrobate-surface interface gives use more insight into how the adsorbates binding to the gold cause it to reconstruct due to the possible bonding arrangements such as two-fold bridge, three-fold hollow, adatom, and barbell configurations. With the ability to fine tune molecules and surfaces at such an intricate level, in this case through protonation states, more efficient molecular electronics and devices can be possible. We are able to gain more insight into the surface chemistry and physics at the nanoscale and this will enable the creation of cutting edge devices.

Future experiments will involve more in-depth computational studies in order to elucidate the proper binding modalities for **12CDT**. Two molecules of interest are **12CDS** and 9,12-dicarba-*closo*-dodecaboranedithiol (**912CDT)** due to their structural similarities to **12CDT**. Monolayers of **12CDS** have the same structures as **12CDT**, with selenium attachment instead of sulfur; this change enables comparisons of thiol versus selenol binding configurations. Once **12CDS** is fully resolved, we can test thiol/selenol exchange reactions with **12CDT** in order to see if Au-S or Au-Se is more favorable for these cage molecules. The **912CDT** molecule requires more attention due to its isomeric similarities to **12CDT** in that the thiols are now bound to boron atoms opposite carbon atoms [17]. The change in position of the thiol groups causes **912CDT** to have a dipole in the opposite direction when compared to **12CDT**. Codepositing this with **12CDT** will allow us to image how their dipoles interact on the surface. Additionally, probing the local barrier heights in these systems will result in better understanding of intermolecular interactions.

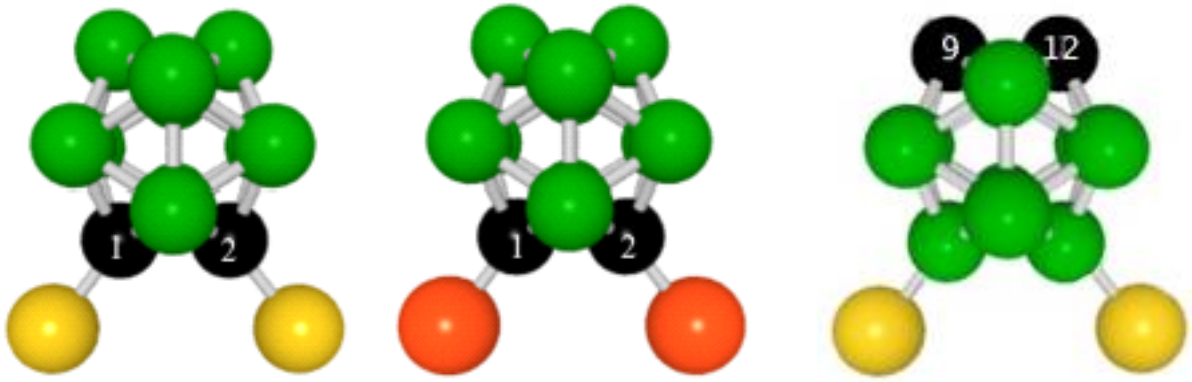

Figure 2.1: Three functionalized derivatives of 1,2-dicarba-*closo*-dodecaborane. Note that 1,2-caboranedithiol (**12CDT**) is on the left and 1,2-carboranediselenol (**12CDS**) is in the middle and 9,12-carboranedithiol (**912CDT**) is on the right.

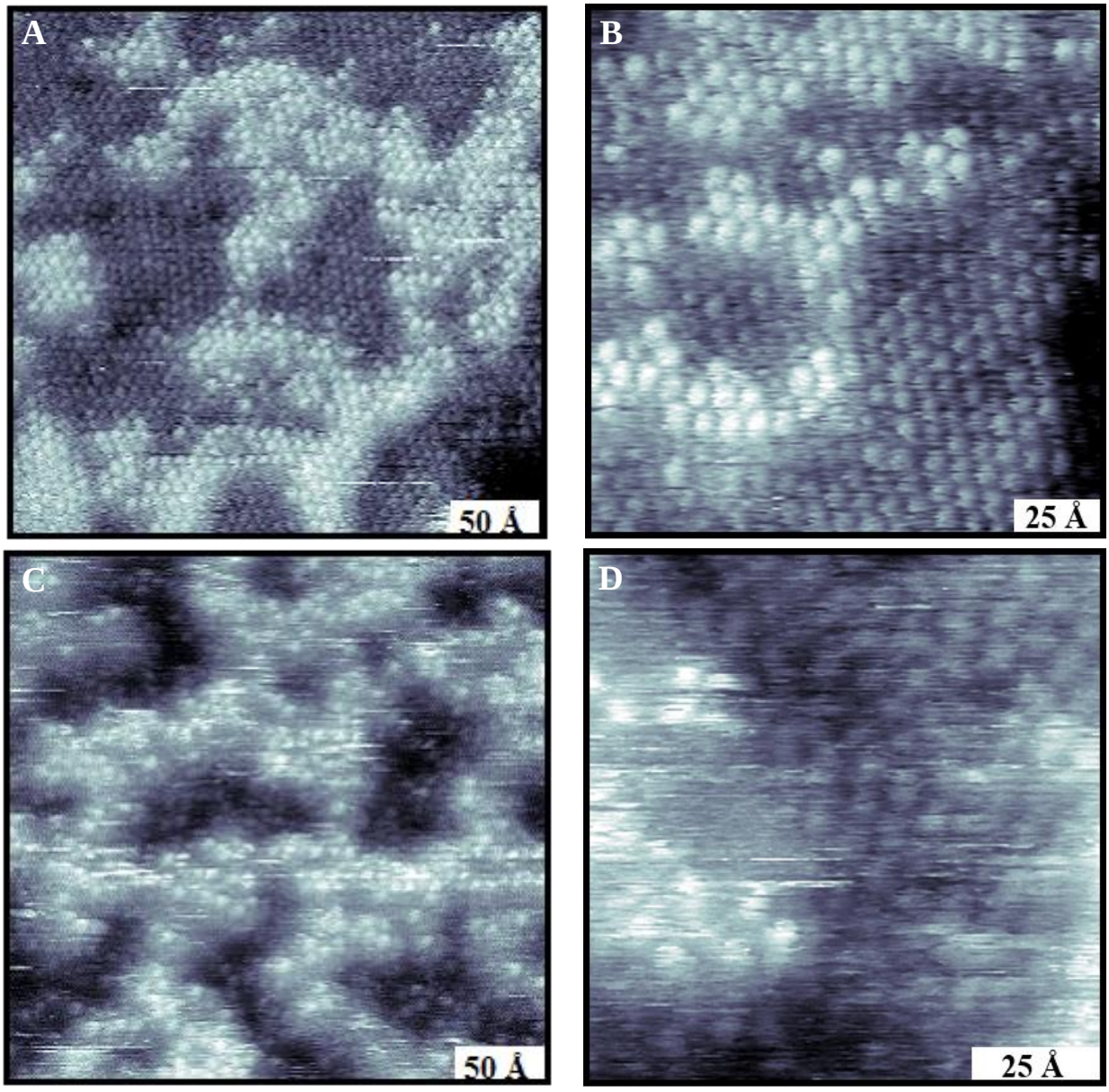

Figure 2.2: Scanning tunneling micrographs of **12CDT (A, B)** and **12CDS (C, D)** show two different intensities of protrusions. We attributed these more intense and less intense protrusions to two distinct binding modalities for each molecule. **(A)** Image is recorded with sample bias (V_S) = 0.1 V and tunneling current (I_T) = 120 pA. **(B)** Image is recorded with V_S = 0.1 V and I_T = 200 pA. **(C)** Image is recorded with V_S = 0.1 V and I_T = 100 pA. **(D)** Image is recorded with V_S = 0.1 V and I_T = 100 pA.

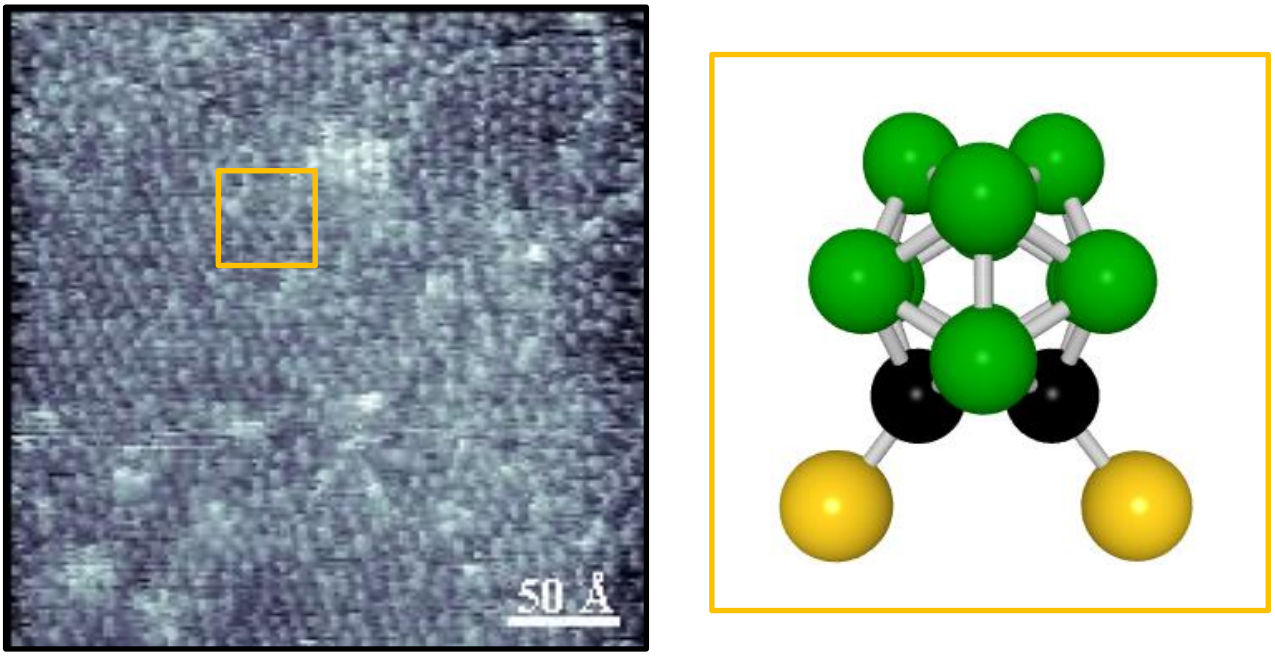

Figure 2.3: Scanning tunneling micrograph taken with an ambient STM of **12CDT** on Au{111}/mica after being exposed to 2 equivalences of 1 mM NaOH. We predominantly see one type of intensity, where both thiols are bound to the surface enclosed in the yellow box. Image is recorded with V_s = 1 V and I_T = 100 pA.

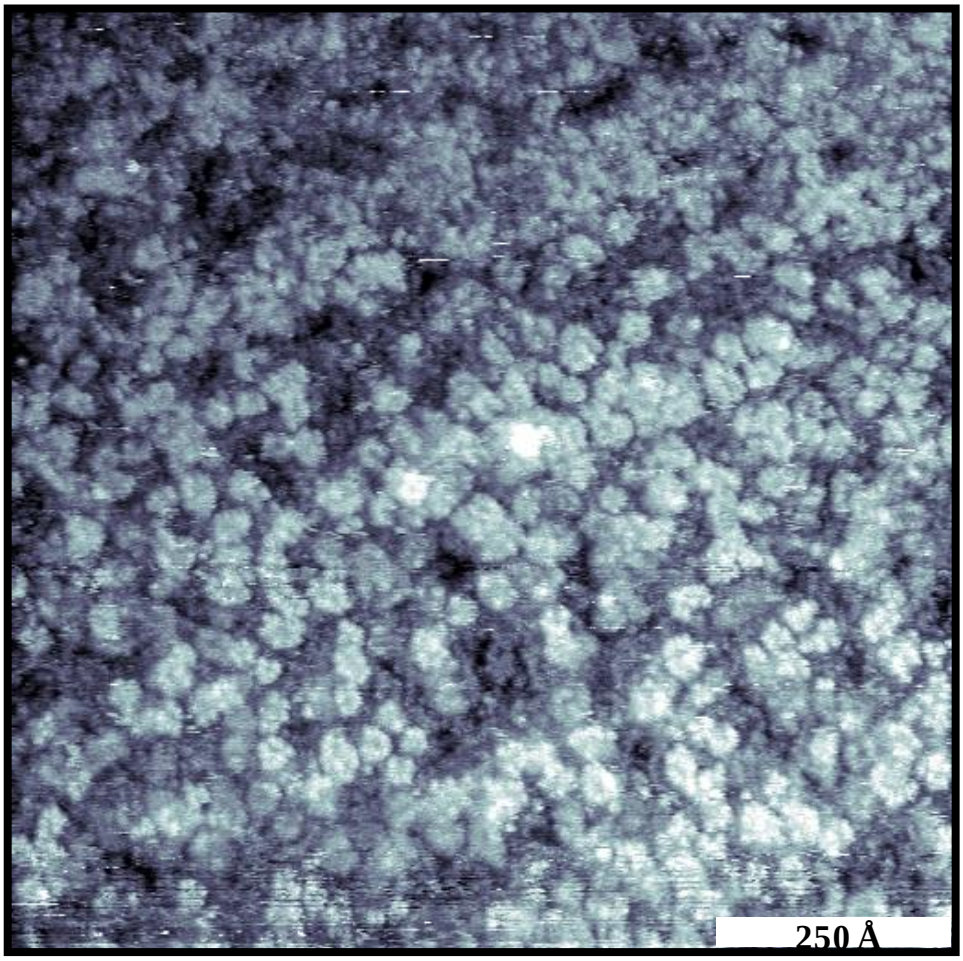

Figure 2.4: Scanning tunneling micrograph taken with an ambient STM of **12CDT** on Au{111}/mica after being exposed to 1 equivalence of 1 mM HCl. Image is recorded with $V_s = 1$ V and $I_T = 10$ pA.

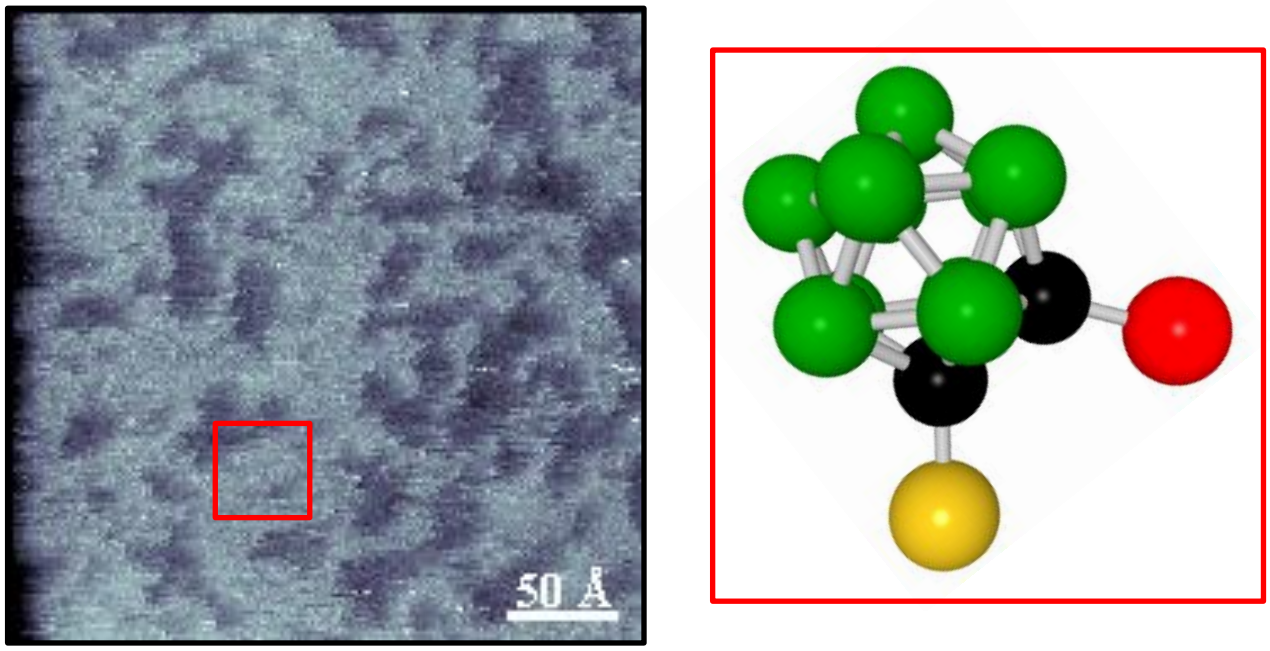

Figure 2.5: Scanning tunneling micrographs taken with an ambient STM of **12CDT** on Au{111}/mica after being exposed to 1 equivalences of 1 mM HNO_3. We predominantly found higher intensity protrusions, where only one thiol is bound to the surface enclosed in the red box. Image is recorded with V_s = 1 V and I_T = 100 pA. In the schematic to the right the unbound thiol is colored in red.

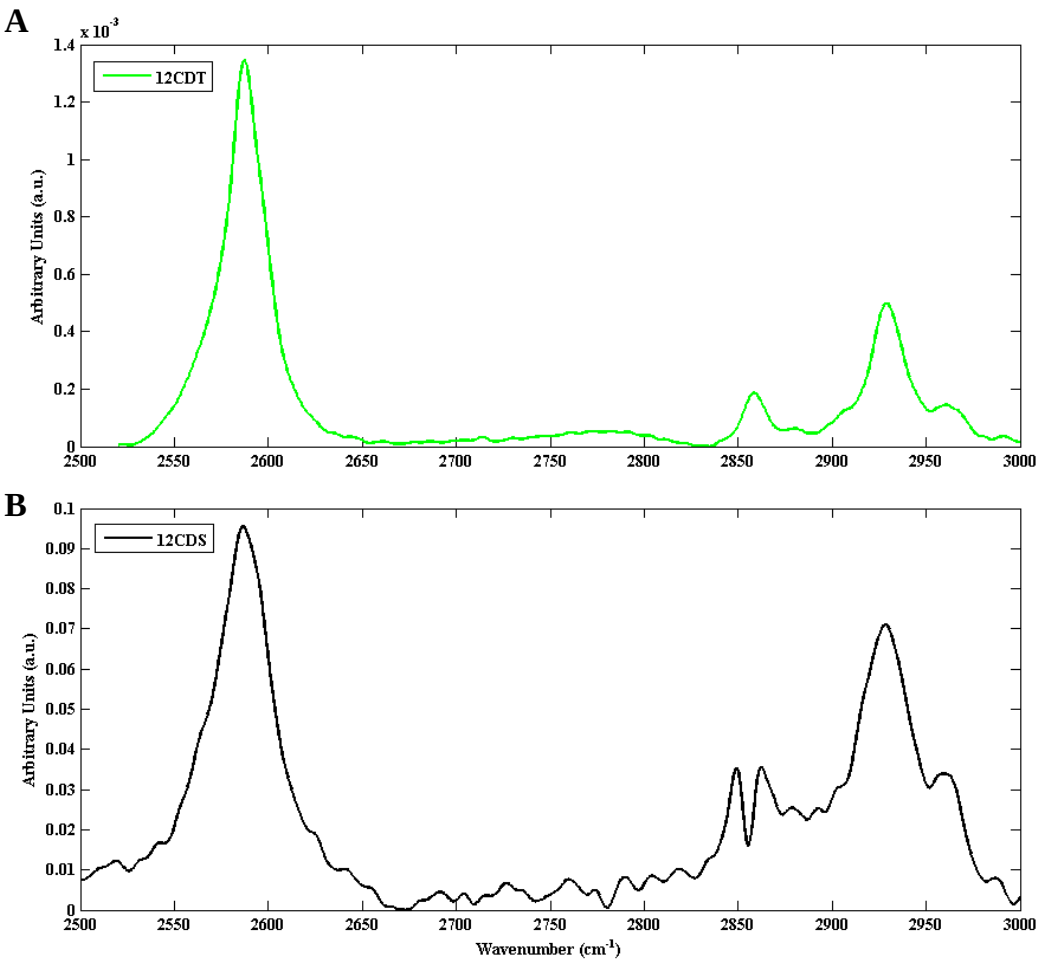

Figure 2.6: Grazing incidence FTIR spectra of **12CDT** (green) and **12CDS** (black) on Au{111}. **(A)** The spectra between 2500 – 3000 cm^{-1} for the **12CDT** SAM. **(B)** The spectra between 2500 – 3000 cm^{-1} for the **12CDS** SAM. The characteristic B-H stretch is centered around 2600 cm^{-1}.

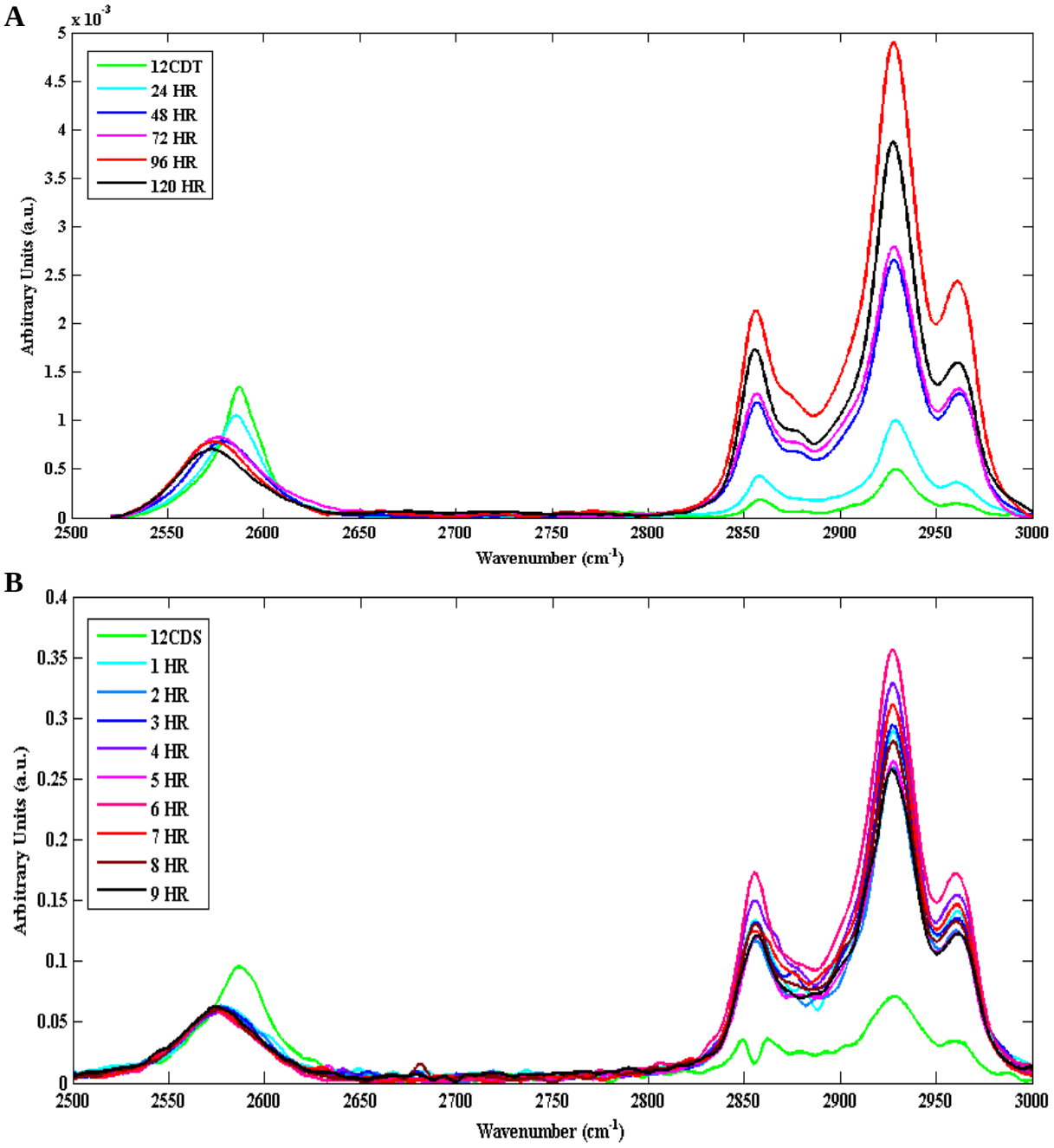

Figure 2.7: Vibrational studies of **(A) 12CDT** and **(B) 12CDS** SAMs during exposure to **C12**. **12CDT** and **12CDS** SAMs were exposed to a 1mM ethanolic **C12** solution and measured with FTIR at 24 h intervals for **12CDT** and at 1 h intervals for **12CDS** respectively. The characteristic B-H stretch is centered around 2600 cm^{-1} and observe a slight decrease in intensity over the course of the reaction, with an intensity increase to C-H stretches around 2900 cm^{-1}.

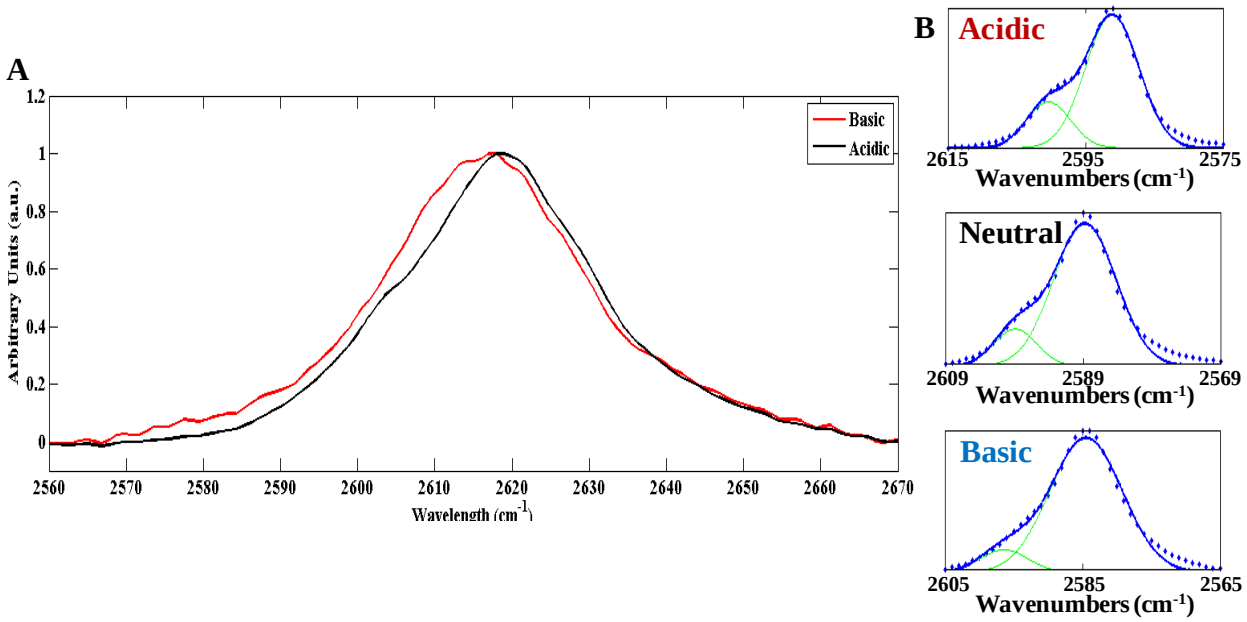

Figure 2.8: Grazing incidence FTIR spectra of acidic **12CDT** (black) and basic **12CDT** (red) on Au{111}. **(A)** The spectra between 2500 – 2700 cm^{-1} emphasizes the differences between acidic and basic **12CDS** SAMs. **(B)** Zoom deatils in spectra of B-H stretches at different pH conditions. The characteristic B-H stretch is centered around 2600 cm^{-1}.

2.5 References

1. Hohman, J. N.; Claridge, S. A.; Kim, M.; Weiss, P. S. Cage molecules for self-assembly. *Mater. Sci. Eng. R* **2010,** *70*, 188-208.

2. Heying, T. L.; Clark, S. L.; Hillman, M.; Goldstein, H. L.; Polak, R. J.; Mangold, D. J.; Szymansk, J. W.; Ager, J. W. A new series of organoboranes.1. Carboranes from reaction of decaborane with acetylenic compounds. *Inorg. Chem.***1963**, *2*, 1089–1092.

3. Fein, M. M.; Cohen, M. S.; Mayes, N.; Schwartz, N.; Bobinski, J. Carboranes. I. Preparation and chemistry of 1-isopropenylcarborane and its derivatives (a new family of stable clovoboranes). *Inorg. Chem.* **1963**, *2*, 1111–1115.

4. Zakharkin, L. I.; Stanko, V. I.; Brattsev, V. A.; Chapovsky, Y. A.; Ponomarenko, A. A.; Okhlobystin, O. Y.; Klimova, A. I. Synthesis properties of new class of organoboron compounds $B_{10}C_2H_{12}$ (Baren) its derivatives. *Dokl. Akad. Nauk SSSR* **1964**, *155*, 1119–1122.

5. Grimes, R. N. Carboranes. *Academic Press: New York*, **1970**.

6. Hohman, J. N.; Zhang, P.; Morin, E. I.; Han, P.; Kim, M.; Kurland, A. R.; McClanahan, P. D.; Balema, V. P.; Weiss, P. S. Self-assembly of carboranethiol isomers on au{111}: intermolecular interactions determined by molecular dipole orientations. *ACS Nano* **2009**, *3*, 527-536.

7. Baše, T.; Bastl, Z.; Hávranek, V.; Langecker, J.; Malina, V. Carboranedithiols: building blocks for self-assembled monolayers on copper surfaces. *Lagmuir* **2012,** *28* (34), 12518-12526.

8. Baše, T.; Bastl, Z.; Plzák, Z.; Grygar, T.; Plešek, J.; Carr, M. J.; Malina, V.; Šubrt, J.; Boháček, J.; Večerníková, E.; *et al.* Carboranethiol-modified gold surfaces. A study and comparison of modified cluster and flat surfaces. *Langmuir* **2005**, *21*, 7776-7785.

9. Baše, T.; Bastl, Z.; Šlouf, M.; Klementová, M.; Šubrt, J.; Vetushka, A.; Ledinský, M.; Fejfar, A.; Macháček, J.; Carr, M. J.; *et al.* Gold micrometer crystals modified with carboranethiol derivatives. *J. Phys. Chem. C* **2008**, *112*, 14446-14455.

10. Baše, T.; Bastl, Z.; Hávranek, V.; Lang, K.; Bould, J.; Londesborough, M. G. S.; Macháček, J.; Plešek, J. Carborane–thiol–silver interactions. A comparative study of the molecular protection of silver surfaces. *Surf. Coat. Technol.* **2010**, *204*, 2639-2646.

11. Bumm, L. A.; Arnold, J. J.; Charles, L. F.; Dunbar, T. D.; Allara, D. L.; Weiss, P. S. Directed self-assembly to create molecular terraces with molecularly sharp boundaries in organic monolayers. *J. Am Chem. Soc.* **1999**, *121*, 8017–8021.

12. Stipe, B. C.; Rezaei, M. A.; Ho, W. Single-molecule vibrational spectroscopy and microscopy. *Science* **1998**, *280*, 1732-1735.

13. Bumm, L. A.; Arnold, J. J.; Dunbar, T. D.; Allara, D. L.; Weiss, P. S. Electron transfer through organic molecules. *J. Phys. Chem. B* **1999**, *103*, 8122-8127.

14. Weiss, P. S.; Eigler, D. M. Site dependence of the apparent shape of a molecule in scanning tunneling micoscope images: benzene on pt{111}. *Phys. Rev. Lett.* **1993**, *71*, 3139-3142.

15. Hohman, J. N.; Kim, M.; Shüpback, B.; Kind, M.; Thomas, J. C.; Terfort, A.; Weiss, P. S. Dynamic double lattice of 1-adamantaneselenolate self-assembled monolayers on Au{111}. *J. Am. Chem. Soc.* **2011**, *133*, 19422-19431.

16. Lübben, J. F.; Baše, T.; Rupper, P.; Künniger, T.; Macháček, J.; Guimond, S. Tuning the surface potential of ag surfaces by chemisorption of oppositely-oriented thiolated carborane dipoles. *J. Colloid Interface Sci.* **2011**, *354*, 168-174.

17. Bould, J.; Macháček, J.; Londesborough, M. G. S.; Macias, R.; Kennedy, J. D.; Bastl, Z.; Rupper, P.; Baše, T. Decaborane thiols as building blocks for self-assembled monolayers on metal surfaces. *Inorg. Chem.* **2012**, *51*, 1685-1694.

CHAPTER 3

Self-Assembled *p*-Carborane Analogs of *p*-Mercantobenzoic Acid on Au{111}

3.1 Introduction

Self-assembled monolayers, or *qausi*-crystalline two-dimensional interfaces, enable tunable surface properties that can be incorporated in nanotechnology and materials development applications [1, 2]. Functionalization of essential building blocks used in SAMs has become a primary target in efforts to understand and to control materials at the molecular level, and using individual molecules for bottom-up surface assemblies with designer specific dimensions, chemical compositions, and physicochemical properties [3, 4]. Most 2D assemblies are comprised of organic molecules tethered to gold surfaces by means of thiol (-SH) / thiolate ($-S^-$) anchoring groups [5]. Recently, cage molecules have attracted special attention because of their rigid 3D architectures and ability to make structural and chemical modifications [6-12]. Thiolated derivatives of 12-vertex dicarba-*closo*-dodecaboranes have a nearly regular icosahedral molecular structure, with the general formula $(HS)_x$-$C_2B_{10}H_{12-x}$. They are representatives of inorganic cluster molecules belonging to this category [13-15]. Carboranes SAMs have shown to possess several advantages, such as higher stability against heating and chemical substitution and pristine monolayer formations which have fewer types and total numbers of defects compared to their organic counterparts [16, 17]. Fewer defects in carborane SAMs can be attributed to the higher axial isotropy of the carborane-based backbones compared to the organic aromatic varieties; which is the primary stimulus for our research. The large dipole moment in various isomeric carboranethiols allows tuning of the effective work function over a wide range of coinage metal substrates [2, 18-20]. Due to how robust these molecules are, they

have been embedded in functional organic-based SAMs due to their steric properties and wide frontier-orbital energy gaps [8, 21].

New synthetic strategies have been proposed for the preparation of the dicarba-*closo*-dodecaborane derivatives substituted at both carbon and boron positions as routes to new precursors and ligands for coordination compounds and metal surfaces [22-24]. These concerted efforts are a systematic approach towards compiling a library of functionalized carborane cluster compounds with potential use as surface modifiers with innovative traits. The primary focus of this research is to probe this library of potential carborane-based building blocks through targeted functionalization which special attention to materials and supramolecular chemistry. In the context of SAMs, functionalized *p*-isomers are garnering interest due to their applications in ultra-thin films and directing nano-architectures [2, 7, 9, 15, 25].

In this chapter, we report on the characterization of a new cage thiol with a carboxyl functional group that is suitable for further chemical modification on exposed SAM surfaces. Inspired by the recent successes in the functionalization and patterning of *p*-mercaptobenzoic acid, which itself has proven to be effective in surface functionalization tempted us to investigate the cluster analogue of *p*-mercaptobenzoic acid (1-HS-4-COOH-C_6H_4) in more detail as a possible modifier of gold surfaces [26-30]. Another reason of interest for using this new cage building block, 1-HS-12-COOH-1,12-$C_2B_{10}H_{10}$ (**A'**) in SAMs is due to its high axial symmetry. When compared to the benzene ring of *p*-mercaptobenzoic acid, the larger steric demands of the carborane cage enable greater separation spacings of the carboxylic functional groups in two dimensions. This new carborane derivative has a particularly attractive use as a functional capping ligand for gold colloidal particles or as a ligand for transition metal complexes. We compare the structure of (**A'**) to its precursor 1-HS-1,12-$C_2B_{10}H_{11}$ (**A**) as the initial step for

examination, where micrographs obtained by STM are discussed. These two SAM constituents on gold have been quantified using contact angle measurements in order to study the surface wetting characteristics.

3.2 Results and Discussion

3.2.1 Scanning Tunneling Microscopy

Two-dimensional lattices of **A** on Au{111} were measured in ambient conditions and used its lattice as a backbone in order to trap islands of **A'** in a mixed (1:10, **A'**:**A**) SAM. Single-component SAMs of **A'** were tough to image with molecular resolution at ambient conditions due to the free rotation of the hydrophilic COOH functional groups around the five-fold symmetry axis of the *p*-carborane cage and the likelihood of adsorbing water.

Scanning tunneling microscopy can be employed in order to probe exposed interfaces of conductive thin films with molecular precision [31, 32]. Acquired data was imaged in constant-current mode, which represents a convolution of topography and electronic structure [33, 34]. Single-component monolayers of **A** on Au{111} form into two-phase hexagonally close-packed arrays with a 7.0 ± 0.4 Å nearest neighbor spacing (Figures 3.1 and 3.2). The most probable unit cell structures are: $(\sqrt{93}\times\sqrt{93})R21.05°$, $(\sqrt{97}\times\sqrt{97})R15.30°$, and (5×5), with nearest-neighbor spacings of 6.94, 7.09, and 7.20 Å, respectively. It is possible that the measured SAMs may compete between any of the above structures; incommensurate lattices are also possible [35, 36]. Simple density functional theory (DFT) calculations of a 2D array of **A**, estimate the steric demands of the cage moiety and predict nearest-neighbor intermolecular distances of 7.26 Å, as seen in Figure 3.3. This calculated distance best matches the (5×5) unit cell structure. Calculated lattice constants are different due to the five-fold symmetry of the *para*-carborane cage. The two distinct phases observed have a apparent height difference of 1.0 ± 0.3 Å. We reason that the less

protruding apparent height features are thiolate-bound moieties and the more protruding apparent height features are thiol moieties. In-depth analyses across many different areas and samples ($n_{samples} > 3$) shows an average coverage of 5.1 ± 1.4 % for the thiol-bound moiety and 95 ± 2.5 % average coverage for the thiolate-bound moiety as shown in Figure 3.4. This demonstrates that the thiolate bound moiety is more dominant and favored over the thiol-bound moiety. Previous STM studies have shown only thiolate-bound states for the isomeric 1-HS-1,7-$C_2B_{10}H_{11}$ [17].

Mixed component SAMs proved valuable in promoting sparse **A'** monolayer formation. Scanning tunneling micrographs reveal that co-deposited SAMs show dispersed islands of **A'**, in regions where the lattice of the **A** backbone is confirmed and **A'** is resolved in apparent height. Hydrogen bonding among **A'** molecules in solution may play a significant role in its 2D packing, due to intermolecular forces causing the formation of island aggregates. Scanning tunneling micrographs show an apparent height difference of 1.2 ± 0.2 Å, under specific imaging conditions used, the carboxyl moiety is topographically more protruding (Figure 3.5). Imaging reveals local ordering of the **A** backbone, where minimal defects surround **A'** patches, which implies that the **A'** moieties have adopted the same 7 Å nearest neighbor spacing of the backbone monolayer. Creating patterned substrates that contain chemically functionalized islands dispersed throughout the monolayer can possibly take advantage and make use of this system. [15, 29, 37-47].

3.2.2 Dynamic contact angles

A fundamental approach to macroscopic characterization of modified surfaces is the measurement of dynamic contact angles, which provides information about the hydrophilic and hydrophobic surface character [7, 48]. Gold surfaces were modified with derivatives **A** and **A'**

demonstrating advancing and receding wetting angle values of 87.5° and 76.8° for SAMs of **A**, respectively, and 30.0° and 24.8° for SAMs of **A'**, respectively (Table 3.1). These values are considerably different and reveal the hydrophilic character of **A'** SAMs in comparison to **A** SAMs. The hydrophilic character of **A'** is predictable due to the addition of the exposed COOH functional groups. These results are consistent with the orientation of the molecules on gold surfaces as anticipated by the carboxylic functional groups interacting weakly with the underlying gold surface due to being at the exposed surface and the thiol/thiolate groups affixing the molecules to the substrate.

3.3 Conclusions and Prospects

Derived from 12-vertex *p*-carborane, a new bifunctional cage molecule was characterized using various structural methods. This new building block has higher axial symmetry and greater steric demands compared to its planar organic analogue, *p*-mercaptobenzoic acid. When employed in SAMs on Au{111}, these bulky molecules organize themselves into hexagonal close-packed arrays with nearest-neighbor distances of 7.0 ± 0.4 Å. These molecules assemble into close-packed rows with nearest neighbor distances of only 6.635 Å in single crystals. Various 2D arrangements cannot pack that efficiently due to the five-fold symmetry axis of the *p*-carborane cage. Consequently, steric demands and axial symmetry both influence packing on Au{111} surfaces. Mixed SAMs involving this new cage molecule and its non-carboxylated precursor reveal that this system can be used to prepare pristine monolayers that have separated islands with additional functional groups on top, which can then be used in surface patterning. Assembling these new molecules on gold have shown that they prefer to adsorb as thiolates, with a small percentage adsorbing as thiols. Our results are consistent with previous studies of mono-thiolated *o*- and *m*-carboranes, which dissociate more easily than mono-thiolated

p-carborane [17, 18]. The presence of the COOH group on top of the *p*-carborane has been revealed to have a negligible effect on the interactions between the SH group and the substrate. Due to the cage, this molecule effectively isolates the two functional groups, in spite of its *pseudo*-aromatic character.

In relationship to its organic analog, *p*-mercaptobenzoic acid, **A'** yields SAMs with several interesting properties, resulting from the fact that the carborane cage provides more rigid and have larger lattice spacings than alkyl or aryl substituents [7]. Similarly modifying the *m*- and *o*- isomers would allow for increased backbone interaction strengths ready for surface functionalization [49]. Recently similar *p*-carborane derivatives were used as building blocks for metal-organic frameworks and their results correlate well with observations seen here [36, 45]. Combining both kinds of carborane-based building blocks provide a basis for creating porous 3D structures such as *p*-carboranylcarboxylate metal-organic frameworks.

3.4 Materials and Methods

3.4.1 Monolayer preparation

The chemical, 1-HS-1,12-$C_2B_{10}H_{11}$ (**A**) was prepared based off previous literature [50, 51]. Benzene and other solvents (Sigma-Aldrich, St. Louis, MO) for STM experiments were used as received. For STM, both pure and co-deposited **A** and (1:10) **A'**:**A** SAMs were deposited from solution onto Au{111} substrates (Agilent, Santa Clara, CA). The Au{111} substrates were hydrogen flame annealed and placed into a 1 mM benzoic solution of either **A** or **A'**:**A** (1:10). Samples were heated for 24 h at 78 °C in a Barnstead Thermolyne 1400 furnace (ThermoFisher Scientific, Waltham, MA). Samples were removed from solution and then cleaned with neat benzene and dried with a stream of nitrogen gas before loading into the custom-built ambient microscope.

3.4.2 Scanning tunneling microscopy

All STM measurements were conducted using a custom beetle-style microscope at ambient conditions [7, 52]. Platinum/iridium tip wire (80:20) was used (Alfa Aesar, Ward Hill, MA). Gains for the piezoelectric scanners were calibrated using the lattice constant of the 1-dodecanethiolate SAM on Au{111} and then checked against the expected spacings of SAMs of **A**. Samples were held within a -1 to -0.1 V bias range, and 256 × 256 pixel images were acquired in constant-current mode at a tunneling current of 100 pA.

3.4.3 Water contact-angle measurements

Contact angle measurements were made using a custom-built goniometer, for **A** and **A'** SAMs on Au/Si. This apparatus uses a CCD camera equipped with an InfiniStix (Hitachi Ltd., Tokyo, Japan) 0.50× magnification, 94 mm focal length lens. Data acquisition and contact angle measurements used FTA 1000 B software, produced by First Ten Angstroms, Inc. (Portsmouith, VA).

Contact angle data were collected using a dynamic sessile drop method, where a sample is placed in close proximity to the tip of the needle. Reproducible 2 µL droplets were deposited and manipulated using a 0.5 mL Luer Lock syringe (Cole-Palmer, Vernon Hills, IL) and a 30 gauge needle. Once deposited on the sample, the needle was carefully positioned in the center of the drop without deforming its shape. The volume was then increased to 6 µL and an image was captured for the advancing contact angle. The drop size was increased to 8 µL and then decreased to 6 µL and another image was captured for the receding contact angle. All these measurements were collected on an automated system with images collected at 60 frames per second for seven cycles and each data point was an average of 5 measurements per sample for 3 samples.

3.4.4 Computational details

Using the Abinit package, density functional theory in the plane wave basis was employed to calculate periodic structures [53-55]. For the unit cell, two dimensions of interest were set to 7.2 Å, at an angle of 60°, and optimized along with the molecular geometry. The third dimension for this 2D cell was fixed to 30 Å. General gradient approximation exchange-correlation functions of Perdew, Burke, and Ernzerhof were used, and the atoms were described by the projector-augmented wave approximation with the atomic data downloaded from the Abinit web [56-59]. The cut-off energy was set to 15 Ha for the plane-wave basis and 50 Ha for the double grid cutoff. The 3×3×1 Monkhorst-Pack k-point grid was generated automatically so as not to introduce incorrect contributions to the Fourier transform of real space vectors shorter than 50 Å [60].

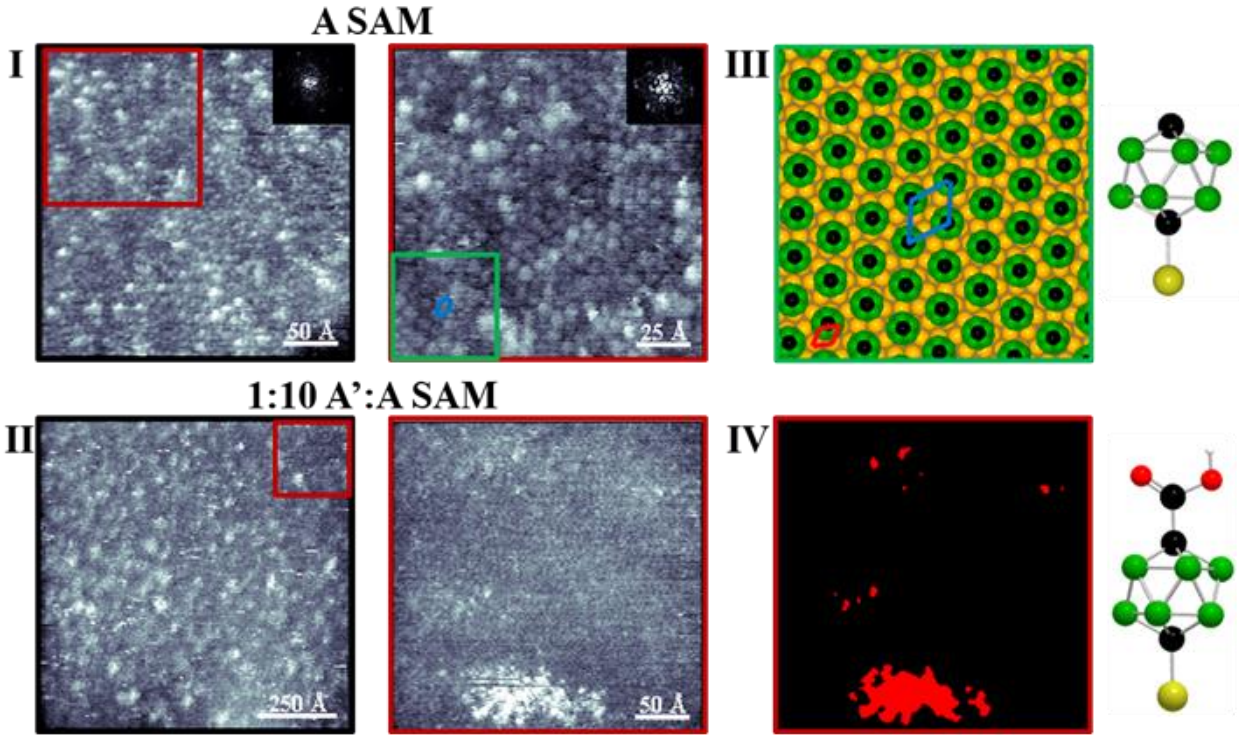

Figure 3.1. **I** Scanning tunneling micrographs of **A** at 300 Å × 300 Å and 150 Å × 150 Å. A Fourier transform is shown in each inset depicting a hexagonally close-packed lattice with a nearest-neighbor spacing of 7.0 ± 0.4 Å. **II** Scanning tunneling micrographs of a co-deposited (1:10, **A'**:**A**) SAM, at 1000 Å × 1000 Å and 300 Å × 300 Å scan sizes. Images were recorded with V_S = 1.0 V and I_T = 100 pA. **III** Structural schematic representing the observed lattice (blue lines indicate nearest neighbors) with respect to the underlying (1×1) unit cell (red rhombus) of the unreconstructed Au{111} substrate. **IV** Thresholding enables the isolation of **A'** regions that are highlighted in red.

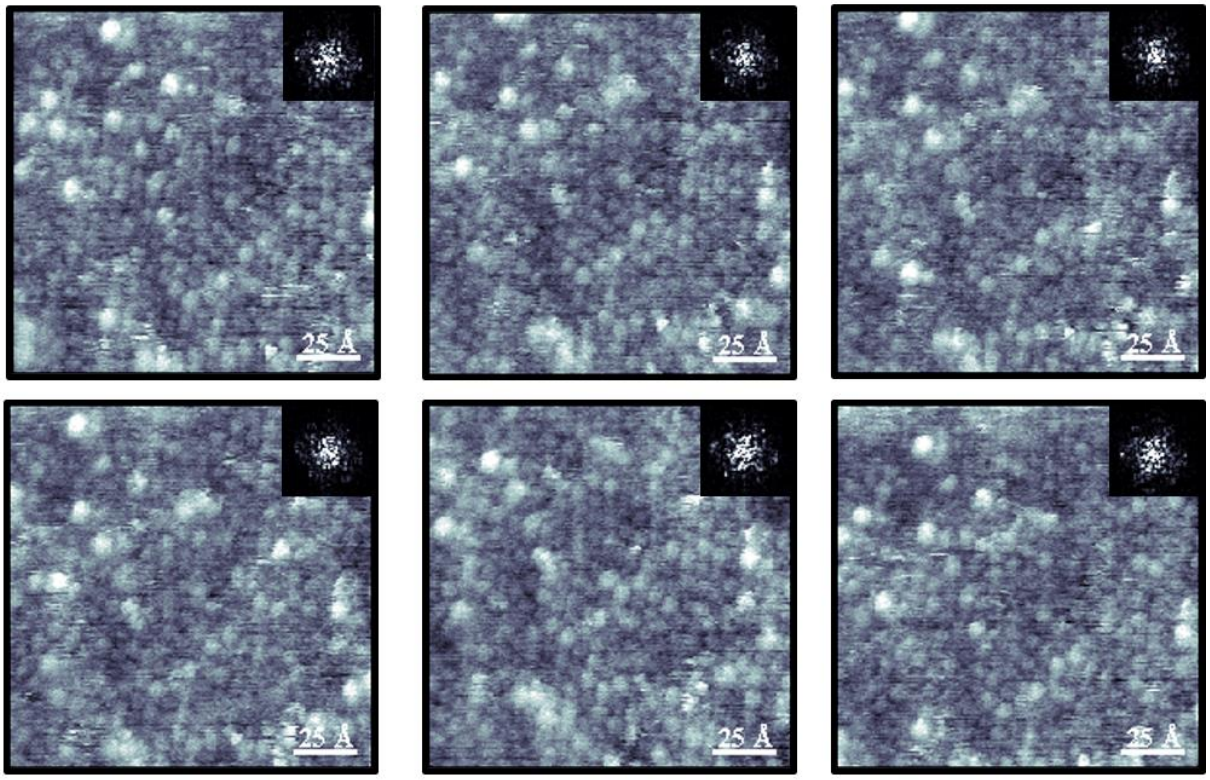

Figure 3.2: Scanning tunneling micrographs, that measure hexagonally close-packed arrays of **A** on Au{111}. Both the thiol (higher intensity protrusions) and thiolate (lower intensity protrusions) bound moieties are resolved, and show an average nearest neighbor distance of 7.1 ± 1.1 Å, which was obtained from the Fourier transform shown in each inset. Images were recorded with V_S = 1.0 V and I_T = 100 pA.

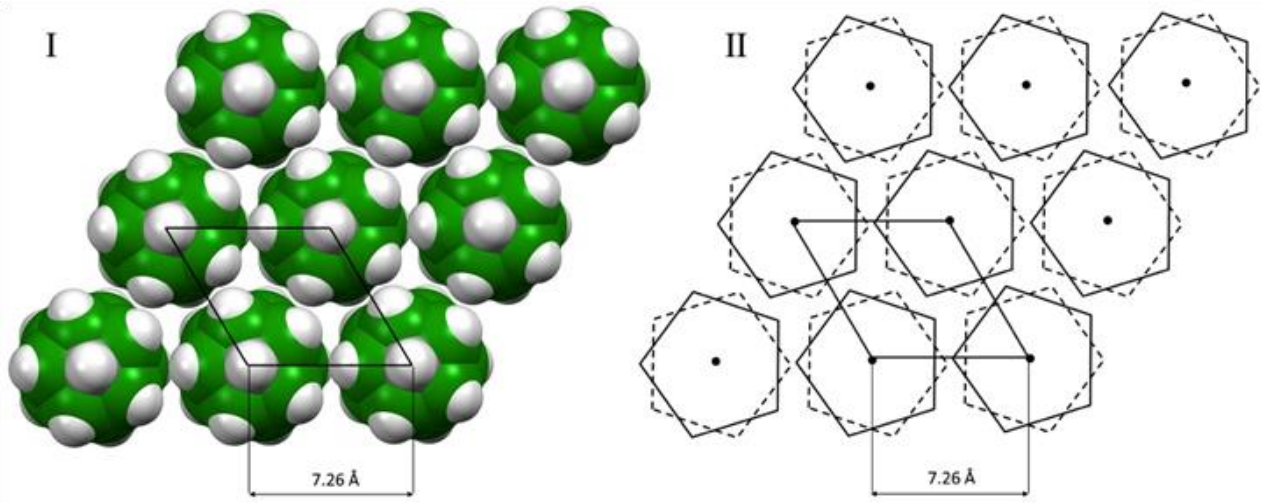

Figure 3.3: Using density functional theory, we calculated a 2D array of molecules **A** showing a close-packed structure with lattice parameters of 7.26 Å × 7.27 Å (α = 60.07°). (**I**) Space-filling model and (**II**) a schematic representation.

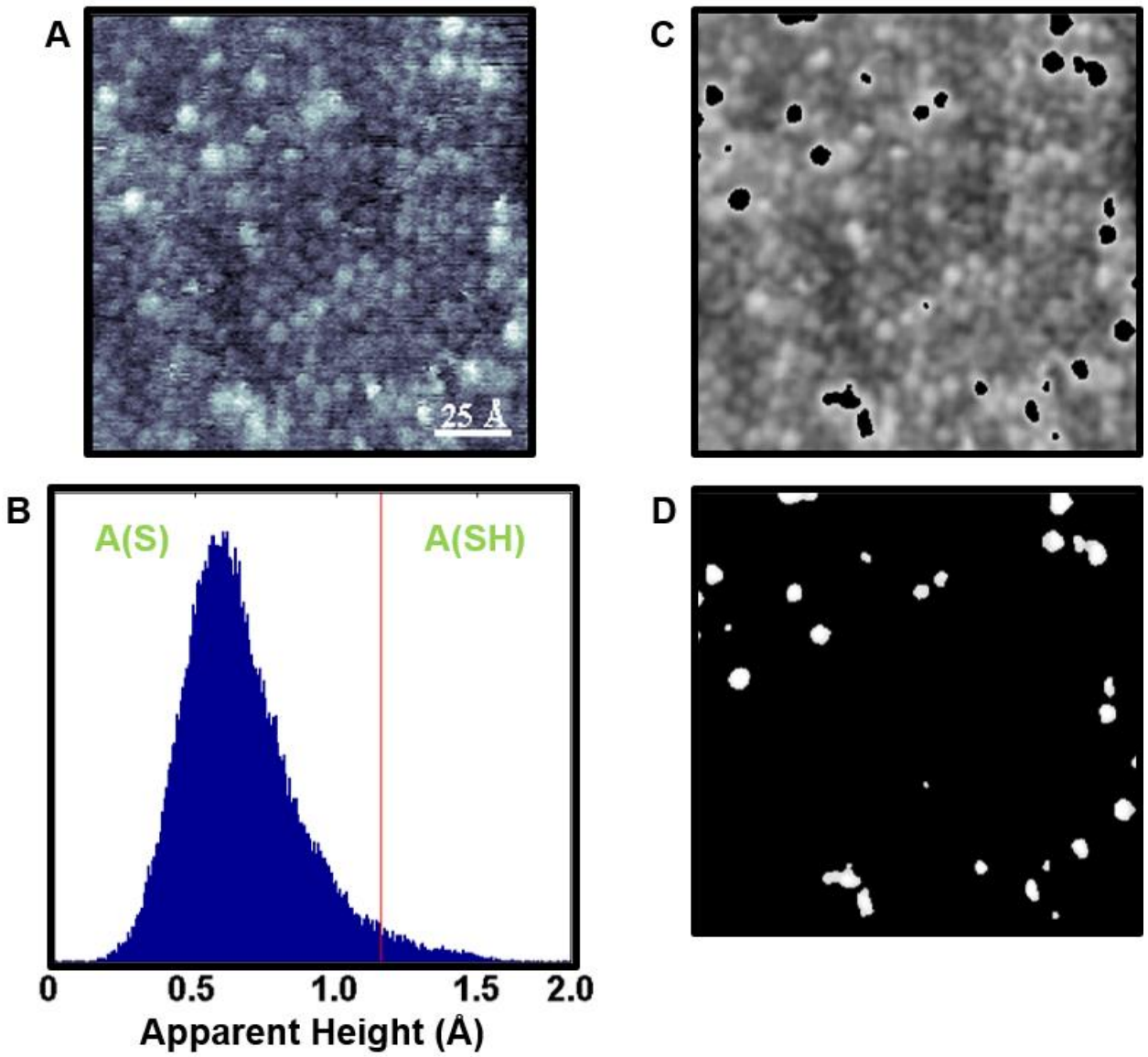

Figure 3.4: (A) Scanning tunneling micrograph of **A** deposited on Au{111} with its **(B)** apparent height histogram. In **(C)** and **(D)** respectively, the STM image has been thresholded by separating pixels that differ in average apparent height. Masking techniques were performed in Matlab, in order to separate and to analyze independent regions of **A** bound as thiols and thiolates. The summed average percent of **A** (bound as thiolate) is 95% (5% **A**, bound as thiol), suggesting that the cleaved hydrogen-sulfur surface bonding is energetically favorable in comparison to the non-cleaved bonding scheme.

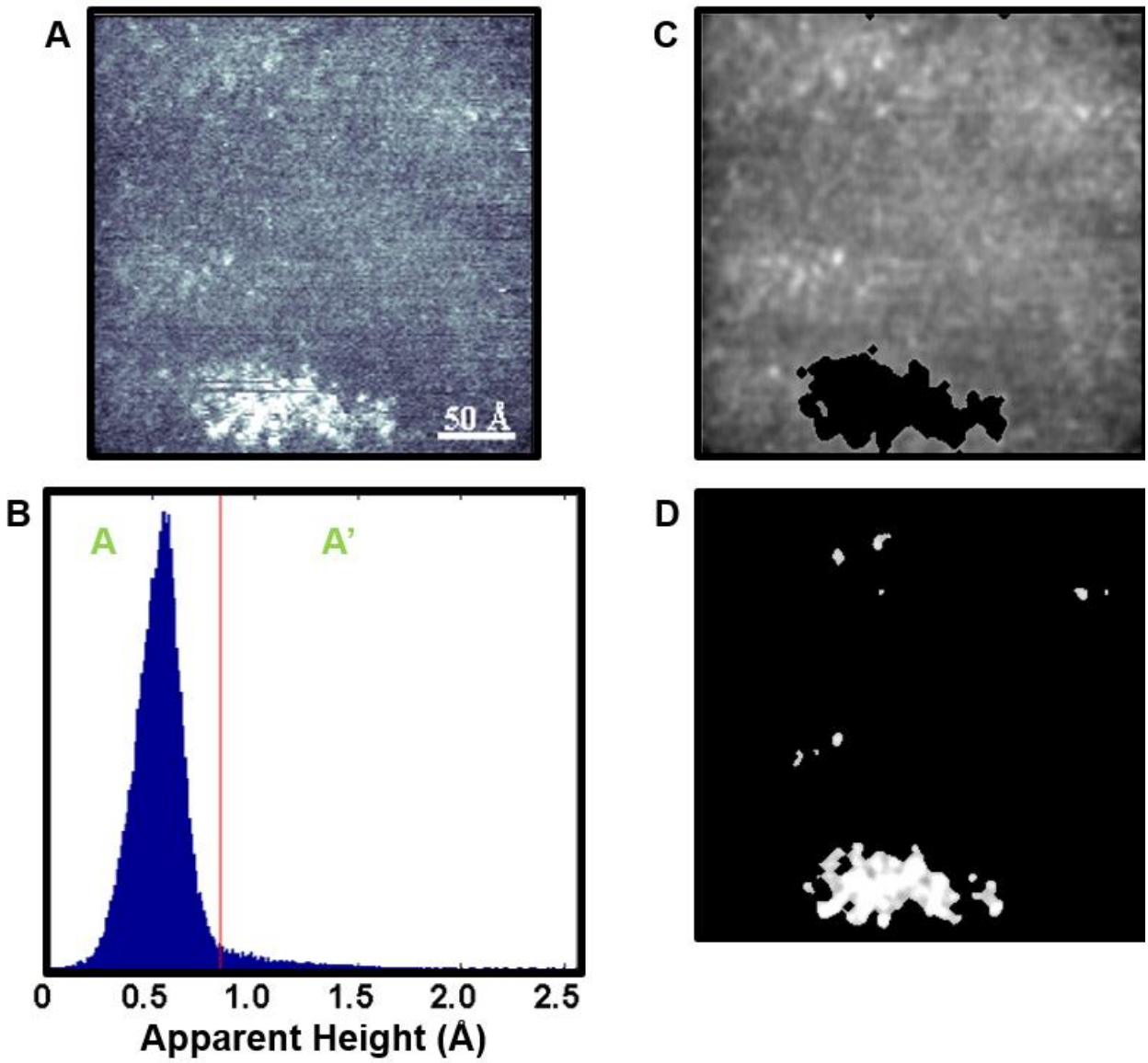

Figure 3.5: (A) Scanning tunneling micrograph of 1:10 (**A'**:**A**) solution deposited SAM, with measured coverages consistent with deposited ratios, on a Au{111} substrate with its **(B)** apparent height histogram. In **(C)** and **(D)** respectively, the STM image is thresholded by differences in apparent height. Masking techniques were performed in Matlab, in order to separate and to analyze independent regions of **A** and **A'**. The **A'** moiety displays a larger apparent height of 1.2 ± 0.2 Å due to protruding carboxyl groups.

Table 3.1: Advancing (Θ_{adv}) and receding (Θ_{rec}) contact angles of water on **A** and **A'** SAMs on Au. All angles are in degrees with standard deviations shown in parentheses.

Sample	Θ_{adv}	Θ_{rec}
A SAM	87.5 (0.3)	76.8 (0.2)
A' SAM	30.0 (0.1)	24.8 (0.1)

Θ_{adv} and Θ_{rec}: advancing and receding contact angles of water, respectively.

3.5 References

1. Smith, R. K.; Lewis, P. A.; Weiss, P. S. Patterning self-assembled monolayers. *Prog. Surf. Sci.* **2004,** *75*, 1-68.

2. Kim, J.; Rim, Y. S.; Liu, Y.; Serino, A. C.; Thomas, J. C.; Chen, H.; Yang, Y.; Weiss, P. S. Interface control in organic electronics using mixed monolayers of carboranethiol isomers. *Nano Lett.* **2014,** *14*, 2946-2951.

3. Love, J. C.; Estroff, L. A.; Kriebel, J. K.; Nuzzo, R. G.; Whitesides, G. M. Self-assembled monolayers of thiolates on metals as a form of nanotechnology. *Chem. Rev.* **2005,** *105*, 1103-1169.

4. Gooding, J. J.; Ciampi, S. The molecular level modification of surfaces: from self-assembled monolayers to complex molecular assemblies. *Chem. Soc. Rev.* **2011**, *40*, 2704-2718.

5. Ulman, A. Formation and structure of self-assembled monolayers. *Chem. Rev.* **1996,** *96*, 1533-1554.

6. Fujii, S.; Akiba, U.; Fujihira, M. Geometry for self-assembling of spherical hydrocarbon cages with methane thiolates on Au(111). *J. Am. Chem. Soc.* **2002**, *124*, 13629-13635.

7. Hohman, J. N.; Claridge, S. A.; Kim, M.; Weiss, P. S. Cage molecules for self-assembly. *Mater. Sci. Eng. R* **2010,** *70*, 188-208.

8. von Wrochem, F.; Scholz, F.; Gao, D.; Nothofer, H.-G.; Yasuda, A.; Wessels, J. M.; Roy, S.; Chen, X.; Michl, J. High-band-gap polycrystalline monolayers of a 12-vertex *p*-carborane on Au(111). *J. Phys. Chem.* **2010,** *1*, 3471-3477.

9. Hohman, J. N.; Kim, M.; Shüpback, B.; Kind, M.; Thomas, J. C.; Terfort, A.; Weiss, P. S. Dynamic double lattice of 1-adamantaneselenolate self-assembled monolayers on Au{111}. *J. Am. Chem. Soc.* **2011**, *133*, 19422-19431.

10. Spokoyny, A. M.; Machan, C. W.; Clingerman, D. J.; Rosen, M. S.; Wiester, M. J.; Kennedy, R. D.; Stern, C. L.; Sarjeant, A. A.; Mirkin, C. A. A coordination chemistry dichotomy for icosahedral carborane-based ligands. *Nat. Chem.* **2011,** *3*, 590-596.

11. Katano, S.; Kim, Y.; Kitagawa, T.; Kawai, M. Tailoring electronic states of a single molecule using adamantane-based molecular tripods. *Phys. Chem. Chem. Phys.* **2013**, *15*, 14229-14233.

12. Wann, D. A.; Lane, P. D.; Robertson, H. E.; Baše, T.; Hnyk, D. The gaseous structure of *closo*-9,12-$(sh)_2$-1,2-$c_2b_{10}h_{10}$, a modifier of gold surfaces, as determined using electron diffraction and computational methods. *Dalton Trans.* **2013**, *42*, 12015-12019.

13. Yeager, L. J.; Saeki, F.; Shelley, K.; Hawthorne, M. F.; Garrell, R. A new class of self-assembled monolayers: *closo*-$B_{12}H_{11}S^{3-}$ on gold. *J. Am. Chem. Soc.* **1998**, *120*, 9961-9962.

14. Scholz, F.; Nothofer, H.-G.; Wessels, J. M.; Nelles, G.; von Wrochem, F.; Roy, S.; Chen, X.; Michl, J. Permethylated 12-vertex *p*-carborane self-assembled monolayers. *J. Phys. Chem. C* **2011**, *115*, 22998-23007.

15. Claridge, S. A.; Liao, W. S.; Thomas, J. C.; Zhao, Y.; Cao, H. H.; Cheunkar, S.; Serino, A. C.; Andrews, A. M.; Weiss, P. S. From the bottom up: dimensional control and characterization in molecular monolayers. *Chem. Soc. Rev.* **2013,** *42*, 2725-2745.

16. Baše, T.; Bastl, Z.; Plzák, Z.; Grygar, T.; Plešek, J.; Carr, M. J.; Malina, V.; Šubrt, J.; Boháček, J.; Večerníková, E.; *et al.* Carboranethiol-modified gold surfaces. A study and comparison of modified cluster and flat surfaces. *Langmuir* **2005,** *21*, 7776-7785.

17. Hohman, J. N.; Zhang, P.; Morin, E. I.; Han, P.; Kim, M.; Kurland, A. R.; McClanahan, P. D.; Balema, V. P.; Weiss, P. S. Self-assembly of carboranethiol isomers on au{111}: intermolecular interactions determined by molecular dipole orientations. *ACS Nano* **2009,** *3*, 527-536.

18. Baše, T.; Bastl, Z.; Šlouf, M.; Klementová, M.; Šubrt, J.; Vetushka, A.; Ledinský, M.; Fejfar, A.; Macháček, J.; Carr, M. J.; *et al.* Gold micrometer crystals modified with carboranethiol derivatives. *J. Phys. Chem. C* **2008,** *112*, 14446-14455.

19. Baše, T.; Bastl, Z.; Hávranek, V.; Lang, K.; Bould, J.; Londesborough, M. G. S.; Macháček, J.; Plešek, J. Carborane–thiol–silver interactions. A comparative study of the molecular protection of silver surfaces. *Surf. Coat. Technol.* **2010**, *204*, 2639-2646.

20. Lübben, J. F.; Baše, T.; Rupper, P.; Künniger, T.; Macháček, J.; Guimond, S. Tuning the surface potential of ag surfaces by chemisorption of oppositely-oriented thiolated carborane dipoles. *J. Colloid Interface Sci.* **2011**, *354*, 168-174.

21. Ito, M.; Wei, T. X.; Chen, P.-L.; Akiyama, H.; Matsumoto, M.; Tamada, K.; Yamamoto, Y. A novel method for creation of free volume in a one-component self-assembled monolayer. Dramatic size effect of *para*-carborane. *J. Mater. Chem.* **2005**, *15*, 478-483.

22. Langecker, J.; Fejfarová, K.; Dušek, M.; Rentsch, D.; Baše, T. Carbon-substituted 9,12-dimercapto-1,2-dicarba-*closo*-dodecaboranes via a 9,12-bis(methoxy-methylthio)-1,2-dicarba-*closo*-dodecaborane precursor. *Polyhedron* **2012**, *45*, 144-151.

23. Frank, R.; Boehnke, S.; Aliev, A.; Hey-Hawkins, E. From *ortho*-carbaborane-9-thiol towards new building blocks. *Polyhedron* **2012**, *39*, 9-13.

24. Kabytaev, K. Z.; Everett, T. A.; Safronov, A. V.; Sevryugina, Y. V.; Jalisatgi, S. S.; Hawthorne, M. F. B-mercaptocarboranes: a new synthetic route. *Eur. J. Inorg. Chem.* **2013**, 2488-2491.

25. Weiss, P. S. Functional molecules and assemblies in controlled environments: formation and measurements. *Acc. Chem. Res.* **2008,** *41*, 1772-1781.

26. Ackerson, C. J.; Jadzinsky, P. D.; Kornberg, R. D. Thiolate ligands for synthesis of water-soluble gold clusters. *J. Am. Chem. Soc.* **2005**, *127*, 6550-6551.

27. Jadzinsky, P. D.; Calero, G.; Ackerson, C. J.; Bushnell, D. A.; Kornberg, R. D. Structure of a thiol monolayer-protected gold nanoparticle at 1.1 Å resolution. *Science* **2007**, *318*, 430-433.

28. Walter, M.; Akola, J.; Lopez-Acevedo, O.; Jadzinsky, P. D.; Calero, G.; Ackerson, C. J.; Whetten, R. L.; Grönbeck, H.; Häkkinen, H. A unified view of ligand-protected gold clusters as superatom complexes. *Proc. Natl. Acad. Sci.* **2008**, *105*, 9157-9162.

29. Saavedra, H. M.; Thompson, C. M.; Hohman, J. N.; Crespi, V. H.; Weiss, P. S. Reversible lability by *in situ* reaction of self-assembled monolayers. *J. Am. Chem. Soc.* **2009**, *131*, 2252-2259.

30. Saavedra, H. M.; Mullen, T. J.; Zhang, P. P.; Dewey, D. C.; Claridge, S. A.; Weiss, P. S. Hybrid approaches in nanolithography. *Rep. Prog. Phys.* **2010,** *73*, 036501.

31. Claridge, S. A.; Schwartz, J. J.; Weiss, P. S. Electrons, photons, and force: quantitative single-molecule measurements from physics to biology. *ACS Nano* **2011,** *5*, 693-729.

32. Hohman, J. N.; Thomas, J. C.; Zhao, Y.; Auluck, H.; Kim, M.; Vijselaar, W. J. C.; Kommeran, S.; Terfort, A.; Weiss, P. S. Exchange reactions between alkanethiolates and alkaneselenols on Au{111}. *J. Am. Chem. Soc.* **2014**, *136*, 8110-8121.

33. Han, P.; Kurland, A. R.; Giordano, A. N.; Nanayakkara, S. U.; Blake, M. M.; Pochas, C. M.; Weiss, P. S. Heads and tails: simultaneous exposed and buried interface imaging of monolayers. *ACS Nano* **2009,** *3*, 3115-3121.

34. Claridge, S. A.; Thomas, J. C.; Silverman, M. A.; Schwartz, J. J.; Yang, Y.; Wang, C.; Weiss, P. S. Differentiating amino acid residues and side chain orientations in peptides using scanning tunneling microscopy. *J. Am. Chem. Soc.* **2013,** *135*, 18528-18535.

35. Fujii, S.; Akiba, U.; Fujihira, M. Geometry for self-assembling of spherical hydrocarbon cages with methane thiolates on Au(111). *J. Am. Chem. Soc.* **2002**, *124*, 13629–13635.

36. Farha, O.; Spokoyny, A. M.; Mulfort, K. L.; Hawthorne, M. F.; Mirkin, C. A.; Hupp, J. T. Synthesis and hydrogen sorption properties of carborane based metal-organic framework materials. *J. Am. Chem. Soc.* **2007**, *129*, 12680–12681.

37. Stranick, S. J.; Parakh, A. N.; Tao, Y.-T.; Allara, D. L.; Weiss, P. S. Phase separation of mixed-composition self-assembled monolayers into nanometer scale molecular domains. *J. Phys. Chem.* **1994,** *98*, 7636-7646.

38. Weck, M.; Jackiw, J. J.; Rossi, R. R.; Weiss, P. S.; Grubbs, R. H. Ring-opening metathesis polymerization from surfaces. *J. Am. Chem. Soc.* **1999**, *121*, 4088–4089.

39. Liu, G.-Y.; Xu, S.; Qian, Y. Nanofabrication of self-assembled monolayers using scanning probe lithography. *Acc. Chem. Res.* **2000**, *33*, 457–466.

40. Zhang, H.; Li, Z.; Mirkin, C. A. Dip-pen nanolithography-based methodology for preparing arrays of nanostructures functionalized with oligonucleotides. *Adv. Mater.* **2002**, 14, 1472–1474.

41. Smith, R. K.; Lewis, P. A.; Weiss, P. S. Patterning self-assembled monolayers. *Prog. Surf. Sci.* **2004,** *75*, 1-68.

42. Srinivasan, C.; Mullen, T. J.; Hohman, J. N.; Anderson, M. E.; Dameron, A. A.; Andrews, A. M.; Dickey, E. C.; Horn, M. W.; Weiss, P. S. Scanning electron microscopy of nanoscale chemical patterns. *ACS Nano* **2007**, *1*, 191–201.

43. Mullen, T. J.; Srinivasan, C.; Hohman, J. N.; Gillmor, S. D.; Shuster, M. J.; Horn, M. W.; Andrews, A. M.; Weiss, P. S. Microcontact insertion printing. *Appl. Phys. Lett.* **2007**, *90*, 063114.

44. Shuster, M. J.; Vaish, A.; Szapacs, M. E.; Anderson, M. E.; Weiss, P. S.; Andrews, A. M. Biospecific recognition of tethered small molecules diluted in self-assembled monolayers. *Adv. Mater.* **2008**, *20*, 164-167.

45. Spokoyny, A. M.; Kim, D.; Sumrein, A.; Mirkin, C. A. Infinite coordination polymer nano- and microparticle structures. *Chem. Soc. Rev.* **2009**, *38*, 1218–1227.

46. Liao, W.-S.; Cheunkar, S.; Cao, H.; Bednar, H.; Weiss, P. S.; Andrews, A. M. Subtractive patterning *via* chemical lift-off lithography. *Science* **2012**, *337*, 1517-1521.

47. Zheng, Y. B.; Pathem, B. K.; Hohman, J. N.; Thomas, J. C.; Kim, M. H.; Weiss, P. S. Photoresponsive molecules in well-defined nanoscale environments. *Adv. Mater.* **2013**, ***25***, 302–312.

48. Vaish, A; Shuster, M. J.; Cheunkar, S.; Weiss, P. S.; Andrews, A. M. Tuning stamp surface energy for soft lithography of polar molecules to fabricate bioactive small-molecule microarrays. *Small* **2011**, ***7***, 1471–1479.

49. Thomas, J. C.; Schwartz, J. J.; Hohman, J. N.; Claridge, S. A.; Auluck, H. S.; Serino, A. C.; Spokoyny, A. M.; Tran, G.; Kelly, K. F.; Mirkin, C. A.; Gilles, J.; Osher, S. J.; Weiss, P. S. Defect-tolerant aligned dipoles within two-dimensional plastic lattices. *ACS Nano*. **2015**, *9*, 4734–4742.

50. Plešek, J.; Heřmánek, S. Experimental evaluation of charge distribution on particular skeletal atoms in icosahedral carboranes by means of HS-derivatives. *Collect. Czech. Chem. Commun.* **1979**, *44*, 24–33.

51. Plešek, J.; Heřmánek, S. Syntheses and properties of substituted icosahedral carborane thiols. *Collect. Czech. Chem. Commun.* **1981**, *46*, 687–692.

52. Bumm, L. A.; Arnold, J. J.; Charles, L. F.; Dunbar, T. D.; Allara, D. L.; Weiss, P. S. Directed self-assembly to create molecular terraces with molecularly sharp boundaries in organic monolayers. *J. Am Chem. Soc.* **1999**, *121*, 8017–8021.

53. Kohn, W.; Sham, L. J. Self-consistent equations including exchange and correlation effects. *Phys. Rev.* **1965**, *140*, A1133–A1138.

54. *ABINIT*; Université Catholique de Louvain, Corning Incorporated, Université de Liège, Commissariat à l'Energie Atomique, Mitsubishi Chemical Corp., Ecole Polytechnique Palaiseau, and other contributors.

55. Gonze, X.; Amadon, B.; Anglade, P.-M.; Beuken, J.-M.; Bottin, F.; Boulanger, P.; Bruneval, F.; Caliste, D.; Caracas, R.; Cote, M.; Deutsch, T.; Genovese, L.; Ghosez, P.; Giantomassi, M.; Goedecker, S.; Hamann, D. R.; Hermet, P.; Jollet, F.; Jomard, G.; Leroux, S.; Mancini, M.; Mazevet, S.; Oliveira, M. J. T.; Onida, G.; Pouillon, Y.; Rangel, T.; Rignanese, G.-M.; Sangalli, D.; Shaltaf, R.; Torrent, M.; Verstraete, M. J.; Zerah, G.; Zwanziger, J. W. ABINIT: First-principles approach to material and nanosystem properties. *Comput. Phys. Commun.* **2009**, *180*, 2582–2615.

56. Perdew, J. P.; Burke, K.; Ernzerhof, M. Generalized gradient approximation made simple. *Phys. Rev. Lett.* **1996**, *77*, 3865–3868.

57. Blöchl, P. E. Projector augmented-wave method. *Phys. Rev. B* **1994**, *50*, 17953–17978.

58. Holzwarth, N. A. W.; Matthews, G. E.; Dunning, R. B.; Tackett, A. R.; Zeng, Y. Comparison of the projector augmented-wave, pseudopotential, and linearized augmented-plane-wave formalisms for density-functional calculations of solids. *Phys. Rev. B* **1997**, *55*, 2005–2017.

59. PAW dataset for Abinit — ABINIT http://www.abinit.org/downloads/PAW2 (accessed Sep 7, 2012).

60. Monkhorst, H. J.; Pack, J. D. Special points for brillouin-zone integrations. *Phys. Rev. B* **1976**, *13*, 5188–5192.

CHAPTER 4

Defect-Tolerant Aligned Dipoles within Two-Dimensional Plastic Lattices

4.1 Introduction

Creating molecular systems with precise control over position, orientation, and interactions allows control over chemical reactions with practical applications in nanomaterials, bio-assembly and catalysis [1-7]. Electrostatic fields, collisional forces, and intense laser fields have demonstrated molecular dipole alignment [8-11]. Most alignment characterization methods are ensemble measurements, where local information is lost [12-14]. Using STM to resolve chemical state information at the molecular level has spurred the development of a variety of techniques that extend its capabilities beyond structure, such as photon-coupled, alternating current, and microwave-coupled STM [1, 15-21]. By employing multimodal STM, we can visualize molecular alignment of dipole-containing carboranethiolate within SAMs at 4 K. Local barrier height was measured as a function of position across the surface by modulating the tip-surface distance around its constant-current topographic imaging value, which is a convolution of both electronic and topographic information and allows for simultaneous measurements of local dipoles and the exposed interface in order to visualize molecular orientations within quasi-2D systems. Local barrier height (LBH) is mapped as the first harmonic (dI/dz) of the modulated current, which is a function of surface topography and local tunneling work function [22-25]. Previous studies such as the Mermin-Wagner theorem predict spontaneous symmetry breaking, which prohibits aligned dipoles in two dimensions, however alignment is allowed in longer range interactions, whereas we visualize ordering in quasi-2D monolayers [26, 27]. In this study we use a custom-built, ultrastable STM that can measure and visualize the molecular geometry and intermolecular interactions [28]

Self-assembly provides a simple way for construction of well-defined monomolecular films, which can be used in various applications ranging from nanotechnology all the way to the life sciences [29-34]. The most commonly used *n*-alkanethiols produce monolayers on Au{111} that tilt and have degrees of freedom (e.g., conformation relaxation, gauche defects) that lead to defects, whereas carboranethiols are rigid three-dimensional carboboron- hydrogen compounds that adsorb upright and form ordered monolayers on Au{111} [35, 36]. Carboranethiol monolayers on Au{111} form identical lattices independent of isomers, which provides a simple system in which we can test the effects of intermolecular interactions, while keeping the monolayer structure the same [37,38]. Previous studies have shown that carboranetiols that have dipole moments parallel to the surface outcompete carboranethiols with dipoles normal to the surface [38]. Motivated by this key feature and previous studies conducted, we set out to observe the intermolecular dipole interactions responsible for this effect. The STM can be used to measure both topography and spatial dipole offset with submolecular resolution as we compare the monolayers of *o*-9-carboranethiolate (**O9**) and *m*-1-carboroanethiolate (**M1**); the largest contributor to the dipole is from the electron-deficient carbon atoms in the *ortho* and *meta* positions of the boron cage. Correlating the topographic maxima with tunneling barrier height maxima allows the measurement of the dipole offset within different regions, molecular domains, substrate terraces and molecules within each SAM.

Previous studies have shown that monolayers of carboranethiols and various other symmetric cage molecules have lattices determined by projections of the cage on the substrate surface [35, 37, 39, 40]. Therefore, **O9** and **M1** carbanethiols have identical lattices. The most common defects in these monolayers are substrate step edges and molecular domain boundaries [35, 37, 39, 41, 42].

4.2 Results and Discussion

Topographic and LBH modalities are measured simultaneously while imaging domains in **O9** monolayers and comparing local orientations across monatomic substrate steps (Figure 4.1). Local maxima in both modalities are computed within a square pixel window with an approximate nearest neighbor lattice constant (~7.2 Å). Tunneling LBH, $\varphi = 0.95(dl(I)/dz)^2$, which can be related to the local dipole using electrostatics, $\Delta\varphi = \Delta\mu e/\varepsilon_0 A$, permittivity of a vacuum is ε_0 and A is area, which associates the LBH maxima to the largest surface dipole normal to the substrate and the topographic maxima to the topographic molecular apexes [43-45]. The **O9** molecule was designed to contain a large dipole (5.72 Debye) that is tilted off normal with respect to the substrate surface and dipole and we assign LBH as the dipole apexes due to *o*-carbone atoms. Overlaying image maximas allows the LBH and topographic maxima offsets to be evaluated using a block-matching algorithm. Block-mathcing computes the correlations between sliding image patches in both bounded modalities within a molecular-sized search window [46,47]. Rose plots are used to depict dipole offsets from topographic molecular apexes, which are binned in degrees and magnitude, for multiple domains using image thresholding and masking techniques (Figure 4.2). Dipole orientation analysis across separate domains reveals orientations of $308 \pm 27°$ above and $341 \pm 31°$ below the substrate step edge, with respect to the image axis of LBH and topography. Measurement of different orientations the same image is consistent with dipole orientation and not imaging artifacts (Figure 4.3). Measurements of **O9** molecular regions reveal a measureable amount of ordering at 4 K with minimal single-molecule dipole orientation defects.

In contrast to the **O9** orientation measurements, we study **M1** which has the same molecular lattice as **O9** [37]. The dipole moment for **M1** (1.08 Debye) is smaller in magnitude with the largest component oriented parallel to the substrate. The LBH maxima measured corresponds to the electron-deficient carbon atoms at 9- and 12- positions within the **O9** monolayer and the 1- and 7- carbon atoms within the **M1** monolayer. Identical analyses for local regions of **M1** SAMs are performed, which involve overlaying image maximas, correlations computation, and orientation mapping on flat gold terraces (Figure 4.4). As seen in figure 4.4, three different regions are highlighted, two being lattice matched with different orientations and a third area depicting local disorder, which is confirmed by Fourier analysis (Figure 4.5). In these highlighted areas dipoles are oriented 290 ± 31° with respect to the image axis and displayed in a Rose plot. It should be noted that defect-tolerant alignment crosses both substrate step edges and different molecular domains within the same terrace for both carboranethiol monolayers.

Correlations are computed using sliding patches in each image for each maximum p in the topographic images and each maximum q in the LBH images. We then acquire a set of vectors, *pq*, associated with each dipole (Figure 4.6). The **O9** monolayers show the largest spatial (x-y) distribution at 2.0 ± 0.3 Å. The correlation between local maxima between LBH and topographic images of **M1** SAMs reveal a local two-dimensional offset of 2.4 ± 0.5 Å (Figure 4.7) and confirm past results obtained using infrared spectroscopy [37]. Analyzing numerous samples and images ($n_{molecules} > 1000$), we see that **O9** displays an average offset of 1.8 ± 0.8 Å, while **M1** shows a slightly higher average offset of 2.0 ± 0.8 Å. Recent studies have shown long range dipolar interactions of carboranethiol isomers across aqueous media, where parallel alignment was larger than perpendicular alignment with respect to surface normal, due to in-

plane surface dipoles [48]. In this study we employ density functional theory to calculate a point dipole which is used to predict alignment.

Utilizing a simple model, we can determine and understand the dipole-dipole interaction energies within a SAM as shown in Figure 4.7. Intermolecular dipole interaction energies are determine by the potential energy of the dipole moment in the local electric field. The electric field's in-plane component from the tip is irrelevant in the tunneling junction, thus justifying excluding tip-induced electric field effects from our calculations, which has been confirmed experimentally, as shown in Figure 4.8; molecular orientations remain fixed in space, independent of scan direction, and are stable over days of imaging at low temperature. In our model, the surrounding molecules, which are assumed to be ideal electric dipoles arranged in a hexagonal lattice, determine the strength and direction of the field and alignment with the field acts to stabilize the dipole orientations. Using this model, we estimate the molecules' interaction energies, and any changes in those energies, with respect to the surrounding SAM lattice. Changes in the intermolecular interaction energy can be caused by dipole reorientation. A Monte Carlo method using the metropolis algorithm is used to determine possible stable orientation of molecular dipoles in a SAM [49]. Low temperatures cause the system to evolve towards a state where dipoles align in a common direction and the energy stabilizes their orientation, which allows for the formation and growth of ordered regions of molecular dipoles (Figure 4.9). These simulated results are consistent with the topographic and LBH data obtained with STM and explains the mechanism which drives the ordering of dipoles.

The STM is capable of imaging molecular monolayers and the underlying substrate-molecule bonds, which makes absolute tilt assignments possible [50]. For the first time, measurements herein use LBH imaging with dipole containing molecules to resolve local

orientation within the SAMs chemical environment. Topographic and LBH images, which are 256×256 pixels, are corrected for image anomalies on a line-by-line basis using a matrix transformation approach due to residual drift and non-orthogonalities of the scanner tube during high-resolution data acquisition (~2 hr) (Figure 4.10 and 4.11). Additionally, distortions such as shear are accounted for in Fourier space and the adjusted images are used in further analyses. Local maxima are overlaid (Figure 4.12 and 4.13) and each topographic maximum is connected to all LBH maxima within a square pixel window of varying size. These results are then compared to the computed correlations for both molecular monolayers. In the **O9** and **M1** images depicted, block matching yields the maximum computed correlation in a varied square pixel window for all maxima where increased artifacts act as a function of pixel window size. Entropy gray scale values, calculated in MATLAB (Figure 4.14 and 4.15) are measured in a 9×9 pixel neighborhood, and are compared within local regions in **O9** and **M1** monolayers. Centered at each pixel, mean entropy values in both topographic and LBH image masks contain a large number of accessible grayscale states, demonstrating high image textural contrast [51]. Previous work has shown that nearby continuous modulation of the metal work function (~1 eV) can be achieved by controlling mixtures of carboranethiol isomers, which are extremely robust in the presence of active organic layers in fabricated devices [52]. These techniques can be used to determine domains and domain sizes of carboranethiolates as well as dipole orientations within and between domains [53-55]. The average LBH values with respect to single crystal Au have been measured: (**M1:** +0.20+- 0.18 eV, **O9**: -0.97 +- 0.21 eV). Coupling data acquisition with new image analysis techniques will enable for greater insight of local snapshots between bounded dipole interfacial and topographically exposed modalities.

4.3 Conclusions and Prospects

Employing multi-modal imaging allows the measurement of single-molecule orientations when correlating topographic and LBH images. Carboranethiols, specifically **M1** and **O9** which contain large molecular dipoles, form into ordered arrays and contain fewer types and number of defects in comparison to linear/tilted chain molecules [25,27,56-59]. Using STM, we can simultaneously probe the 2D interface in topographic mode and the buried dipole interface in LBH mode.

Greater tunability of assemblies is possible when creating monolayer systems with defect tolerance and precisely determined dipoles, enabling enhanced control of stability through designed interactions. Various single-molecule measurement methods have major disadvantages, unlike STM which can measure the local environment with submolecular resolution and the capability to use spectroscopic imaging for chemical identification [17, 60-64]. Creating chemical environments with cage molecules will be an important milestone in creating detailed structures in two and three dimensions.

4.4 Materials and Methods

4.4.1 SAM Preparation

Benzene and **M1** were used as received (Sigma-Aldrich, St. Louis, MO). The chemical **O9** was prepared and characterized based off previous literature [42]. The Au{111} substrates (Agilent, Santa Clara, CA) were hydrogen flame annealed and solution deposited into a 1mM benzoic solution held at room temperature for ~10 minutes. Short deposition times were used in order to maximize the local defects while retaining a well-ordered monolayer. Each sample was removed from solution and rinsed with neat benzene and dried with a stream of ultrahigh purity argon. The sample was then introduced into the UHV chamber.

4.4.2 Imaging

All STM measurements were conducted with a custom-built Besoke-style STM under extreme high vacuum ($<10^{-12}$ torr) and cryogenic (4 K) conditions [65]. Simultaneous constant-current topographic and LBH images were acquired at a fixed sample bias of (V_{sample} = -0.5 V) and tunneling current of (I_T = 15 pA). All LBH images were acquired by a small AC modulation of the tunneling-gap distance, with a sinusoidal voltage amplitude of ~ 0.1 Å and a frequency of ~3 kHz. The derivative of the modulated current, dI/dz, was measured using a lock-in amplifier (Stanford Research Systems SR850 DSP, Sunnyvale, CA). Images were calibrated using the lattice of atomic Au{111}, held at 4 K. Local barrier height images were further calibrated alongside Au step edge measurements in order to validate the method used (Figure 4.16).

4.4.3 Image Analyses

An automated digital processing routine developed in MATLAB (Mathworks, Natick, MA) was applied to all STM images. This routine removes high-frequency noise and intensity spikes that may hinder reliable maxima selection [25]. Images were skew corrected and verified in Fourier space in order to remove any image anomalies caused by drift and piezoelectric transducer non-linearities. Points p and q are denoted as local maxima in topographic and LBH images, respectively. Point p was considered a local maximum if its intensity was larger than every other pixel's intensity surrounding its molecular-sized neighborhood. The molecular-sized neighborhood is defined as a square centered at p, the size $[2p + 1] \times [2p + 1]$; similarly, we compute each point q in the LBH image. After points p and q were obtained, an image patch centered at each p, the size $[2p + 1] \times [2p + 1]$, was correlated at each pixel against a larger LBH image patch, centered at q, of the size $[2qs + 1]\times[2qs + 1]$. Parameter qs is defined as the size of the next-nearest neighbor spacing. This technique is called block-matching, which has been used

in the fields of image compression and object recognition [46, 47, 66, 67]. Maximum correlations for each point p to q were chosen and then referenced and plotted.

4.4.4 Dipole–Dipole Interaction Energy

Each carboranethiol molecule was modeled as an ideal electric dipole moment originating at the center of the cage moiety in a hexagonally close-packed array. A molecule's dipole interaction energy is estimated to be the electric potential energy (U) of the molecule's dipole moment ($\vec{p}$) in the local electric field ($\vec{E}$),

$$U = -\vec{p} \cdot \vec{E} \qquad \text{(Equation 4.1)}$$

The electric field is the vector sum of the fields produced by the surrounding dipoles,

$$\vec{E} = \sum_i \frac{1}{4\pi\epsilon_0} \frac{3(\vec{p}_i \cdot \hat{r})\hat{r} - \vec{p}_i}{r^3} \qquad \text{(Equation 4.2)}$$

where r is the separation distance between the molecule under consideration and its ith neighboring dipole moment ($\vec{p}_i$). The gold substrate influences the electric field due to the induced charge on the conductor, producing an image dipole beneath the surface for each dipole in the SAM. Dipole interaction strength diminishes as r^{-3}, rendering more distant dipole moments less significant contributors to the calculated energy. The summation in Equation 4.2 includes just neighboring molecular dipoles, and image dipoles within the first four concentric, hexagonal rings surrounding the molecule under consideration. We assumed left-right and top-bottom periodicity in our modeled SAM, so that the opposite edges of the rectangular molecular lattice coincided with each other, hence simulating an infinite monolayer.

4.4.5 Monte Carlo Simulations

We employed the Metropolis algorithm to determine possible equilibrium orientations of molecular dipole moments within a SAM. Iteratively, the interaction energy of a randomly chosen molecule within a SAM was computed before and after a proposed reorientation. Each

reorientation rotated the molecule by a random angle about an axis normal to the substrate, thereby only altering the lateral position and in-plane components of the dipole moment. Depending on the change in energy, the reorientation was either accepted and preserved in subsequent iterations, or discarded without changing the state of the system. The probability of preserving the change is:

$$Probability\ (\%) = \ 100\ \times \begin{cases} 1, \Delta E < 0 \\ e^{-\Delta E/k_B T}, \Delta E \geq 0 \end{cases},$$

where ΔE is the change in the dipole interaction energy due to the reorientation, k_B is the Boltzmann constant, and T is the absolute temperature of the system.

We created a model SAM with no net in-plane polarization (randomized molecular orientations) and allowed it to progress through successive iterations. The simulations predict that, at the low temperatures (4 K), both **O9** and **M1** SAMs progress toward states with regions of locally aligned in-plane molecular dipoles, as depicted in the STM data. At room temperature (~293 K), we did not observe spontaneous dipole ordering, however we notice the loss of order in a pre-aligned SAM due to random thermal reorientations.

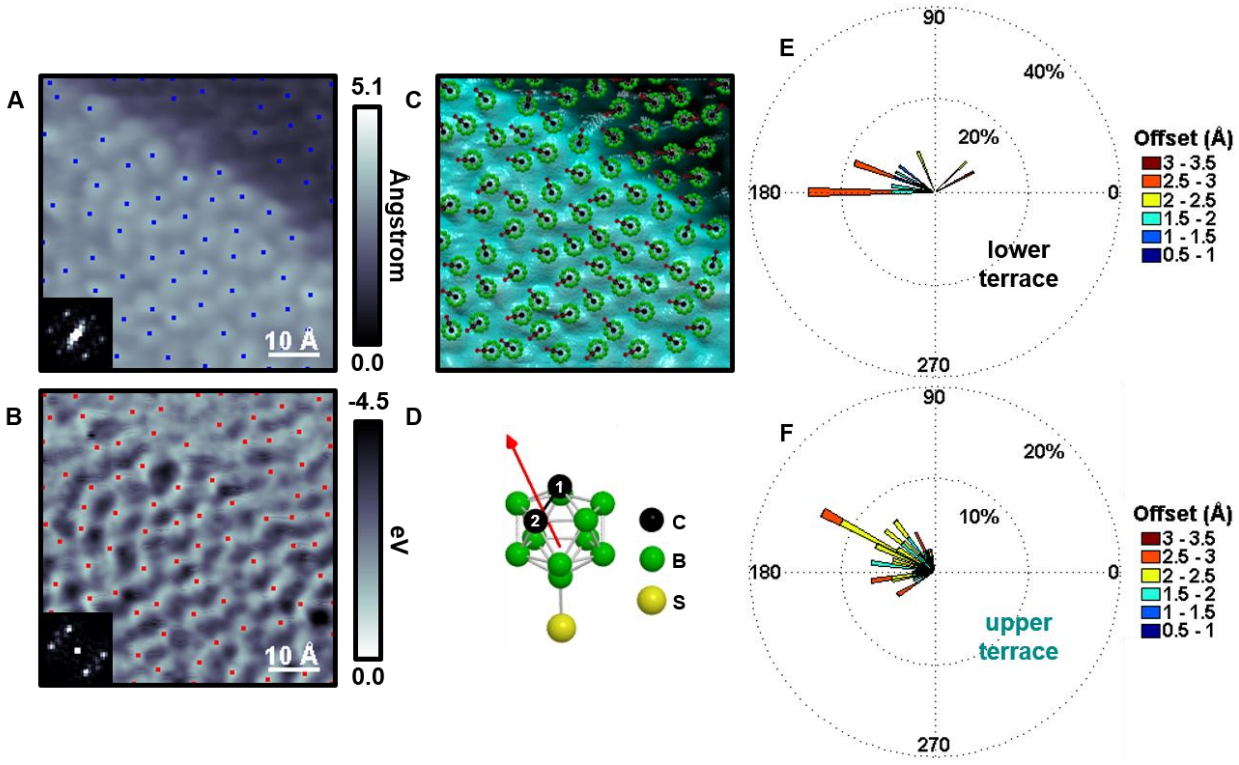

Figure 4.1: **(A)** Scanning tunneling micrograph obtained at V_S = -0.5 V and I_T = 15 pA of **O9** on Au{111} along a monatomic substrate step edge with local maxima depicted in blue. Inset shows a fast Fourier transform (FFT), which reveals a hexagonally close-packed lattice with a 7.2 ± 0.4 Å lattice constant. **(B)** Inverted local barrier height (LBH) image showing carbon positions with the computed local maxima shown in red. Inset shows a FFT revealing the order seen topographically. **(C)** Local dipole vector map displaying the overlaid topographic maxima corresponding to the LBH maxima made visible with a spherical model overlaid by topography. Non-correlated molecules are displayed in gray. **(D)** Molecular schematic of **O9** with hydrogen atoms omitted for clarity. The calculated dipole magnitude is 5.72 D, as shown by the red arrow. In **(E)** and **(F)** Rose plots show the lower terrace (below step edge) and upper terrace (above step edge) that are binned in both magnitude (0.5 Å bins) and direction (4° bins).

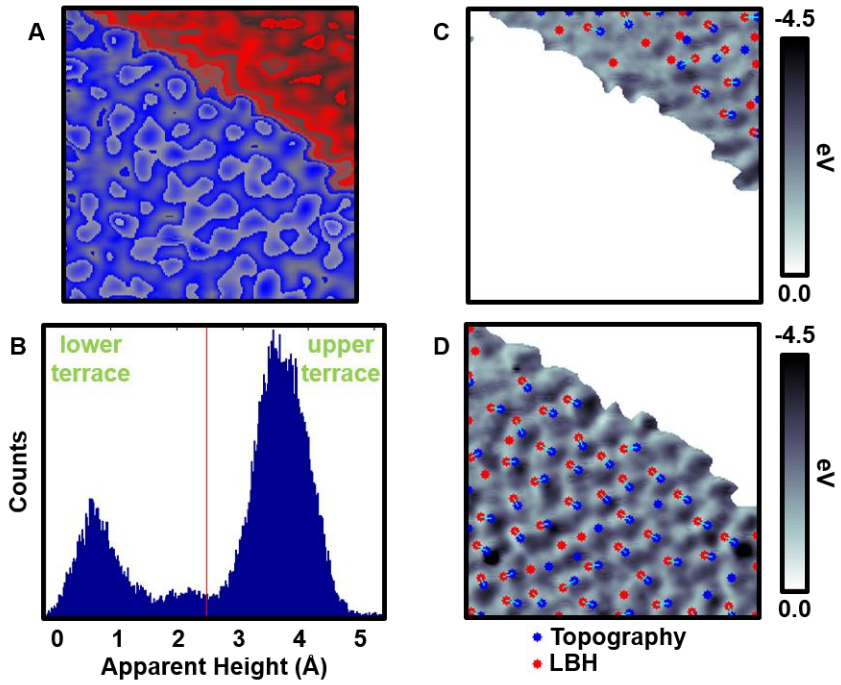

Figure 4.2: **(A)** We divide the topographic image along a monatomic Au{111} step edge and **(B)** show the resulting image histogram. We separate topography based on thresholding (red line) and create a mask that is used to segment LBH images. In **(C)** the topographic and LBH maxima are overlaid for the lower terrace, and correlations are computed. In **(D)** the topographic and LBH maxima are overlaid for the upper terrace, and correlations are computed. Dipole offsets shown in **(C)** and **(D)** were used for the Rose plots in Figure 4.1.

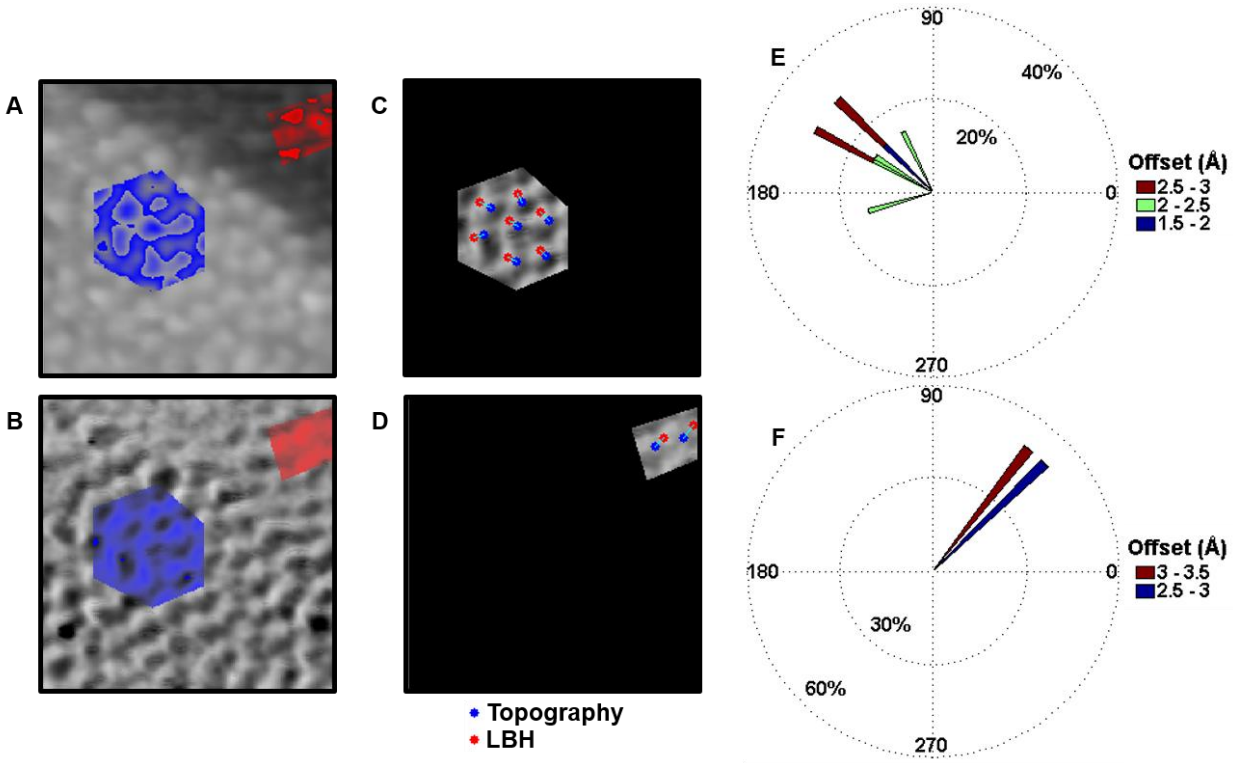

Figure 4.3: **(A)** Topography and **(B)** LBH images depict two regions highlighted by inspection, where each region displays local variation in dipole offsets and directions within the same terrace. Masks are created and used to highlight both areas. **(C)** Topographic and **(E)** LBH maxima are overlaid and correlations are computed. Rose plots for each case, **(D)** and **(F)** show local directionality that is binned in direction (4° bins) and magnitude (0.5 Å bins) with respect to the image axis in **(C)** and **(E)**, respectively.

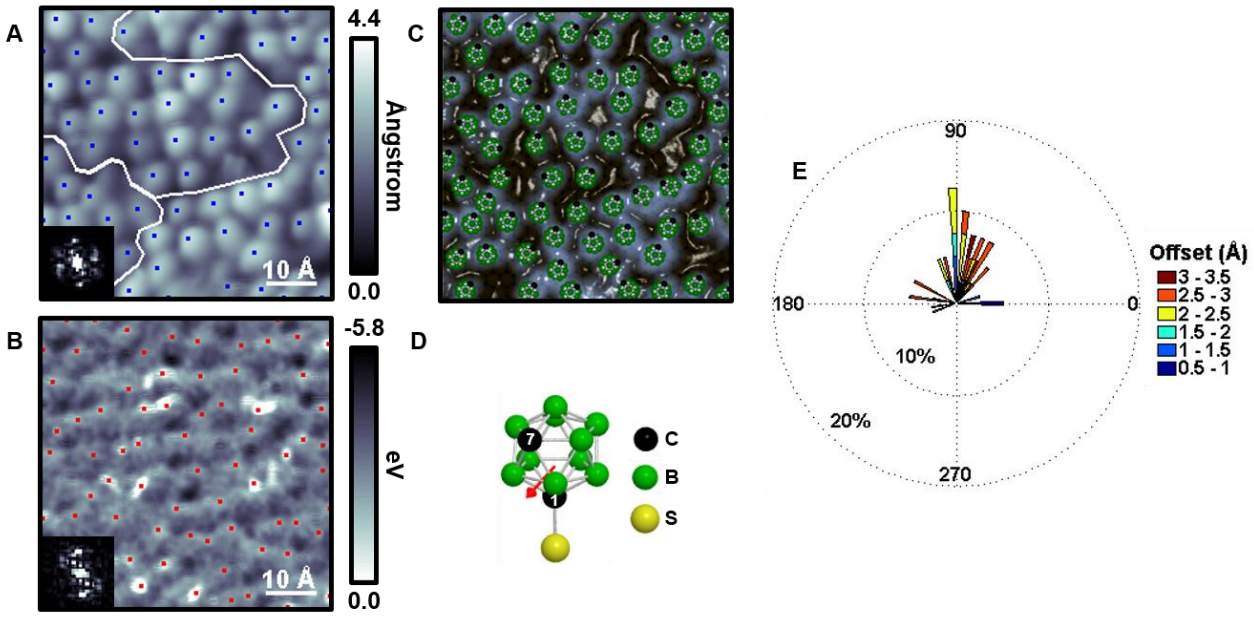

Figure 4.4: **(A)** Scanning tunneling micrograph obtained at V_S = -0.5 V and I_T = 15 pA of **M1** on Au{111} on the same substrate terrace with three different regions separated by lines (see Figure 4.8 for further explanation). Inset shows the FFT, which reveals a hexagonally close-packed lattice with a 7.2 Å lattice constant. Local maxima of both **(A)** topographic and **(B)** inverted local barrier height are solved for in a radial fashion (r = 3 Å). **(C)** A schematic displaying local molecular position overlaid with topography. **(D)** Molecular schematic of **M1** with hydrogen atoms omitted for clarity. The calculated dipole magnitude is 1.08 D, as shown by the red arrow oriented in the plane of the gold substrate. **(E)** Rose plot of the measured dipole vector orientation binned in both magnitude (0.5 Å bins) and direction (4° bins). Figure 4.16 shows correlation results used in **(E)**.

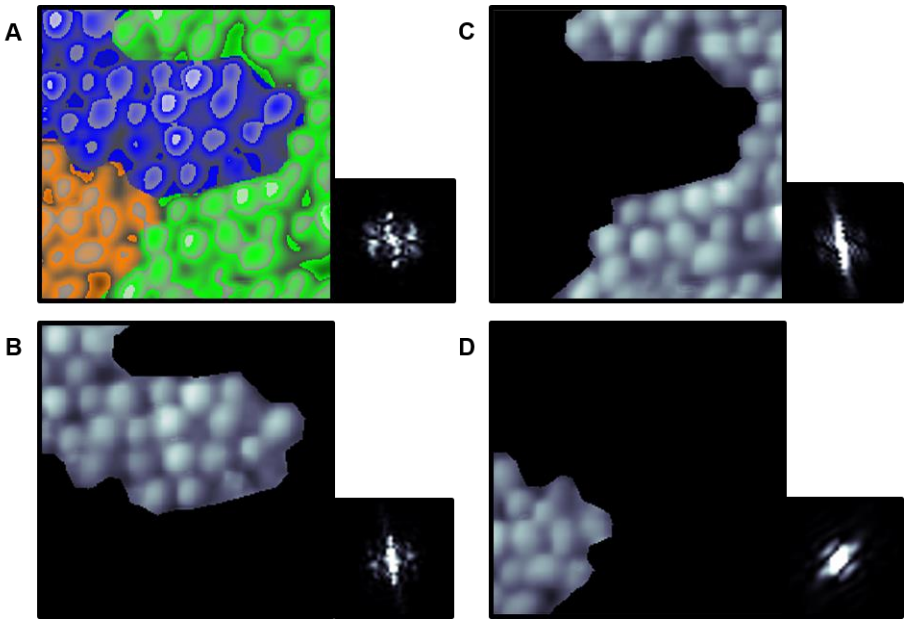

Figure 4.5: **(A)** The image shown in Figure 4.2 is segmented by inspection in order to create a mask used to separate the image into regions **(B)**, **(C)**, and **(D)**. Each image is then analyzed in Fourier space, where **(B)** is an area of local disorder and **(C)** and **(D)** are lattice matched with a different orientations.

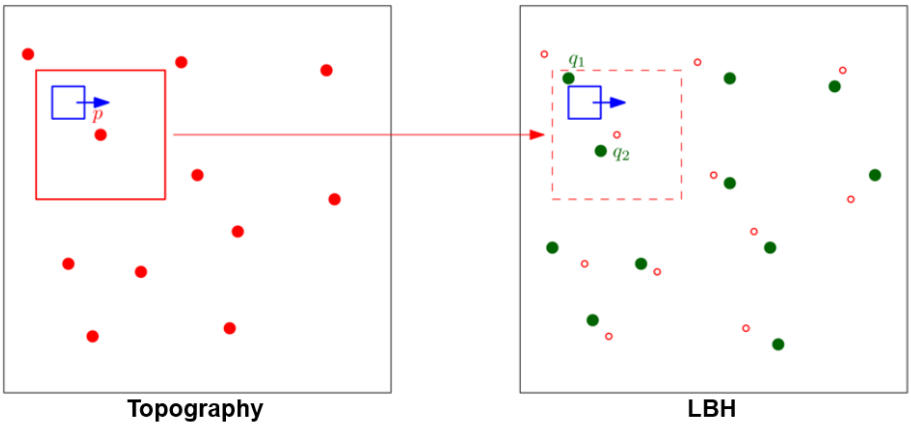

Figure 4.6: If we assume two corresponding sets of local maxima per data set (red circles in the topography image and green circles in the LBH image), we can then pick a maximum *p* from the topography image, and search for its corresponding LBH maximum. We then use a block-matching approach to find such correspondences between the two. Since topography and LBH images are acquired simultaneously, both images are bounded, and we can define a search window (the red square in the topography image and doted red square in the LBH image) that is centered at *p* of a given dimension (size of one molecule). Correalations are computed between sliding patches taken at the same position in each image in the search window (the blue squares) and decide which LBH maximum (i.e., $q1$ and $q2$) corresponds to *p* and calculate the maximum correlation. This procedure is then performed for each maximum *p* in the topographic image and a set of vectors are computed which are associated with each molecule. The set of vectors relate the molecular maxima to the dipole positions.

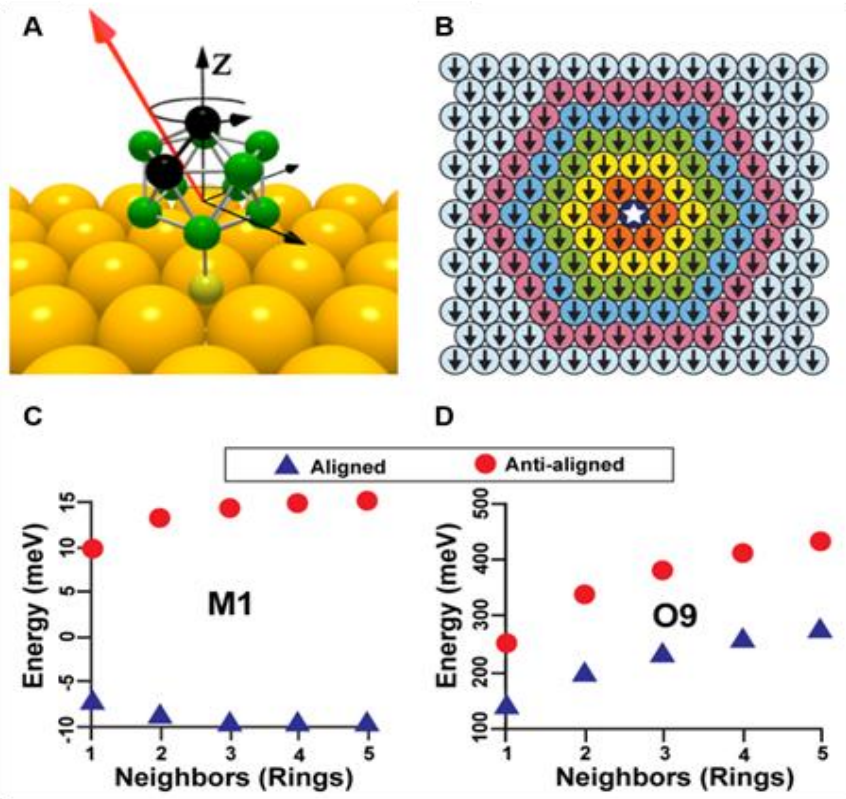

Figure 4.7: Dipole interaction energy: in order to estimate the dipole interaction energy, we assume a carboranethiol molecule standing normal to a gold surface, along the z-axis, as shown in the structural schematic **(A)** of an **O9** molecule. Iterations of the Metropolis algorithm affect random rotations about the z-axis, changing the dipole (red arrow) orientation and interaction energy. **(B)** Representation of a carboranethiol SAM, with inscribed arrows indicating the in-plane orientation of each molecular dipole. Every dipole in the molecular lattice, except for the central molecule, aligns along the same direction. The plots depicted in **(C) M1** and **(D) O9** show the interaction energies of a dipole aligned in the same (aligned-blue triangles) and opposite (anti-aligned-red circles) direction in relation to its neighbors. The interaction energy depends on the number of concentric, hexagonal rings of neighboring molecules included in the summation in Equation 4.2. In **(B)**, we highlight the first five rings around a central molecule (indicated by an inscribed star) with the colors orange, yellow, green, blue, and pink. Other molecules outside these rings do not contribute to the interaction energy.

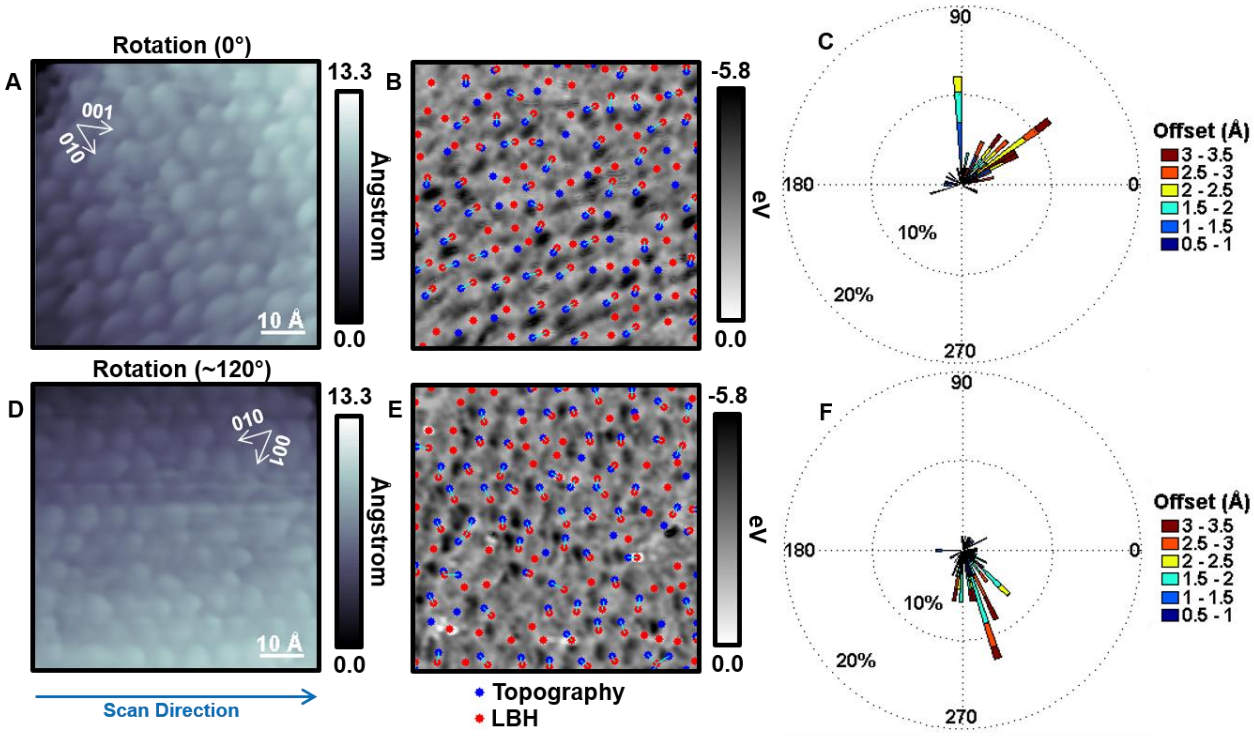

Figure 4.8: We test if the tip electric field plays a role during data acquisition. Images were obtained at V_S = -0.5 V and I_T = 15 pA for **(A)** topography and **(B)** LBH near a step edge, where topographic and LBH maxima are overlaid and correlations are computed. **(C)** The Rose plot shows the local dipole offset of **(B)** that is binned in direction (4˚ bins) and magnitude (0.5 Å bins) with respect to the image axis in **(A)**. Scan angle is rotated and both **(D)** topography and **(E)** LBH are measured, where correlation are computed again to obtain the Rose plot shown in **(F)**. The dipole offset rotates with scan angle rotation, and opposes the fast scan direction in **(E)**.

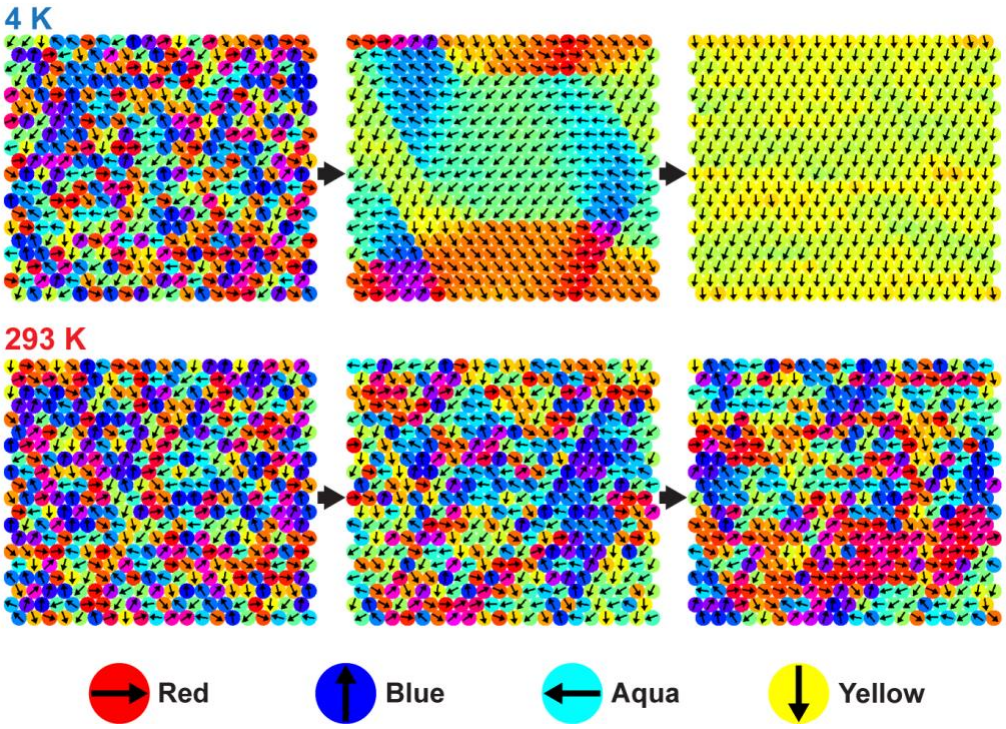

Figure 4.9: Simulated monolayers evolving under the influence of internal dipole fields. We track the orientation of molecular dipoles in a 20×20 molecule region for an **O9** SAM. At 4 K (top), the molecular dipoles progress towards a state where they align along a common direction. However, we do not observe this trend in simulations at 293 K (bottom); the dipoles remain randomly oriented and no permanent polarization develops. Over the course of 500,000 iterations of a Monte Carlo algorithm, monolayer progression from left to right, initial, intermediate, and final states are depicted. Individual **O9** molecules are represented as circles inscribed with an arrow indicating the orientation of the molecule's in-plane dipole moment. Dipole orientation also determines the depicted color of each molecule (bottom). Molecules with dipoles oriented toward the top appear blue, oriented to the right appear red, oriented to the left appear aqua, and oriented towards the bottom appear yellow. Intermediate orientations result in a combination of these colors. Similarly **M1** monolayers progress in a similar way to those of **O9**.

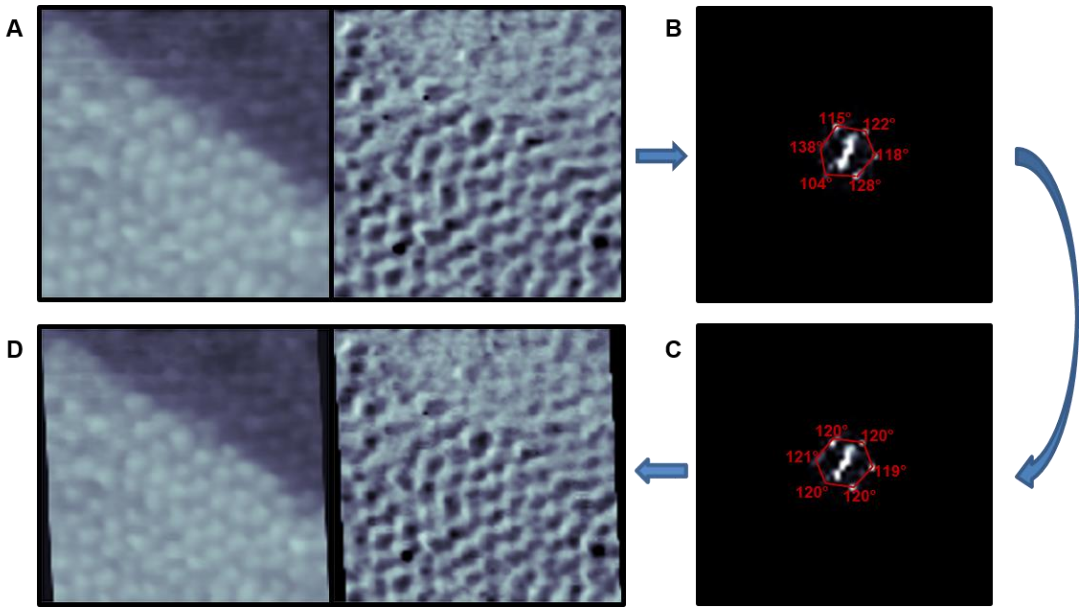

Figure 4.10: **(A)** Topography (left) and LBH (right) images of **O9** SAMs are shown before image aberration correction. **(B)** Images are then transformed into the Fourier domain, and the reciprocal lattice points are symmetrized **(C)** using the following transform matrix, $\begin{pmatrix} 1 & c_1 & 0 \\ c_2 & 1 & 0 \\ 0 & 0 & 1 \end{pmatrix}$, where c_1 and c_2 are the correction factors in both the y and x planes, respectively. **(D)** Corrected images are depicted after optimization.

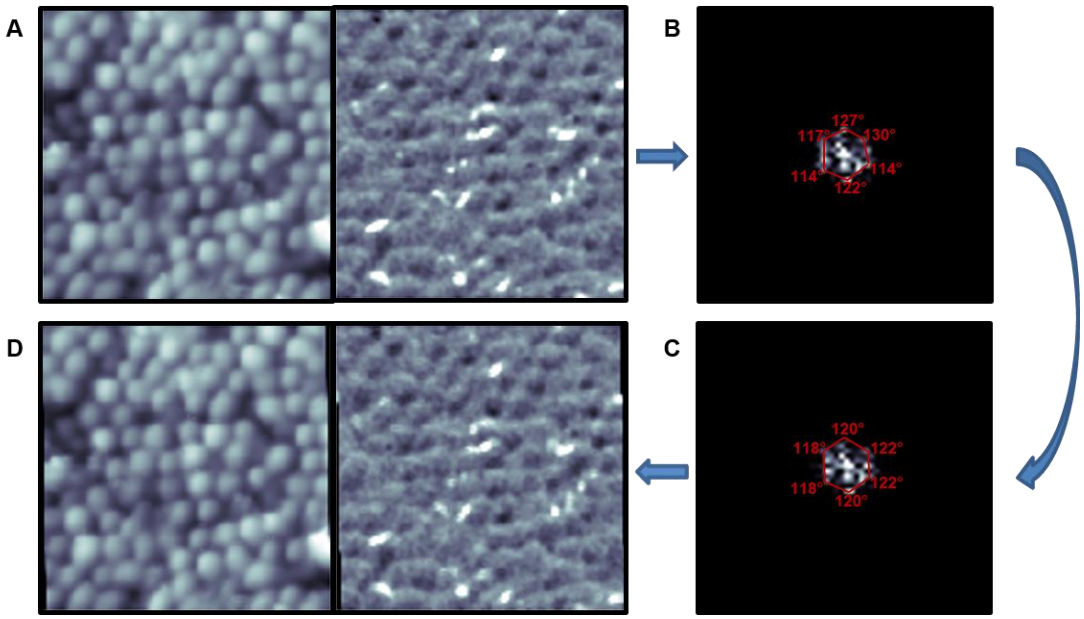

Figure 4.11: **(A)** Topography (left) and LBH (right) images of **M1** SAMs are shown before image aberration correction. **(B)** Images are then transformed into the Fourier domain, and the reciprocal lattice points are symmetrized **(C)** using the transform matrix shown in Figure 4.10. **(D)** Corrected images are depicted after optimization.

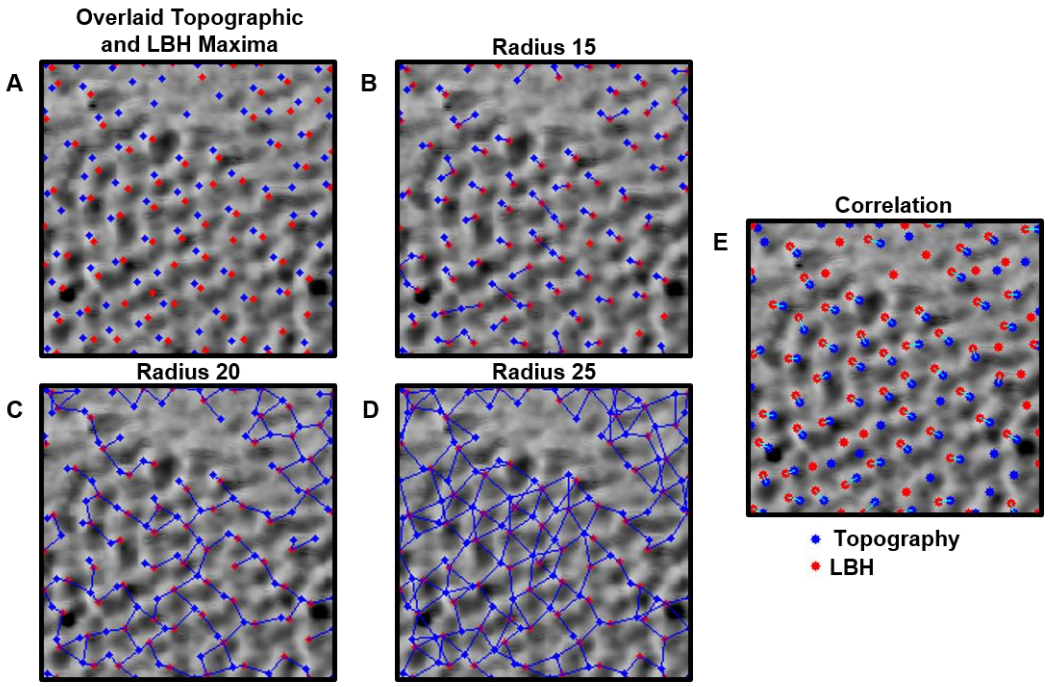

Figure 4.12: **(A)** Topographic and LBH maxima are overlaid on **O9** LBH images for comparison. Maxima are compared by drawing all vectors, *pq*, within a specified square pixel window **(B)**, [15 **(C)** 20, and **(D)** 25 pixels]. Differences seen above and below 15-25 pixels are trivial, and all ranges depict artifacts. **(E)** Within a specified square pixel window, *p*, window centered around each topographic maximum $[2p + 1] \times [2p + 1]$ is then correlated with the equal-size pixel, *q*, window in the LBH image $[2q + 1] \times [2q + 1]$. The result shown reveals maximum correlated topographic and LBH maxima drawn with a vector, *pq*, which is then stored and plotted for each molecule.

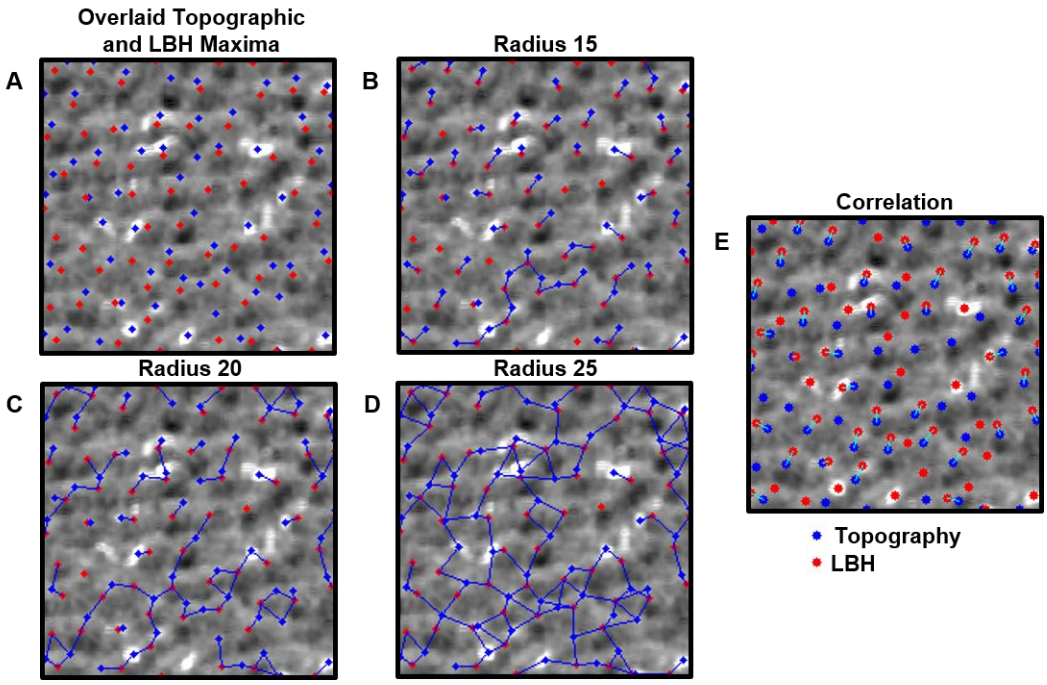

Figure 4.13: **(A)** Local barrier height and topographic maxima are overlaid for **M1** monolayers for comparison. Maxima are compared by drawing all vectors, *pq*, within a specified square pixel window [15 **(B)**, 20 **(C)**, and 25 **(D)** pixels]. Differences seen above and below 15-25 pixels are trivial. Each increase in window size from 15 pixels to 25 pixels shows increased artifacts. **(E)** Cross-correlation, within a specified square pixel window, *p*, window centered around each topographic maximum $[2p + 1] \times [2p + 1]$ is then correlated with an equal-size pixel, *q*, window in the LBH image $[2q + 1] \times [2q + 1]$. The result shown reveals maximum correlated topographic and LBH maxima drawn with a vector, *pq*, which is then stored and plotted for each molecule.

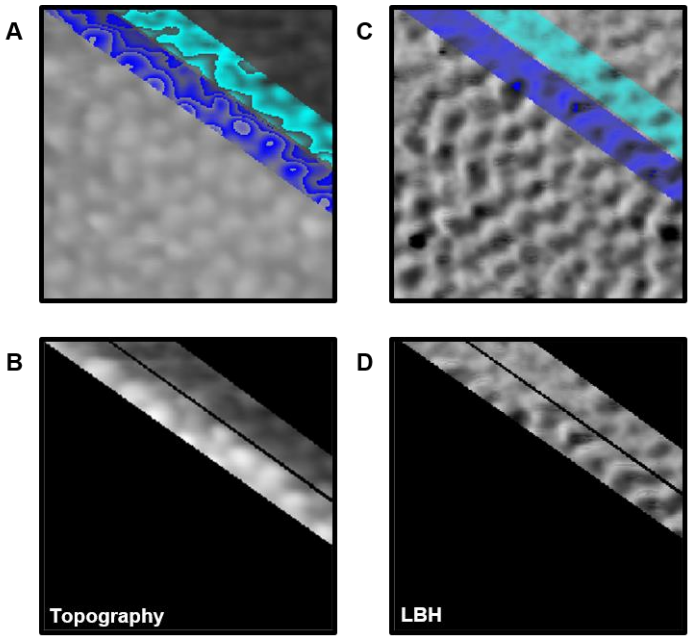

E

Image Mask	Pixel Entropy
Topography (Above Step Edge)	3.75 ± 1.78
Topography (Below Step Edge)	3.74 ± 1.74
LBH (Above Step Edge)	3.97 ± 1.89
LBH (Below Step Edge)	3.87 ± 1.84

$$E = -\sum_i p_i * \log_2 p_i$$

Figure 4.14: Textural differences above and below the step edge of **O9** were quantified using MATLAB matrix analysis software. Two regions around a step edge domain were selected in **(A)** and **(C)** and isolated in **(B)** and **(D)**. Each pair of regions were analyzed using entropy filtering which quantifies the number of accessible grayscale states in the intensity values of pixels in a 9x9 pixel neighborhood, where the entropy at the center point is calculated as seen in **(E)**. In LBH and topographic modes, regions around the step edge exhibit high textural contrast.

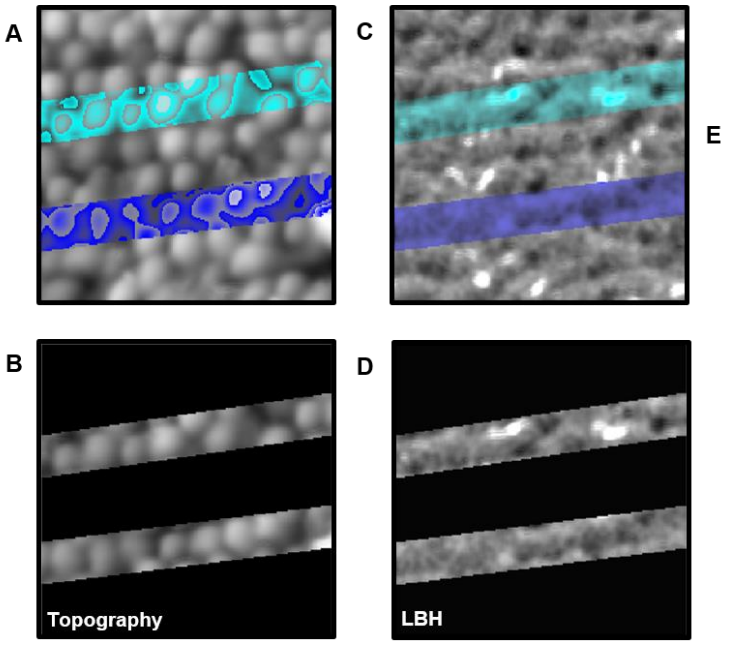

E

Image Mask	Pixel Entropy
Topography (1)	4.14 ± 1.51
Topography (2)	4.23 ± 1.58
LBH (1)	3.84 ± 1.35
LBH (2)	3.99 ± 1.46

Figure 4.15: Textural differences within the same domain of **M1** monolayers were quantified using MATLAB matrix analysis software. Two regions were specified in the topography and LBH images **(A)** and **(C)**, which isolated **(B)** and **(D)** by creating masks for the original image. Both sets of regions were analyzed in MATLAB where the entropy at the center point is calculated as seen in **(E)**. In LBH and topographic modes, regions of the same domain exhibit high textural contrast.

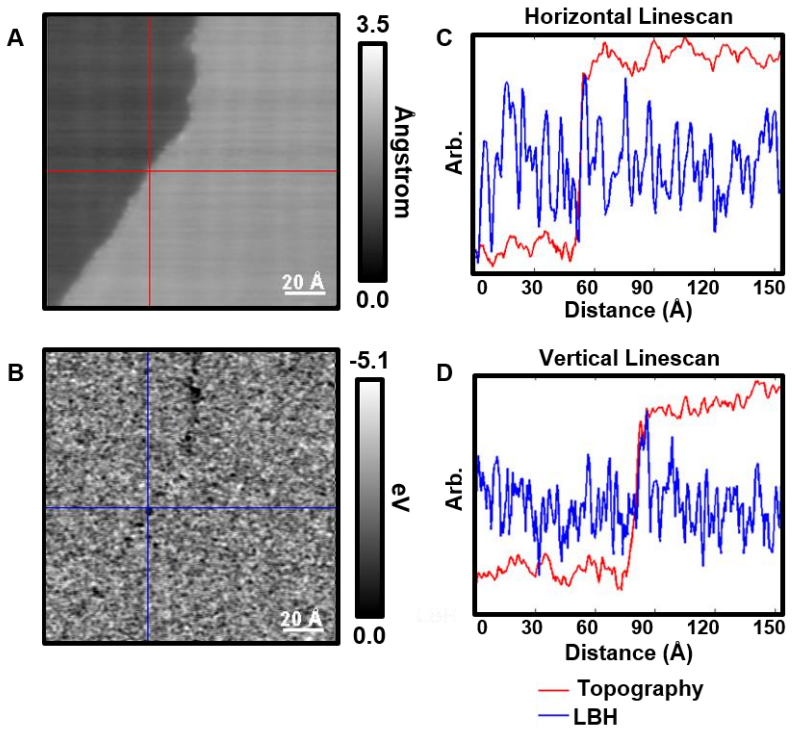

Figure 4.16: Calibration images were obtained at V_S = -0.5 V and I_T = 15 pA, using the same lock-in parameters in all local barrier height measurements (LBH), along a single-crystal Au{111} step edge simultaneously for both **(A)** topography and **(B)** LBH. Inset lines in both topography and LBH represent line scans shown in **(C)** and **(D)**, where the step edge corresponds to a peak in LBH, shown in both the X and Y direction, and thus verifying lock-in parameters.

4.5 References

1. Kim, M.; Hohman, J. N.; Cao, Y.; Houk, K. N.; Ma, H.; Jen, A. K.; Weiss, P. S. Creating favorable geometries for directing organic photoreactions in alkanethiolate monolayers. *Science* **2011**, *331*, 1312-1315.

2. Jorgensen, W. L.; Swenson, C. J. Optimized intermolecular potential functions for amides and peptides. Structure and properties of liquid amides. *J. Am. Chem. Soc.* **1985**, *107*, 569-578.

3. Friedrich, B.; Herschbach, D. Alignment and trapping of molecules in intense laser fields. *Phys. Rev. Lett.* **1995**, *74*, 4623-4626.

4. Zhang, Y.; Chang, A.; Cao, J.; Wang, Q.; Kim, W.; Li, Y.; Morris, N.; Yenilmez, E.; Kong, J.; Dai, H. Electric-field-directed growth of aligned single-walled carbon nanotubes. *App. Phys. Lett.* **2001**, *79*, 3155-3157.

5. Stapelfeldt, H. Colloquium: aligning molecules with strong laser pulses. *Rev. Mod. Phys.* **2003**, *75*, 543-557.

6. Mandal, S. K.; Okawa, Y.; Hasegawa, T.; Aono, M. Rate-determining factors in the chain polymerization of molecules initiated by local single-molecule excitation. *ACS Nano*, **2011**, *5*, 2779-2786.

7. Okawa, Y.; Aono, M. Materials sciene: nanoscale control of polymerization. *Nature*, **2011**, *409*, 683-684.

8. Estler, R. C.; Zare, R. N. Laser-induced chemiluminescence: variation of reaction rates with reagent approach geometry. *J. Am. Chem. Soc.* **1978**, *100*, 1323-1324.

9. Loesch, H. J.; Remscheid, A. Brute force in molecular reaction dynamics: a novel Technique for measuring steric effects. *J. Chem. Phys.* **1990**, *93*, 4779-4790.

10. Baugh, D. A.; Young Kim, D.; Cho, V. A.; Pipes, L. C.; Petteway, J. C.; Fuglesang, C. D. Production of a pure, single ro-vibrational quantum-state molecular beam. *Chem. Phys. Lett.* **1994**, *219*, 207-213.

11. Pirani, F.; Cappelletti, D.; Bartolomei, M.; Aquilanti, V.; Scotoni, M.; Vescovi, M.; Ascenzi, D.; Bassi, D. Orientation of benzene in supersonic expansions, probed by ir-laser absorption and by molecular beam scattering. *Phys. Rev. Lett.* **2001**, *86*, 5035-5038.

12. Brooks, P. R.; McKillop, J. S.; Pippin, H. G. Molecular beam reaction of K atoms with sideways oriented CF_3I. *Chem. Phys. Lett.* **1979**, *66*, 144-148.

13. Aquilanti, V.; Ascenzi, D.; Cappelletti, D.; Pirani, F. Velocity dependence of collisional alignment of oxygen molecules in gaseous expansions. *Nature* **1994**, *371*, 399-402.

14. Weida, M. J.; Parmenter, C. S. Aligning symmetric and asymmetric top molecules *via* single photon excitation. *J. Chem. Phys.* **1997**, *107*, 7138-7147.

15. Berndt, R.; Gaisch, R.; Gimzewski, J. K.; Reihl, B.; Schlittler, R. R.; Schneider, W. D.; Tschudy, M. Photon emission at molecular resolution induced by a scanning tunneling microscope. *Science* **1993**, *262*, 1425-1427.

16. Stranick, S. J.; Weiss, P. S. Alternating current scanning tunneling microscopy and nonlinear spectroscopy. *J. Phys. Chem.* **1994**, *98*, 1762-1764.

17. McCarty, G. S.; Weiss, P. S. Scanning probe studies of single-nanostructures. *Chem. Rev.* **1999**, *99*, 1983-1990.

18. Donhauser, Z. J.; Mantooth, B. A.; Kelly, K. F.; Bumm, L. A.; Monnell, J. D.; Stapleton, J. J.; Price, D. W. Jr.; Allara, D. L.; Tour, J. M.; Weiss, P. S. Conductance switching in single molecules through conformational changes. *Science* **2001**, *292*, 2303-2307.

19. Wu, S. W.; Ogawa, N.; Ho, W. Atomic-scale coupling of photons to single-molecule junctions. *Science* **2006**, *312*, 1362-1365.

20. Claridge, S. A.; Schwartz, J. J.; Weiss, P. S. Electrons, photons, and force: quantitative single-molecule measurements from physics to biology. *ACS Nano* **2011**, *5*, 693-729.

21. Bonnell, D. A.; Basov, D. N.; Bode, M.; Diebold, U.; Kalinin, S. V.; Madhavan, V.; Novotny, L.; Salmeron, M.; Schwarz, U. D.; Weiss, P. S. Imaging physical phenomena with local probes: from electrons to photons. *Rev. of Mod. Phys.* **2012**, *84*, 1343-1381.

22. Lang, N. D. Apparent barrier height in scanning tunneling microscopy. *Phys. Rev. B* **1988**, *37*, 10395-10398.

23. Zheng, X.; Mulcahy, M. E.; Horinek, D.; Galeotti, F.; Magnera, T. F.; Michl, J. Dipolar and nonpolar altitudinal molecular rotors mounted on an Au(111) surface. *J. Am. Chem. Soc.* **2004**, *126*, 4540-4542.

24. Monnell, J. D.; Stapleton, J. J.; Dirk, S. M.; Reinerth, W. A.; Tour, J. M.; Allara, D. L.; Weiss, P. S. Relative conductances of alkaneselenolate and alkanethiolate monolayers on Au{111}. *J. Phys. Chem. B* **2005**, *109*, 20343-20349.

25. Han, P.; Kurland, A. R.; Giordano, A. N.; Nanayakkara, S. U.; Blake, M. M.; Pochas, C. M.; Weiss, P. S. Heads and tails: simultaneous exposed and buried interface imaging of monolayers. *ACS Nano* **2009**, *3*, 3115-3121.

26. Mermin, N. D.; Wagner, H. Absence of ferromagnetism or antiferromagnetism in one- or two-dimensional isotropic heisenberg models. *Phys. Rev. Lett.* **1966**, *17*, 1133-1136.

27. Bruno, P. Absence of spontaneous magnetic order at nonzero temperature in one- and two-dimensional heisenberg and xy systems with long-range interactions. *Phys. Rev. Lett.* **2001**, *87*, 137203.

28. Ferris, J. H.; Kushmerick, J. G.; Johnson, J. A.; Yoshikawa Youngquist, M. G.; Kessinger, R. B.; Kingsbury, H. F.; Weiss, P. S. Design, operation, and housing of an ultrastable, low temperature, ultrahigh vacuum scanning tunneling microscope. *Rev. Sci. Instrum.* **1998**, *69*, 2691-2695.

29. Ulman, A. Formation and structure of self-assembled monolayers. *Chem. Rev.* **1996**, *96*, 1533-1554.

30. Smith, R. K.; Lewis, P. A.; Weiss, P. S. Patterning self-assembled monolayers. *Prog. Surf. Sci.* **2004**, *75*, 1-68.

31. Love, J. C.; Estroff, L. A.; Kriebel, J. K.; Nuzzo, R. G.; Whitesides, G. M. Self-assembled monolayers of thiolates on metals as a form of nanotechnology. *Chem. Rev.* **2005**, *105*, 1103-1169.

32. Weiss, P. S. Functional molecules and assemblies in controlled environments: formation and measurements. *Acc. Chem. Res.* **2008**, *41*, 1772-1781.

33. Saavedra, H. M.; Mullen, T. J.; Zhang, P. P.; Dewey, D. C.; Claridge, S. A.; Weiss, P. S. Hybrid approaches in nanolithography. *Rep. Prog. Phys.* **2010**, *73*, 036501.

34. Claridge, S. A.; Liao, W. S.; Thomas, J. C.; Zhao, Y.; Cao, H. H.; Cheunkar, S.; Serino, A. C.; Andrews, A. M.; Weiss, P. S. From the bottom up: dimensional control and characterization in molecular monolayers. *Chem. Soc. Rev.* **2013**, *42*, 2725-2745.

35. Baše, T.; Bastl, Z.; Šlouf, M.; Klementová, M.; Šubrt, J.; Vetushka, A.; Ledinský, M.; Fejfar, A.; Macháček, J.; Carr, M. J.; *et al.* Gold micrometer crystals modified with carboranethiol derivatives. *J. Phys. Chem. C* **2008**, *112*, 14446-14455.

36. Hohman, J. N.; Claridge, S. A.; Kim, M.; Weiss, P. S. Cage molecules for self-assembly. *Mater. Sci. Eng. R* **2010**, *70*, 188-208.

37. Baše, T.; Bastl, Z.; Plzák, Z.; Grygar, T.; Plešek, J.; Carr, M. J.; Malina, V.; Šubrt, J.; Boháček, J.; Večerníková, E.; *et al.* Carboranethiol-modified gold surfaces. A study and comparison of modified cluster and flat surfaces. *Langmuir* **2005**, *21*, 7776-7785.

38. Hohman, J. N.; Zhang, P.; Morin, E. I.; Han, P.; Kim, M.; Kurland, A. R.; McClanahan, P. D.; Balema, V. P.; Weiss, P. S. Self-assembly of carboranethiol isomers on Au{111}: intermolecular interactions determined by molecular dipole orientations. *ACS Nano* **2009**, *3*, 527-536.

39. Dameron, A. A.; Charles, L. F.; Weiss, P. S. Structures and displacement of 1-adamantanethiol self-assembled monolayers on Au{111}. *J. Am. Chem. Soc.* **2005**, *127*, 8697-8704.

40. Saavedra, H. M.; Barbu, C. M.; Dameron, A. A.; Mullen, T. J.; Crespi, V. H.; Weiss, P. S. 1-adamantanethiolate monolayer displacement kinetics follow a universal form. *J. Am. Chem. Soc.* **2007**, *129*, 10741-10746.

41. von Wrochem, F.; Scholz, F.; Gao, D.; Nothofer, H.-G.; Yasuda, A.; Wessels, J. M.; Roy, S.; Chen, X.; Michl, J. High-band-gap polycrystalline monolayers of a 12-vertex *p*-carborane on Au(111). *J. Phys. Chem.* **2010**, *1*, 3471-3477.

42. Spokoyny, A. M.; Machan, C. W.; Clingerman, D. J.; Rosen, M. S.; Wiester, M. J.; Kennedy, R. D.; Stern, C. L.; Sarjeant, A. A.; Mirkin, C. A. A coordination chemistry dichotomy for icosahedral carborane-based ligands. *Nat. Chem.* **2011**, *3*, 590-596.

43. Wiesendanger, R.; Eng, L.; Hidber, H. R.; Oelhafen, P.; Rosenthaler, L.; Staufer, U.; Güntherodt, H. J. Local tunneling barrier height images obtained with the scanning tunneling microscope. *Surf. Sci.* **1987**, *189-190*, 24-28.

44. Olesen, L.; Brandbyge, M.; Sørensen, M.; Jacobsen, K.; Lægsgaard, E.; Stensgaard, I.; Besenbacher, F. Apparent barrier height in scanning tunneling microscopy revisited. *Phys. Rev. Lett.* **1996**, *76*, 1485-1488.

45. Rusu, P.; Brocks, G. Work functions of self-assembled monolayers on metal surfaces by first-principles calculations. *Phys. Rev. B* **2006**, *74*, 073414.

46. Jain, J.; Jain, A. Displacement measurement and its application in interframe image coding. *IEEE Trans. Comm.* **1981**, *29*, 1799-1808.

47. Love, N. S.; Kamath, C. An empirical study of block matching techniques for the detection of moving objects. *CASC, LLNL. Livermore* **2006**, 1-36.

48. Kristiansen, K.; Stock, P.; Baimpos, T.; Raman, S.; Harada, J. K.; Israelachvili, J. N.; Valtiner, M. Influence of molecular dipole orientations on long-range exponential interaction forces at hydrophobic contacts in aqueous solutions. *ACS Nano* **2014**, *8*, 10870-10877.

49. Metropolis, N.; Rosenbluth, A. W.; Rosenbluth, M. N.; Teller, A. H.; Teller, E. Equation of state calculations by fast computing machines. *J. Chem. Phys.* **1953**, *21*, 1087-1092.

50. Pascual, J.; Jackiw, J.; Kelly, K.; Conrad, H.; Rust, H. P.; Weiss, P. S. Local electronic structural effects and measurements on the adsorption of benzene on Ag(110). *Phys. Rev. B* **2000**, *62*, 12632-12635.

51. Claridge, S. A.; Thomas, J. C.; Silverman, M. A.; Schwartz, J. J.; Yang, Y.; Wang, C.; Weiss, P. S. Differentiating amino acid residues and side chain orientations in peptides using scanning tunneling microscopy. *J. Am. Chem. Soc.* **2013**, *135*, 18528-18535.

52. Kim, J.; Rim, Y. S.; Liu, Y.; Serino, A. C.; Thomas, J. C.; Chen, H.; Yang, Y.; Weiss, P. S. Interface control in organic electronics using mixed monolayers of carboranethiol isomers. *Nano Lett.* **2014**, *14*, 2946-2951.

53. Stranick, S. J.; Parakh, A. N.; Tao, Y.-T.; Allara, D. L.; Weiss, P. S. Phase separation of mixed-composition self-assembled monolayers into nanometer scale molecular domains. *J. Phys. Chem.* **1994**, *98*, 7636-7646.

54. Smith, R. K.; Reed, S. M.; Monnel, J. D.; Lewis, P. A.; Clegg, R. S.; Kelley, K. F.; Bumm, L. A.; Hutchison, J. E.; Weiss, P. S. Phase separation within a binary self-assembled monolayer on Au{111} driven by an amide-containing alkanethiol. *J. Phys. Chem. B* **2001**, *15*, 1119-1122.

55. Hampton, J. R.; Dameron, A. A.; Weiss, P. S. Double-ink dip-pen nanolithography studies elucidate molecular transport. *J. Am. Chem. Soc.* **2006**, *128*, 1648-1653.

56. Nuzzo, R. G.; Dubois, L. H.; Allara, D. L. Fundamental studies of microscopic wetting on organic-surfaces. 1. Formation and structural characterization of a self-consistent series of polyfunctional organic monolayers. *J. Am. Chem. Soc.* **1990**, *112*, 558-569.

57. Poirier, G. E. Characterization of organosulfur molecular monolayers on au(111) using scanning tunneling microscopy. *Chem. Rev.* **1997**, *97*, 1117-1127.

58. Dameron, A. A.; Charles, L. F.; Weiss, P. S. Structures and the displacement of 1-Adamantanethiol self-assembled monolayers on Au{111}. *J. Am. Chem. Soc.* **2005**, *127*, 8697-9704.

59. Kim, M. H.; Hohman, J. N.; Morin, E. I.; Daniel, T. A.; Weiss, P. S. Self-assembled Monolayers of 2-adamantanethiol on Au{111}: control of structure and displacement. *J. Phys. Chem. A* **2012**, *113*, 3895-3903.

60. Stipe, B. C.; Rezaei, M. A.; Ho, W. Single-molecule vibrational spectroscopy and microscopy. *Science* **1998**, *280*, 1732-1735.

61. Lee, H. J.; Ho, W. Structural determination by single-molecule vibrational spectroscopy and microscopy: contrast between copper and iron carbonyls. *Phys. Rev. B* **2000**, *61*, 347-350.

62. Lewis, P. A.; Inman, C. E.; Maya, F.; Tour, J. M.; Hutchison, J. E.; Weiss, P. S. Molecular engineering of the polarity and interactions of molecular electronics switches. *J. Am. Chem. Soc.* **2005**, *127*, 17421-17426.

63. Baber, A. E.; Jensen, S. C.; Sykes, E. C. H. Dipole-driven ferroelectric assembly of styrene on Au{111}. *J. Am. Chem. Soc.* **2007**, *129*, 6368-6369.

64. Han, P.; Akagi, K.; Canova, F. F.; Mutoh, H.; Shiraki, S.; Iwaya, K.; Weiss, P. S.; Asao, N.; Hitosugi, T. Botton-up graphene-nanoribbon fabrication reveals chiral edges and enantioselectivity. *ACS Nano* **2014**, *8*, 9181-9187.

65. Ferris, J. H.; Kushmerick, J. G.; Johnson, J. A.; Yoshikawa Youngquist, M. G.; Kessinger, R. B.; Kingsbury, H. W.; Weiss, P. S. Design, operation, and housing of an ultrastable, low temperature, ultrahigh vacuum scanning tunneling microscope. *Rev. Sci. Instrum.* **1998**, *69*, 2691-2695.

66. Chan, M. H.; Yu, Y. B.; Constantinides, A. G. Variable size block matching motion compensation with applications to video coding. *IEEE Proc. I* **1990**, *137*, 205-212.

67. Nie, Y.; Ma, K. K. Adaptive rood pattern search for fast block-matching motion estimation. *IEEE Trans. Image Process.* **2002**, *11*, 1442-1449.

CHAPTER 5

Exchange Reactions between Alkanethiolates and Alkaneselenols on Au{111}

5.1 Introduction

Two-dimensional assembly and control are key aspects in testing self-assembled monolayers. The well-known ionic/covalent gold-sulfur bond between alkanethiol and the gold surface remains incompletely understood even after 30 years of study. Scanning probe microscopy, X-ray diffraction, and computation now support the generally accepted model of a S/Au-adatom complex [1-6]. This complex exists, which has sulfur atoms bound to gold atoms or on opposite sides of the gold adatom in a barbell configuration [2-4, 6-15]. Gold adatoms play an important role in the motion of gold-thiolate complexes [1] and conformational changes of molecular switches [16]. Many prominent questions remain regarding this adatom complex. Can an adatom complex transition from one complex to another, is it ordered or disordered? Are gold adatoms derived from the unreconstructed surfaces, which leave behind vacancy sites or are they derived from the initial lift of the herringbone reconstruction [5-7, 17-19]? What is the importance of a proposed barbell motif relative to other binding models in the context of molecular-exchange and place-exchange reactions [20-25]? In order to answer these questions, we studied exchange reactions between alkanethiols and alkaneselenate monolayers. Exchange of alkaneselenol molecules into a preformed alkanthiolate SAM occurs on a substrate displaying complete Au-thiolate complex coverage. The reaction products of this reaction are investigated and since the Au{111} herringbone reconstruction is already lifted by thiolate deposition, Au-S/Se exchange reactions provide an opportunity to examine reaction products in the context of the Au-adatom complex [1, 17].

Electronic coupling of molecules to the substrate and the overall oxidative and thermal stability of SAMs are improved when replacing thiols with selenols [26-37]. Selenium is more strongly bound to the gold substrate than sulfur [38, 39]. Studies of likely binding sites for selenium are still developing, and have not taken into account discoveries in the chemistry of sulfur-gold adatom complexes. The main interest here is the configuration of the selenolate attachment and observing coexisting structures of the two chalcogenolates. This work may provide insight into whether or not selenium is attached to the substrate in a manner similar to sulfur.

In this chapter, single-component alkanethiolate and alkaneselenolate films on Au{111} are compared, and the structures formed by the kinetics of the rapid molecular exchange reaction between gold-bound alkanethiolates and alkaneselenols are reported. Furthermore, 2D place-exchange reactions between adsorbed thiolates and selenolates induced by STM tip are observed, enabling the investigation of both gold-thiolate and gold-selenolate attachment chemistry. Initially, our observations suggest gold-selenolate structure occupies the same binding structure and configuration as the gold-thiolate complex and as selenolate coverage increases, there is a transition to a new interface structure.

5.2 Results and Discussion

5.2.1 Morphological Comparisons of Alkanethiolate and Alkaneselenolate Monolayer Structures

Molecular- and atomic-scale resolution are possible using the scanning tunneling microscope. It, however, does not allow for chemical identification beyond the conductance and relative apparent sizes of molecules measured [40-42]. In order to examine mixed order systems involving alkanethiolates and alkaneselenolates, we employ different alkyl chain lengths; a

shorter alkyl chain for the thiolate matrix 1-decanethiolate **(C10)** and a longer 1-dodecaneselenolate **(C12Se)**. The difference in length allows for the identification of molecular species at different stages of the exchange reaction [27, 43]. A morphological comparison of single-component **C10** and **C12Se** SAMs on Au{111} are depicted in Figure 5.1.

When an annealed **C10** SAM is imaged (Figure 5.1 A-C), it reveals the well-ordered hexagonal lattice of molecules in the $(\sqrt{3} \times \sqrt{3})R30°$ configuration. Two important classes of defects exist: domain boundaries and gold substrate step edges (of which the circular depressions shown in Figure 5.1A, substrate vacancy islands, are a subclass) [36, 44-47]. Ordered molecular domains have different alkyl chain azimuthal orientations with domain boundaries separating them [46, 48-50] or offsets of the lattice of attachment. Depending on the configuration of molecules at that interface, domain boundaries are more or less protruding than the surrounding domains [46]. Domain boundaries usually align with the close-packed lattice direction oriented 60° to one another as seen in highly ordered films (Figure 5.1 A-C). When one or more molecules are missing from a well-ordered lattice, it is referred to as a molecular vacancy. This is rare for well-ordered alkanthiolate films. The other class of defect is known as substrate step edges, which are a single gold atom high transition from one flat terrace to the next and are functionally identical to gold terrace step edges in structure and behavior.

Previous studies have shown that despite having identical alkyl chain geometries of alkyl chains, **C12Se** films are noticeably dissimilar from alkanethiolate films (Figure 5.1D and 5.1E) [26, 27, 51]. The characteristic alkanethiolate domain boundary structures are absent as observed in **C10** SAM images [46, 52]. Alternatively, the Moiré patterns of topographic differences are readily apparent in STM images of the **C12Se** film (Figure 5.1D) and originate due to differences in the lattice constants of the gold substrate and the overlying molecular layer in smooth

continuous variation of apparent height by ~1 Å. These features generally align with the substrate, rotated with respect to one another by multiples of 30°, as seen previously in annealed monolayers of 1-adamantaneselenolate [32].

After **C12Se** adsorption, substrate step edges align along the close-packed directions of the gold substrate. High-resolution STM imaging allows us to locate vacancy trenches in single-component **C12Se** SAMs. These configurations are structurally consistent with the round vacancy islands found in **C12** SAMs. For each trench, the median apparent height is ~2.3 Å lower than the median apparent height for each trench of the surrounding terrace, which is indicative of a gold substrate monatomic step. These trenches tend to align with the crystallographic close-packed direction of the gold substrate. Parallel **C12Se** molecular rows, which are dissimilar from the surrounding lattice, often accompany the missing row of the vacancy trench. A common image at high resolution is shown in Figure 5.1F. The rows adjacent to the trench are either less protruding than the median height of the surrounding terrace, or more protruding by a value of 1 Å. Depending on the immediate local environment, a variety of bonding configurations for Au-Se interactions are possible as highlighted by these features.

The crystallographic structure of the gold substrate is reflected by **C12Se** SAM structure, and the differences in the apparent height of various features indicate a range of binding configurations coexisiting with the gold substrate, a trait previously reported in the study of 1-adamantaneselenolate on Au{111} [32]. It can be confirmed from our observations that the formation of the **C12Se** SAM lifts the gold herringbone reconstruction and spawns vacancy islands as the selnolate-gold interaction results in straightened substrate step edge features, and produces small vacancy trenches. Our previous suggestion of gold-selenolate bond promiscuity is consistent with the straightening and existence of multiple binding sites, and other recent

examples of acceptable binding configurations for selenium to gold [26, 27, 32, 53]. The gold substrate also rapidly straightens, which implies that the gold-selenolate complex is more mobile than its sulfur counterpart. We will return to discuss the mobility of the selenolate and the hypothesized gold-selenolate complex below.

5.2.2 Molecular-Exchange and Place-Exchange Reactions of Self-Assembled Monolayers

We now need define the phenomena and timescales of reactions that occur between molecules in self-assembled monolayers. Two distinct types of exchange reactions are described and treated separately here. The first type of reaction is defined as a molecular exchange (or displacement) reaction as the replacement of an adsorbed molecule by a second species and is accomplished by immersion of a SAM-coated substrate into a solution or vapor of the replacing chemical [54-56]. The term, "insertion" is the initial stage of a molecular exchange reaction, where molecules of the second species can decorate the defect sites of the preformed film [54, 57]. These sites are known to provide access to the substrate for other species and for chemical reactions, and are occupied first [24, 26, 45, 48, 56, 58-67]. Defects are critical to both insertion and displacement.

A place-exchange reaction is the second type of reaction and is a position swap between proximate molecules in a 2D lattice with no desorption of either molecule. The molecule **C12Se** is incorporated into the **C10** SAM by a molecular exchange reaction that is arrested in order to investigate place-exchange reactions which are mediated by defects [22, 68].

Four primary factors mediate exchange between adsorbed molecular assemblies and molecules in solution: the chemistry of the molecule/substrate attachment, molecular geometries, intermolecular forces, and the type and density of defects (of both the supramolecular assembly and the substrate, i.e., by access to the substrate). In molecular self-exchange (e.g., the exchange

between a 1-dodecanethiolate monolayer and 1-dodecanethiol), molecules are kinetically trapped in domains and exchange occurs mainly at defects sites [20]. Engineering molecular exchange reactions requires the constituent molecules to be tailored. For example, a combination of weak intermolecular interactions and low surface density make 1-adamanthanethiolate SAMs susceptible to molecular exchange by *n*-alkanethiols [54, 57, 69]. Furthermore, monolayer defects and disorder can be induced by exothermic reactions [70, 71]. The attachment chemistry also plays an important role. It has previously been shown that selenols outcompete sulfur for binding sites on Au{111}. Due to the similarity of packing densities of **C12** and **C12Se** SAMs, a thermodynamic drive towards increased coverage is not present [26, 57, 72]. The Se-Au bond is stronger than the S-Au bond; we have shown that the Se-Au bond is more promiscuous in terms of binding sites [26, 73]. Previous studies by Garrell and coworkers have shown a strong surface preference for benzeneselenolates over benzenethiolates, due to the higher acidity of the selenol group relative to the thiol [38]. Similar experiments conducted on copper-supported monolayers involving thiolates and selenolates did not show strong preferences for either chalcogen [74, 75]. Various substrates can be engineered to promote exchange [76, 77].

In full-coverage monolayers, place-exchange between adsorbed thiolates is generally slow [20, 21, 24, 57, 78-80]. In general, monolayer dynamics within crystalline domains of nearly complete SAMs occur over short distances and time scales on the order of hours or longer. Notable differences are observed at defect sites, where dynamics are relatively fast, however there is little precedent for covalently bound molecules to transit long distances [59]. Previous studies have shown apparent site-hopping of adamantaneselenolates on Au{111}, although these motions are thought to occur between adjacent sites separated by only a few

Ångströms [32]. The even greater promiscuity of amine-Au bonds might be expected to lead to enhanced mobility of these species [81].

5.2.3 Determination of Exchange Kinetics by Infrared Spectroscopy

Infrared reflectance absorption spectroscopy (IRRAS) is used to measure the exchange kinetics of SAM exchange/replacement. This technique has several advantages for tracking changes in monolayers: gold is highly reflective, carbon-hydrogen bonds absorb strongly between 2800 and 3000 cm^{-1}, monolayer coverage down to a few percent can be detected, and spectral data provides both coverage and structural information.

A typical spectrum for a **C12Se** SAM, is shown in Figure 5.2A, is comparable to that of most alkanethiolates on gold. Five dominant spectral features exist: methylene symmetric and asymmetric stretches at 2850 and 2918 cm^{-1}, respectively, methyl symmetric and asymmetric stretches at 2877 and 2963 cm^{-1}, respectively, and a weak band associated with a Fermi resonance of the symmetric methyl stretch with a methyl deformation mode, presented as a shoulder of the methylene asymmetric stretch [82-84]. Intensity and position of the methylene asymmetric stretch correlate to monolayer order. A highly ordered, solid-like film includes the peak position at 2918 cm^{-1}. The intensity of the methylene symmetric stretch relative to the other peaks is lower than those reported for selenolate monolayers deposited from dialkyldiselenide [72]. The microscopic structure observed for monolayers deposited from dialkyl diselenide (a surface that has been reported to show a substantially larger number of gold substrate defects as compared to our observations for alkaneselenol films) appears topographically dissimilar to monolayers fabricated from alkaneselenol. [85]. A more in-depth analysis of alkaneselenol versus dialkyl diselenide self-assembly characterization is necessary.

The partial coverage of alkanethiolate monolayers is determined by an important spectral feature, the methyl symmetric stretch (2877 cm^{-1}); taking the ratio of the peak area at each time point to the peak area after 24 h displacement generates fractional coverage. A largely uniform intensity is given by the symmetry of the group over a range of possible standing-up configurations which makes it a useful metric for coverage in mixed systems of standing-up phase alkanethiolate SAMs [57, 84]. In the case of **C12Se** exchanging **C10**, the intensity of the 2877 cm^{-1} peak is constant throughout the experiment, since coverage and orientation of the terminal methyl groups remain static. Accurate observation of the exchange reaction is difficult due to the spectral interference being too high, and monitoring intensity changes of the methylene asymmetric 2919 cm^{-1} peak is unreliable. Spectral interference of the base monolayer is removed by depositing a perdeuterated dodecanethiolate (**D12**) monolayer, with the key assumption that the chemistry of **D12** film exchange is the same as that of a **C12** monolayer. Unlike our STM measurements and for simplicity, alkyl chains of identical length are employed in order to simplify interpretation of the kinetics. Figure 5.7 shows an infrared spectrum of a **D12** monolayer.

The progression of the exchange reaction between a spectroscopically transparent **D12** monolayer exposed to an ethanolic solution of **C12Se** is shown in Figure 5.2A and 5.2B. As the exposure time increases, the C-H peaks of the **C12Se** film start emerging, and the reaction terminates after complete **D12** monolayer displacement. Minimal reorganization occurs (for example, we see no evidence of a transition between lying-down and standing-up phases [86], as might be observed for deposition onto a bare substrate) due to the relative ratio of peak intensities remaining static throughout the displacement process. Therefore, molecules are found in their near-final orientations shortly after incorporation into the film. Figure 5.2B illustrates the

fractional coverage of **C12Se** monolayers versus immersion time. As seen in Figure 5.3, the STM images reveal an initial phase of slower adsorption dominated by insertion at defect sites, followed by a period of more rapid replacement, and the rate ultimately slows as the reaction approaches completion. The main source of error is sample-to-sample variability. Every gold substrate features a characteristic (and unquantified) fraction of steps and defects [57, 87]. As the exchange reaction is initiated by insertion at defect sites, slight differences in sample defect density can have large cumulative effects on the final rate of exchange. These variations are reflected in the standard deviation of fractional coverage at each time point.

In order to describe phase transitions in three-dimensional metal alloys, the Johnson, Mehl, Avrami, and Kolmogorov (JMAK) model was devised [88-90]. The site-saturated nucleation JMAK2 model was previously used to describe perimeter-dependent island growth of 1-adamantanethiolate exchange by **C12**, and given as:

$$\theta(t) = 1 - e^{(\kappa t)^2} ,$$

where κ is the rate constant [57]. Recent studies state that this model can be used in general to describe 2D film exchange [91]. For comparison, the kinetic data are fit to a variety of other models, including pure diffusion, first-order, second-order, and diffusion-limited Langmuir models, and the constant nucleation-rate JMAK3 model. In Figure 5.2B, the JMAK2 model, best represents the data and is consistent with our observations of the reaction progression (a slower initial rate followed by a more rapid rate as coverage increases) is used to fit the kinetic data. Plotting the displacement rate versus the concentration of **C12Se** on a logarithmic scale gives a slope of ~1, as shown in Figure 5.2C, implying that the rate is directly proportional to the concentration of **C12Se**.

At nearly all conditions investigated, we observe that alkanethiolate monolayers are unstable in the presence of alkaneselenols. Codeposition results in single-component **C12Se** monolayers, until the molar ratio approaches 100:1 in favor of the **C12**. Figure 5.2D shows the sharp transition between full-coverage **C12Se** and **D12** monolayers as a function of mole fraction. In their work on benzenethiolates and selenolates, Huang et al. linked the faster kinetic exchange of benzenethiol and benzeneselenol to the pK_a of the selenol, suggesting that the deprotonated forms of the selenols were responsible for the faster exchange kinetics [38]. Our results examining the effect of solution pH on alkanethiolate displacement by selenol corroborate this finding: **C12Se** exchange with **C10** SAMs was faster after addition of aqueous sodium hydroxide to the ethanolic selenolate solution. It remains unclear whether this increase in exchange rate is due primarily to deprotonation of the replacing species, or whether the hydroxide is facilitating abstraction of molecules from the preexisting monolayer. In all cases of hydroxide-catalyzed exchange, the methylene asymmetric stretch (~2918 cm^{-1}) is observed to increase in intensity by a factor of two to three and shift to ~2930 cm^{-1}, indicative of poor order in the resulting film [57, 84]. Annealing the film in the same solution at elevated temperature for 24 h and then repeating the spectroscopic analysis reveals a monolayer film indistinguishable from one deposited at room temperature, evidence of poor ordering after base-catalyzed displacement of thiolate by selenolate. Figure 5.8 shows the collected spectral and kinetic results.

5.2.4 Molecular Exchange of Decanethiolate by Dodecaneselenol

A preformed **C10** SAM is exposed to a 10 mM ethanolic **C12Se** solution for 1 min. The STM micrographs in Figure 5.3A and 5.3A' display rapid insertion of **C12Se** into the **C10** lattice, especially at domain boundaries and step edges. The selenolates appear to occupy hexagonal lattices and incorporate commensurately to the lattices of the surrounding thiolates (Figure

5.3A’). Insertion has also been observed at isolated locations within ordered domains, possibly due to **C12Se** insertion at molecular vacancy defect sites (an example image is shown in Figure 5.6).

In the STM images depicted here, **C12Se** molecules appear somewhat more protruding (~0.7 Å), than the neighboring **C10** molecules. The measured apparent height is related to the configuration of the STM tip, through which the tunneling current passes. Changes in the tip state result in variations of the observed relative apparent height. In some cases, inversion of the relative selenolate and thiolate conductance occurs after changes in the electronic properties of the probe. This tendency for tip-dependent conductance changes must be carefully monitored to ensure that probe variations are distinguished from changes in molecular binding site. Figure 5.6 shows examples of conductance reversal on tip state changes.

Additional exposure to solution results in rapid increases in the relative **C12Se** coverages, with each site of **C12Se** insertion becoming a nucleation site for **C12Se** island growth [57]. After 4 min of **C12Se** exposure, **C12Se** is no longer confined to the regions in close proximity to **C10** defect sites, and occupies a substantial fraction of the surface. The relative apparent heights have inverted, with **C12Se** now appearing less protruding. Ordered islands are the dominant configuration of the residual **C10**. Such large thiolate islands (appearing as the protruding features shown in Figure 5.3B and 3B') have edge lengths of 100-500 Å. The largest, most ordered SAM domains are similarly most resistant to molecular exchange, as there are few internal defects to provide initiation sites for selenolate displacement, requiring molecular exchange to occur from the domain edges inwards.

The displacement reaction does not appear to be a smooth progression between continuous domains of **C10** to **C12Se**. The images in Figure 5.3C and 5.3C' depict striped

features of high- and low-conductance rows. Comparing apparent heights of these striped regions reveals they are composed of features that match the relative height of thiolate islands separated by less-protruding features. The more protruding features can be attributed to structures partially composed of residual **C10**. We use apparent height as the marker for chemical identification. Inserted **C12Se,** at low-coverage, appears more protruding than **C10** in STM images, while striped features are equal or lower in apparent height than **C10**. As the infrared analysis suggests no change in absolute molecular coverage, these lower-height features are consistent with a different bonding configuration of the **C12Se** as relative coverage increases. The reaction progresses with incoming selenolates dismantling the organized domains of the **C10** film, making coalescence into a single-component **C12Se** film rapid. Displacement seems to favor the direction along rows; this process appears to be anisotropic.

In contrast to the low-coverage example, the **C12Se**-dominated regions now appear less protruding than the **C10** matrix. The relative conductance of thiolates and selenolates is strongly influenced by the underlying substrate binding site as evidenced in Figure 5.3B'. This image shows selenolates in two distinct conductance configurations: at the top left are selenolates that appear to protrude more and are lattice matched to the **C10**, and on the right is the striped selenolate domain, which appears to protrude less than the **C10** island.

The apparent height of **C12Se** is dependent on the binding site. As stated previously, selenolates inserted at defects appear protruding from and lattice matched to the **C10** lattice, which adopts a $(\sqrt{3} \times \sqrt{3})R30°$ lattice (and related superstructures). Once the selenolates collapse into their own favored bonding configuration, the alkanethiolate islands appear to protrude in STM images from the surrounding alkaneselenolate lattice by ~0.7 Å (for the conditions shown), in spite of the **C12Se** molecules having a longer chain length. This measurement is in close

agreement with our previously reported value for **C12** inserted into a **C12Se** SAM, where **C12** molecules in STM images appeared to protrude from preformed **C12Se** SAMs [27].

After 7 min exposure to a **C12Se** solution, all **C10** molecules were replaced by **C12Se**. This monolayer is organized differently than the directly deposited **C12Se** SAM, yet the variations in apparent height in STM images remain. As shown in Figure 5.3C and 3C', the structure is primarily striped, demonstrating the linear propagation of the displacement reaction. Analogous to the single-component **C12Se** film, the difference between the most and least protruding molecules in STM images on single terraces is approximately 1 Å.

Displacement reactions preserve the integrity of the top layer of the gold. No aforementioned "trench" vacancy islands are observed after the alkaneselenolates have occupied the substrate surface, and the vacancy islands that form after thiolate SAM assembly are preserved by the new monolayer. This observation presents evidence that vacancy island formation is tied directly to lifting the Au herringbone reconstruction at the initial stage of SAM formation, and thus no new vacancy islands can form after thiolate replacement by selenolate. Similarly, we do not observe adatom islands, as would be expected if thiolates were abstracted and gold adatoms left behind [8, 10]. The longer **C12Se** molecules appear lattice matched to the **C10** in the early stages of the displacement reaction, due to the **C12Se** molecules being trapped in the same binding configuration as the sulfur in the **C10** SAM. As coverage increases, the selenolates are no longer confined to thiolate-like configurations and adopt their own preferred binding configurations.

5.2.5 Bias-Induced Place Exchange of Selenolates with Thiolates

In order to tailor physical and chemical properties at interfaces, SAM coverage, structure and composition must be altered. Phase-separated molecules can be selectively moved and

removed *via* electrochemistry, where domains having weaker intermolecular interactions desorb at lower potential [92, 93]. The STM probe has long been used to manipulate atoms and molecules directly, and to perform nanoscale lithographic patterning [94-99]. The STM tip can be used to pattern alkanethiolate monolayers at relatively high voltages (sample bias of +3 V) [100-102]. We have observed that the threshold for induced motion of the selenolates is lower, with motion observed at low sample biases, e.g., +1 V, and that alkaneselenolates can be manipulated selectively. This may be associated to the promiscuous binding of selenolates to Au (relative to thiolates) [26].

For imaging without disturbing the SAM, we use a sample bias of -1 V at a tunneling current of 3 pA. Imaging at a sample bias of +1 V induces physical reorganization of thiolate/selenolate mixed monolayers. The overall film order is retained after reorganization. At high selenolate coverage, the effect becomes more dramatic: both thiolate and selenolate domains become disordered, and mottled configurations of high and low conductance domains are observed (images can be found in Figure 5.9).

In Figures 5.4A and 5.4A', STM images depict **C12Se** molecules appear protruding relative to the **C10** lattice. Upon bias polarity reversal (to +1 V sample bias), the positions of individual **C12Se** molecules are no longer well defined, as shown in Figure 5.4B. This "noise" is attributed to molecular place-exchange reactions and motion occurring at timescales faster than imaging [103-106]. Each image is recorded over ~4 min by rastering the tip over the interface, where the tip encounters individual protruding molecules at many positions, rather than over a single, well-defined binding site. Returning to -1V sample bias in image 5.4C arrests the place-exchange reactions, and the selenolates are seen again at well-defined sites. The number of molecules visible in the recorded area are approximately the same before and after bias-induced

shuffling. A change in the tip geometry after bias reversal resulted in faint "double tip" artifacts to the lower right of all high-aspect-ratio protrusions, giving the false impression that more **C12Se** molecules are present in the images in Figure 5.4C, C'. Selenolates are then observed to be incorporated into the centers of ordered domains. The movement of molecules to the new sites results in increased disorder, while the overall domain structures before and after place-exchange reactions are nominally the same. Protruding **C12Se** molecules are thus accompanied by depressions in the **C10** lattice that arise from the additional free space created by decreases in the local alkyl chain crystallinity. The structures of the **C10** domain boundaries have similarly been reconfigured.

While bias-induced place-exchange reactions are localized, the reactions are not limited to the specific position of the tunneling junction. The monolayer was reconfigured as far as 50 nm from the region imaged at +1 V substrate bias, as seen in Figure 5.4C'. The tip scanned only over a 250 Å × 250 Å region, but molecules have been rearranged over the 500 Å × 500 Å terrace. Imaging at distances greater than 500 Å from the region of induced motion reveal no apparent molecular place exchange (Figure 5.10).

We demonstrated the ability to manipulate small groups of molecules with localized, short-duration voltage pulses, although the 500 Å range over which motion can be induced made directed assembly of individual molecules into specific patterns impractical. A small cluster of protruding **C12Se** molecules at which the STM tip is positioned is shown in Figure 5.5. The sample bias is set to +1 V at 3 pA tunneling current for 5 sec. Subsequent imaging at -1 V sample bias revealed extensive rearrangement of the local structure that continued long after the initial pulse. In many cases, however, short pulses had no obvious effects on the local structure at

the scale imaged, but responses at distances larger than the imaging window could not be excluded. The structure observed continues to evolve faster than the minute timescale.

5.2.6 Implications for the Gold-Adatom Complex

No evidence exists for the restructuring of the gold substrate during complete exchange reactions. **C12Se** SAMs deposited by displacement of **C10** show evidence of the topographic variations characteristic of the selenolate system, but show vacancy islands characteristic of the **C10** system (Figure 5.3C, 5.3C'). These features add to the existing evidence that the formation of vacancy islands is due to dynamics between the substrate and binding chalcogen as the herringbone reconstruction of the gold is lifted [2, 18, 19, 107]. We conclude that the configuration of the gold-thiolate association is conserved after the initial molecular exchange reaction, and additional reconfiguration that does not involve loss of gold atoms occurs as alkaneselenolate coverage increases.

Our observations corroborate two distinct binding modes for selenolate on gold. In the initial stages of the displacement reaction, **C12Se** molecules appear more protruding from the **C10** lattice, and the apparent heights of the inserted **C12Se** are similar to the expected heights for **C12** molecules inserted into **C10** lattices. We propose that the selenolates occupy the binding sites previously occupied by thiolates. At the initial stages, the reaction exchange is slow, and **C12Se** molecules are predominantly found at defects in the **C10** SAM. In the later stages of the replacement reaction, the **C12Se** molecules appear lower than the **C10** domains, and propagation of **C12Se** appears to occur in bands several molecules wide, with stripes of **C10** remaining. We propose that the gold-thiolate complexes exhibit long-range order in highly annealed films, thus enabling linear stripes of selenolates to propagate over long distances (hundreds of Ångströms).

Several independent groups have proposed a barbell configuration of the gold adatom-thiolate complex [4, 13, 32, 108, 109]. Several of our observations mesh well with this concept for the gold-adatom complex. The early, high conductance stage of **C12Se** insertion can be seen as an alkaneselenolate binding to and displacing the alkanethiolate from this complex, conserving the structure (Figures 5.3A, 5.3A'). As the coverage of selenolates increases, a change in structure and apparent heights of the selenolates is observed (Figures 5.3B, 5.3B'). A number of mechanistic pathways exist that can explain the progression of the displacement mechanism. The observed accelerated displacement after insertion is not accounted for when thiolate desorption at SAM and substrate domain boundaries frees binding sites for selenol insertion from solution [20, 57, 110]. A ligand exchange model provides a mechanistic pathway for displacement, in which a selenolate binds at the thiolate-occupied complex adjacent to a defect site, and the thiolate is subsequently induced to desorb. This mechanism would require formation of a transient $Au(SeR)(SR)_2$ complex prior to desorption, which would likely not be observable at room temperature or at the slow experimental imaging timescales used in this study.

It is unclear how to resolve the barbell model with the mobility of the gold-selenolate complex and the patterns formed by the progression of the selenol-thiolate exchange reaction. Gold-thiolate complex mobility has long been an important concept for explaining the order and dynamics of alkanethiolate monolayers; however, the mobility we observe in the bias-induced reactions (as shown in Figure 5.4) is unprecedented. Translation distances on the order of 5 nm (corresponding to a minimum of 10 molecular lattice site hops to reach the new location) for both individual and grouped **C12Se** are observed during the tip-induced place-exchange reactions. One possible mechanism that relies on the transient trichalcogen gold complex described above is the turnstile mechanism. If the selenolate dissociates from a complex and can

hop to an adjacent complex after bias induced activation, then the thiolate on the destination complex could in turn step back to effectively switch sites with the selenolate. Within the alkyl backbone superlattice and in the absence of available solution phase interactions favoring abstraction, subsequent transfer of a thiolate to the site vacated by the selenolate would be likely. The packing of the alkyl chains would be expected to deteriorate after repeated place exchanges by this mechanism, and this is observed as an increase in depressions in the monolayer (e.g., in comparison of Figures 5.5A' and 5.5C'). At higher selenolate coverage, the mixed monolayer system becomes randomly mixed and order is lost after imaging at +1 V sample bias, as mentioned above. On the other hand, the gold adatom complexes may instead be swapping sites with neighbors, consistent with the observed mobility of the complex. Additional experiments and theoretical modeling will be required to address the question of the buried structure and mechanism of both molecular and place-exchange reactions between thiolate/selenolate gold complexes.

5.3 Conclusions and Prospects

Investigating SAM molecular exchange reactions through the lens of gold adatom complexes provides a variety of insights for interpreting the structural evolution from one complex supramolecular system to another, significantly less studied system. Atomic-scale configurations of gold-chalcogen bonds are deceptively complex problems. Numerous phases of even simple alkanethiolates and alkaneselenolates on Au{111} exist [26, 86, 111]. We observed a monolayer transition from a full-coverage sulfur-bound **C10** SAM to a full-coverage selenium-bound **C12Se**, taking note of how the gold substrate directs the progression of the reaction, and the structures of the products.

Numerous structural differences are noted when comparing single-component **C10** and **C12Se** SAMs. We reported substrate vacancy trenches in single-component **C12Se** SAMs, which become visible as narrow, linear vacancy islands that align with the close-packed substrate lattice directions. The ±1 Å apparent height variations of highly ordered **C12Se** are grouped in similarly aligned substrate-matched patches and rows. Boundaries between groups of different apparent heights are less delineated than the domain boundaries in ordered **C10** domains. These observations are consistent with the viewpoint that there are both more varied binding sites available for selenolates and associated adatom complexes, and that apparent height is highly dependent on the Au-Se attachment geometry.

The adatom complex (or of any other hypothesized motif) is conserved following the exchange reaction replacing **C10** with **C12Se.** This replacement does not generate new vacancy trench features or adatom islands, suggesting that there is no ejection or reconstruction on thiolate replacement by selenium. The contrast between the linear propagation of the thiolate/selenol displacement versus the more radial growth mechanism of 1-adamantanethiolate displacement by alkanethiols may provide insight into the stoichiometry of the complexes involved and into mechanistic details of exchange at adatom complexes. The displacement reaction follows the JMAK2 site-saturated island growth mechanism, consistent with similar monolayer exchange reactions.

Having access to the substrate is necessary to initiate the exchange reaction, since insertion is observed predominantly at monolayer and substrate defect sites, and the insertion of a single molecule creates an adjacent molecular defect site. Furthermore, inserted **C12Se** molecules appear lattice matched to adjacent **C10** molecules due to molecule-molecule interactions. In low fraction **C12Se** monolayers, we conclude that the selenolates have adopted

thiolate-like binding configurations with the gold substrate, and as coverage increases, the disruption of ordered alkanethiolate domains appears to occur directionally. We infer from these results, that the adatom layer is ordered in the highly annealed **C10** films we employ. It has previously been shown that multiple binding configurations are close energetically, indicating that there are multiple stable possibilities for substrate attachment. The low energy barbell configuration may be consistent with these results, but, future experiments with grazing angle X-ray diffraction and local barrier height imaging will be necessary to elucidate the binding configurations of **C12Se** and **C12**S [50]. Data shown here will have implications not only for the Au-S bond complexes, but also in the field of chemical patterning down to the single-molecule scale [87].

Lastly, we observed a low (≤1 eV) barrier to induced motion of **C12Se** by the STM tip at positive sample bias, where electrons injected into empty states of the mixed monolayer film induce place-exchange reactions between the selenolates and thiolates. When in motion, adjacent sites seem to have equal probability of providing a new attachment site, assuming the substrate bond configuration is the same. The atomistic nature of this reaction remains an open question, which future conductance spectroscopy experiments can possibly answer, such as by obtaining a better understanding of bias-induced motion. We propose that application of positive sample bias induces a local thiolate to selenolate ligand exchange metathesis reaction between adjacent gold-adatom complexes. A turnstile adatom trichalcogen transitional state would account for the capacity of isolated selenolates to move through an ordered lattice without inducing extensive monolayer order.

5.4 Materials and Methods

5.4.1 Materials

The chemical 1-dodecanselenol was prepared by reduction of di(dodecyl)diselenide with $LiAlH_4$ in diethylether. After an acidic work-up, the product was purified by distillation over a 30 cm Vigreux column at a pressure of 20 hPa. Exclusion of oxygen is critical throughout each preparation step. 1-Decanethiol, 1-dodecanethiol, and absolute ethanol (nondenatured) were used as received from Sigma Aldrich. Perdeuterated 1-dodecanethiol (**D12**) is used as received from CDN Isotopes (Canada). For air-sensitive work, ethanol is degassed via freeze-pump-thawing cycles as described previously and is subsequently transferred to a sealed, gasketed bottle stored inside an oxygen-free (<1 ppm) glovebox [32]. Glassware was cleaned by immersion in fresh piranha solution (1:3 H_2O_2 and concentrated sulfuric acid; *safety warning: solutions are strongly acidic and oxidizing, reactions are energetic and improper use or disposal could result in explosion or severe burns.*) and thorough rinsing in deionized water supplied by a Milli-Q system from Millipore.

5.4.2 Preparation of Substrates and Self-Assembled Monolayers

Gold on mica substrates (Agilent) and gold on silicon (prepared by electron beam evaporation of 1000 Å Au on a 50 Å Cr adhesion layer, without breaking vacuum, at a rate of 1 Å s^{-1} onto a *p*-type silicon wafer supplied by Silicon Quest International (Santa Clara, CA) are annealed by 40 passes of a hydrogen flame (*safety warning: use appropriate engineering controls when striking a flame from a compressed fuel cylinder*) at an approximate rate of 0.5 Hz. Held at a 45° angle, the flame is struck from a quartz tip, which is passed over the substrate. Substrates for **C12** SAM fabrication are used immediately after preparation, and the time between annealing and **C12Se** fabrication is minimized. Titanium adhesion layers for gold

substrates are not suggested as the metal can peel from the substrate in response to flame exposure.

Preparation of extremely stable, well-ordered, self-assembled monolayers is achieved through control of deposition conditions. The **C10**, **C12**, and **D12** solutions are gravimetrically prepared by transferring the appropriate volume of neat liquid substance to a volumetric flask. Flasks are then filled to the appropriate volume with ethanol. A freshly flame-annealed substrate is quickly immersed in the solution. Since full monolayer coverage is achieved within milliseconds of solution contact, excess volume is withdrawn. The gold substrate is left exposed to the airspace in the vial over a small volume of residual solution. The vial is capped and placed in a furnace set to 78 °C for a minimum of 24 h and up to 5 days. Under these vapor annealing conditions, SAM domain sizes grow exceptionally large and the SAM is well ordered, conditions favorable to imaging substrate-linked structures through minimization of alkyl backbone orientational defects. Any oxidative degradation of the film is immediately healed, maintaining film quality indefinitely until just before imaging or further modification. These well-ordered films resist oxidative degradation better than films deposited rapidly or at room temperature, and thus support stable continuous imaging for several days.

Solutions of **C12Se** in ethanol are prepared in an oxygen- and water-free glovebox. Organic thiols and selenols are known to contaminate glovebox environments, so extreme care is taken to minimize clean substrate exposure to the glovebox environment. Sample transfer operations are thus conducted rapidly, typically less than 3 s. Two vials are each filled with 1 mL of ethanol degassed via freeze-pump-thaw cycles. The first vial is kept sealed, and is held in reserve for a later rinsing step. One microliter of **C12Se** is added to the first vial. A 5-min purge procedure is then performed on the glovebox environment. A freshly annealed substrate is placed

in a gasketed vial, which has been briefly purged with a stream of nitrogen prior to sealing. The sample is then transferred to the glovebox, removed from the vial, and quickly immersed in the **C12Se** solution for 24 h. At the end of the immersion, the sample is removed from **C12Se** solution and placed immediately into the vial of neat ethanol, which is removed from the glovebox. The film is not air sensitive, and is then rinsed with neat ethanol and dried with nitrogen.

For molecular exchange experiments, the prefabricated initial sample is placed in a solution of the specified concentration for the specified time. Exchange by **C12Se** is performed under inert atmosphere inside the glovebox, and exchange by **C10**, **C12**, or **D12** is performed under atmospheric conditions.

5.4.3 Scanning Tunneling Microscopy Measurements

Images were collected on a custom-built beetle-style STM in atmospheric air and at room temperature, as described previously [112]. The Pt/Ir 90:10 tip wire was supplied by Alfa Aesar (Ward Hill, MA). Gains for the piezoelectric scanners were calibrated by comparing a **C10** monolayer on Au{111} to its known lattice constant of 4.99 Å. To ensure low drift, the STM tip is held in tunneling for as long as several days. Imaging of **C12Se** films is dependent on tip state, which can change during imaging. Values reported were for stable and reproducible tips that could generally persist for several days. If a tip states changed frequently, a new tip was either cut right away, or the instrument was left tunneling for several hours.

5.4.4 Infrared Reflectance Absorption Spectroscopy Measurements

Infrared spectra were collected using a Nicolet 8700 equipped with a Seagull variable angle reflection accessory, (Harrick Scientific, Inc., Ossining, NY). A FTIR Purge Gas Generator (Parker-Balston, Cleveland, OH) was used to purge the spectrometer and its accessory. Data

were collected at a grazing incidence angle of 84° relative to sample normal, with a resolution of 4 cm^{-1}. Each spectrum was averaged over 512-1024 multiplexed scans. For fractional coverage determination, samples were held in 1 mM exchange solution (typically ethanolic **C12SeH**) for 24 h to provide a 100% selenolate coverage substrate having identical reflective properties as those used for kinetic experiments. As a result, absolute coverage in the kinetic experiments increases slightly in that time. This small source of systematic error results in the observed kinetic trend of sub-100% maximum within the kinetic experimental time scale.

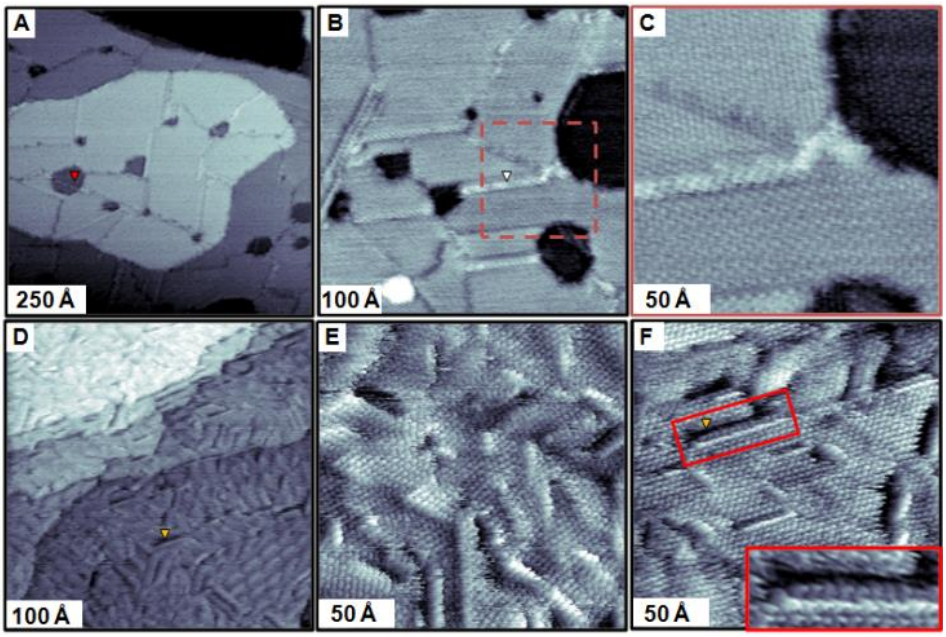

Figure 5.1: Comparison of scanning tunneling microscope images of single-component 1-decanethiolate (**C10**, top) and 1-dodecaneselenolate (**C12Se**, bottom) self-assembled monolayers on Au{111} obtained at a V_S = -1 V and I_T = 3 pA. **(A)-(C)** Image of an annealed **C10** monolayer that is highly ordered, with large domains. Important defect sites are shown, including roughly circular vacancy island substrate defects (red arrow, **(A)** and linear domain boundaries SAM defects (white arrow, **(B)**) that appear either more or less protruding than the surrounding lattice. **(C)** High-resolution image of the enclosed region from image (B). **(D)-(F)** The **C12Se** monolayer is ordered locally, but shows local variations in apparent height. The periodicity of the variation gives rise to the apparent Moiré pattern (visible in the lower right section of image (D) [26]. The features align with the underlying substrate, with linear features rotated with respect to one another in integer multiples of 30°. **(F)** Vacancy islands in single-component **C12Se** SAMs are observed, henceforth described as vacancy trenches, presenting as narrow, linear depressions aligned with the close-packed direction of the substrate (examples denoted with the yellow arrows, (D) and (F). Vacancy trenches are often accompanied by a pair of **C12Se** molecular rows, which appear to be depressed or protruding from the median terrace height by -1 or +1 Å, respectively. The inset shows an expanded view of the region bounded by the red box. The median trench apparent height is ~2.3 Å lower than the median terrace apparent height, reflecting a monatomic step of the gold substrate surface.

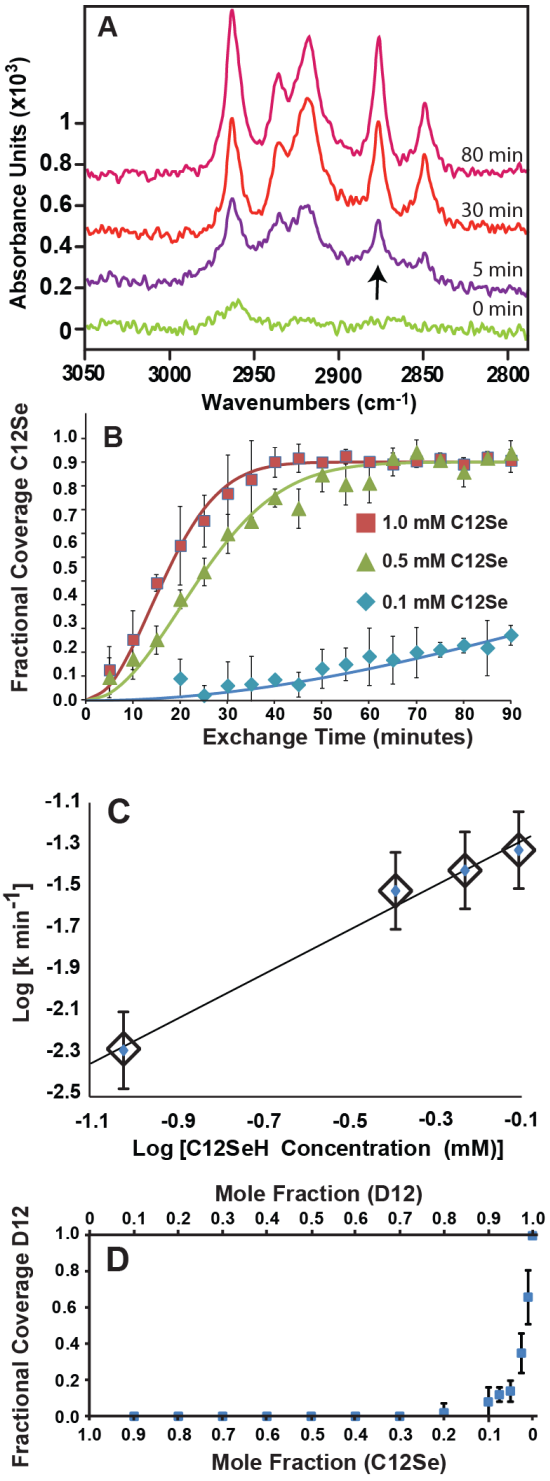

Figure 5.2: Tracking the exchange of perdeuterated 1-dodecanethiol (**D12**) by 1-dodecaneselenol (**C12Se**) via infrared reflectance absorption spectroscopy (IRRAS). **(A)** Evolution of the **C12Se** spectrum as it displaces the **D12** film. Spectral interference was eliminated by employing the deuterated species. The coverage indicator is the 2877 cm^{-1} methyl symmetric stretch, denoted by the black arrow. After 90 min, the reaction reaches completion and no further exchange occurs. **(B)** Kinetic experiments tracking the progression of the

exchange reaction between a preformed **D12** film and **C12Se** in solution. Data is fit to a site-saturated JMAK2 (Johnson, Mehl, Avrami, and Kolmogorov) model for perimeter dependent island growth [57]. **(C)** Rate constant of displacement versus **C12Se** concentration on a logarithmic scale has a slope of ~1, indicating that the rate constant is directly proportional to the concentration of **C12Se**. **(D)** Codeposition studies of **D12** with **C12Se** signifying the preference for **C12Se** in mixed monolayers. **C12Se** dominates film coverage until the mole fraction approaches 100:1 in favor of **D12**.

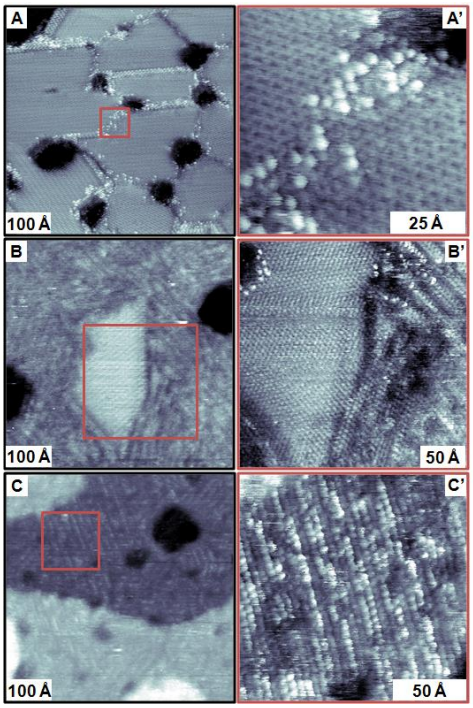

Figure 5.3: Scanning tunneling micrographs of mixed thiolate/selenolate SAMs on Au{111}, obtained at V_S = -1 V and I_T = 1 pA. **(A, A')** Short exposure (1 min) of a **C10** SAM to a 10 mM ethanolic **C12Se** solution, resulting in adsorption at defect sites (step edges and domain boundaries). The **C12Se** molecules appear to protrude from the **C10** lattice by approximately ~0.7 Å in STM images under these conditions. **(B, B')** Longer exposure (4 min) resulted in extensive molecular exchange with **C12Se**, replacing **C10** under these conditions. The relative apparent heights of the two species are reversed; the thiolates appear to protrude from the predominantly **C12Se** lattice by ~0.7 Å in STM images. In (**B'**), features at three different apparent heights can be observed in a single image; **C12Se** molecules (top left) appear to protrude from the **C10** island by ~0.7 Å, while the island appears ~0.7 Å more protruding than nearby striped **C12Se**. Some intercalation of **C10** within the **C12Se** striped phase cannot be excluded. (**C, C'**) After 10 min of exposure, no **C10** molecules are observed, leaving only a striped phase of single-component **C12Se**.

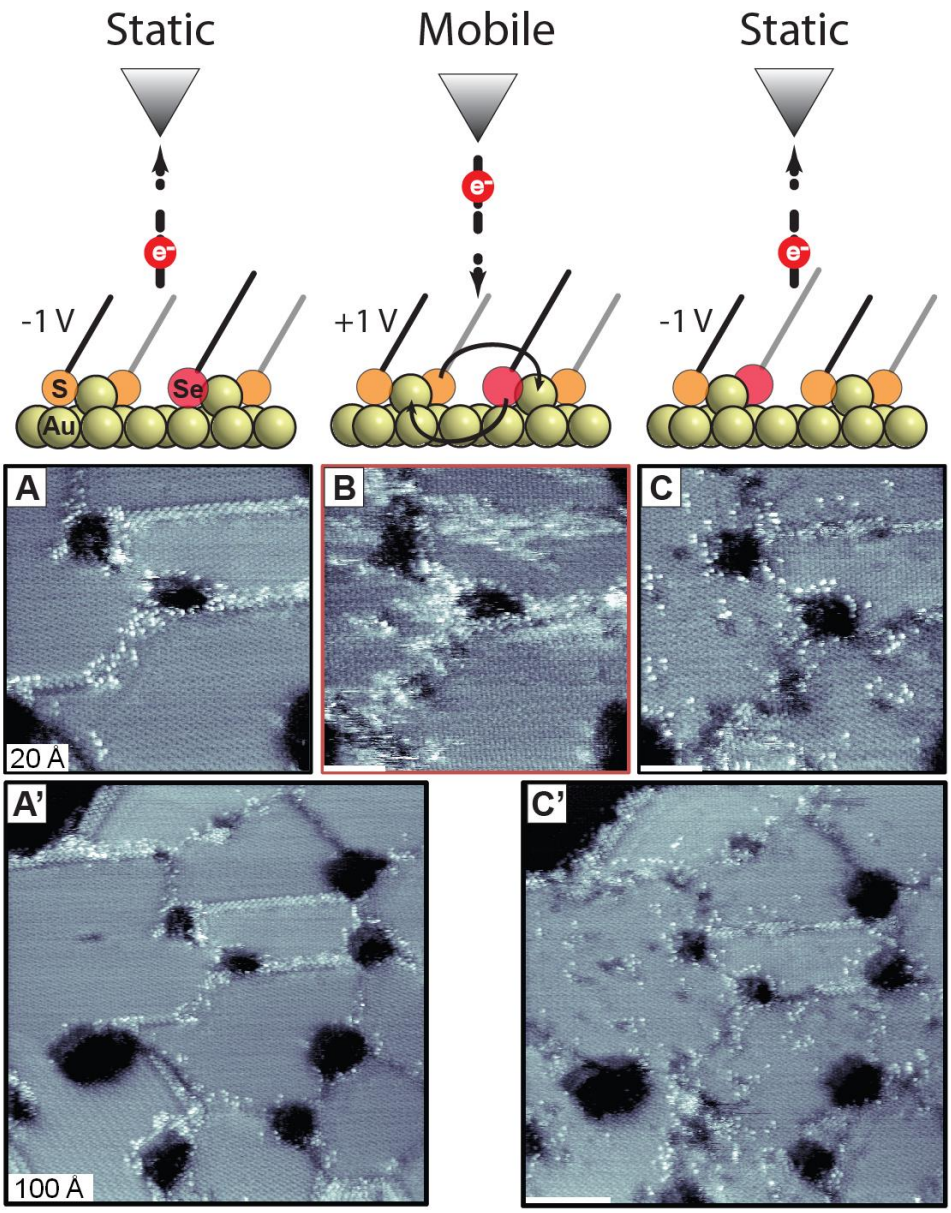

Figure 5.4: (Top) Schematic depicting direction of electron flow, sample bias, and the reaction taking place between the gold (yellow circles) complex of selenolates (red circles), and thiolates (orange circles). The grey and black lines depict alkyl chains. **(Bottom)** A sequence of images showing the effect of induced motion of **C12Se** in **C10** self-assembled monolayer. **(A** and **A')** Scanning tunneling micrographs of **C12Se** molecules (appear protruding) inserted predominantly at step edges and domain boundaries. Images were recorded at V_S = -1 V and I_T = 3 pA. **(B)** Image depicting the same region after reversal of the sample bias to +1 V. This reversal of bias polarity induces motion that enables **C12Se** to exchange positions with neighboring **C10**. Place-exchange reactions occur faster than image acquisition, so the STM probe is no longer able to record the precise position of the selenolates [103, 104]. **(C** and **C')** Returning to -1 V sample bias arrests the tip-induced motion of selenolates. Protruding molecules are observed in ordered **C10** domains, having diffused several nanometers while the region was imaged at +1 V sample bias. The large scan area as shown in image (C'), reveals that the motion of **C12Se** is induced at distances up to 50 nm from the tip position.

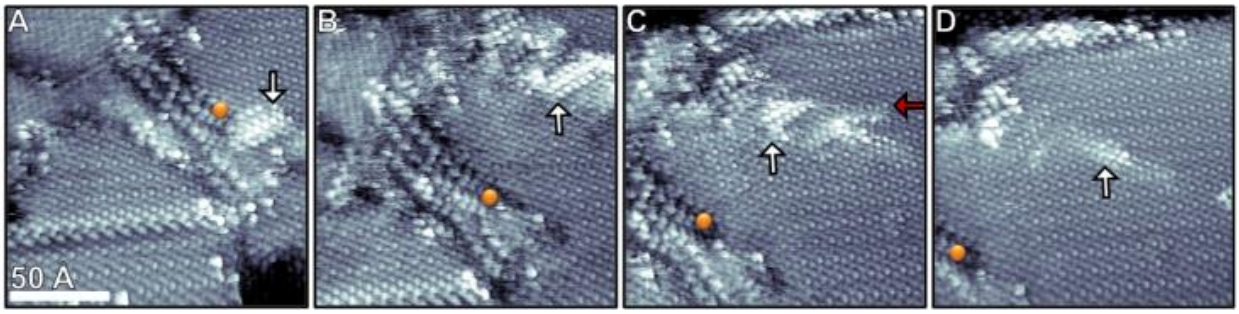

Figure 5.5: A short voltage pulse is applied over a **C12Se** cluster (V_S = +1 V, I_T = 3 pA, 5 s) inducing 2D place-exchange reactions. Protruding molecules are attributed to 1-dodecaneselenolates in a 1-dodecanethiolate matrix. The pulse target, denoted by the orange circle, is labeled to account for drift over image acquisition times in excess of 5 min. The cluster denoted by the white arrow was the target of the voltage pulse. **(B)** Subsequent images show how the cluster is displaced as a group and its evolution over time. **(C)** This feature appears stable, and is then truncated all of a sudden at the image line denoted by the red arrow, indication of motion faster than the imaging timescale. **(D)** Subsequent images revealing continued changes in relative heights, with molecules likely drawn out of the field of view. The shift in the image frame is due to drift over long image acquisition times (~5 min/frame).

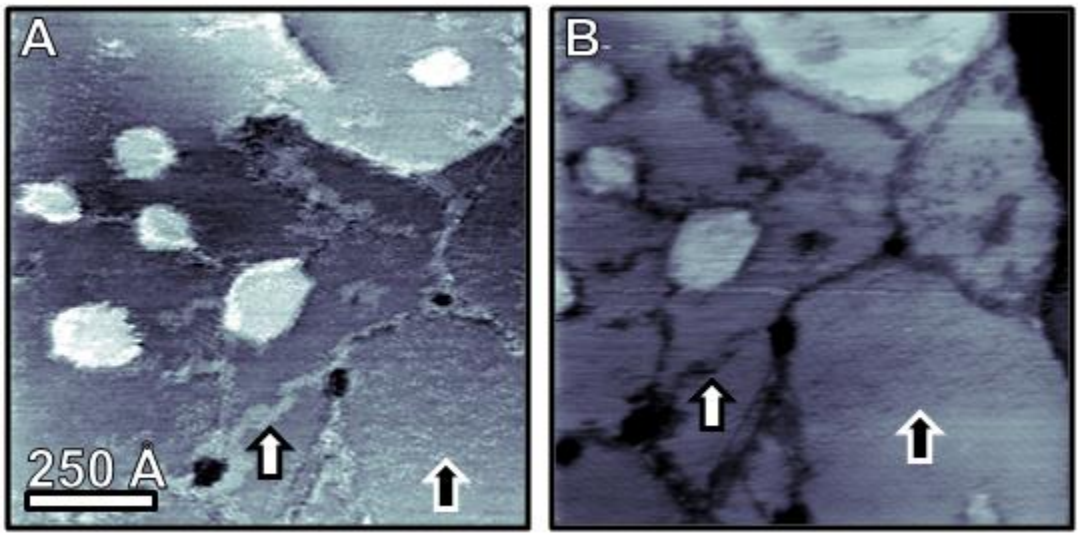

Figure 5.6: Distribution of selenolate exchange and tip dependence of apparent height. **(A)** Dodecaneselenolates inserted predominantly at decanethiolate SAM matrix defects appear protruding relative to the surrounding thiolates. In this example, insertion occurs at domain boundaries (white arrow), step edges, and within ordered domains, attributed to insertion at molecular vacancies (black arrow). **(B)** Tip state change after continuous imaging resulted in inverted contrast for the two molecular species. Both insertion at domain boundaries and within the domain appear less protruding than the surrounding decanethiolate matrix. Tip state changes occur randomly, and grow more common as SAM order decreases and with repeated sample bias reversal experiments. It is important to assign molecular identities carefully as such tip changes can give a false representation of molecular motion and SAM dynamics.

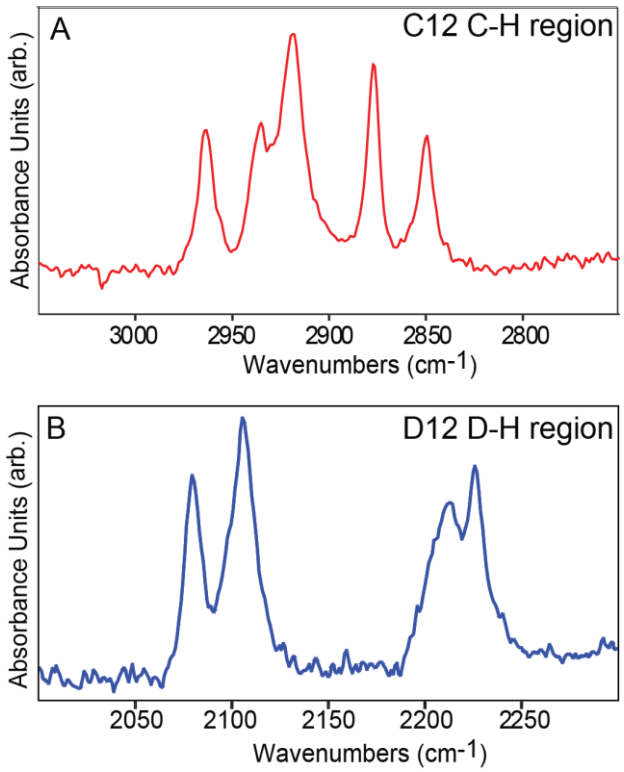

Figure 5.7: (A) Carbon-hydrogen stretches for 1-dodecanethiolate **(C12)** and **(B)** carbon-deuterium stretches for perdeuterated 1-dodecanethiolate **(D12).**

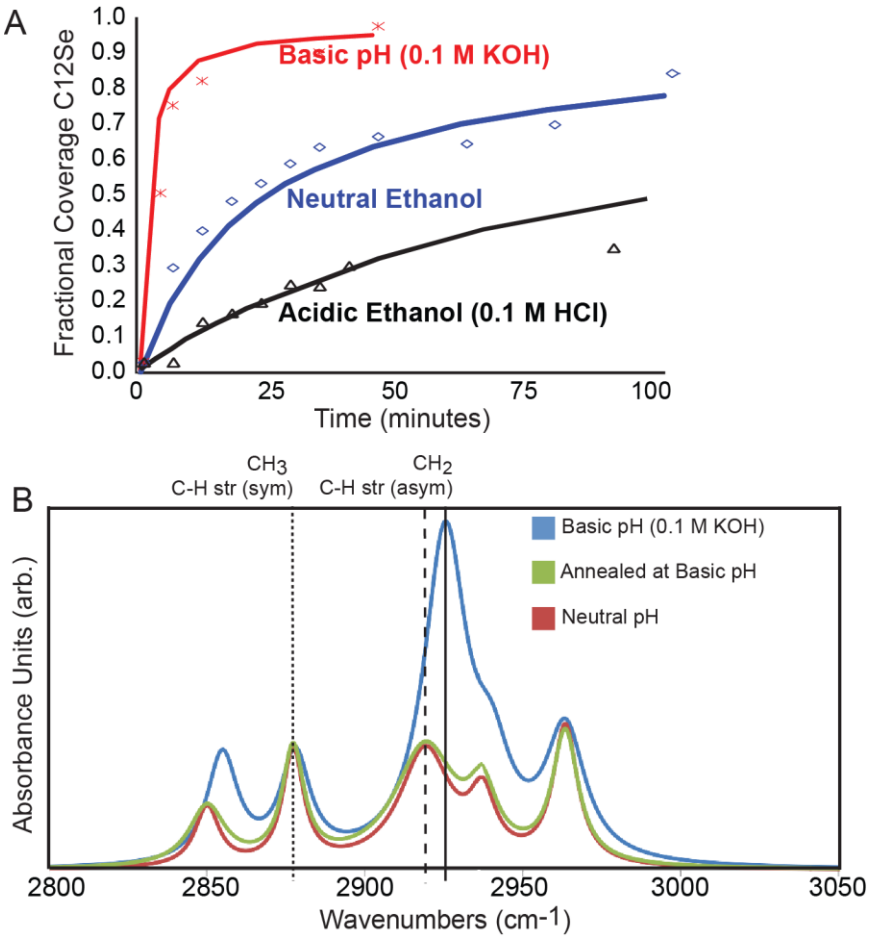

Figure 5.8: Effect of solution pH on perdeuterated 1-dodecanethiolate (**D12**) SAM exchange by 1-dodecaneselenol (**C12Se**) at 1 mM. **(A)** Addition of aqueous KOH to 1 mM ethanolic **C12Se** noticeably increases displacement rate, whereas similar addition of aqueous hydrochloric acid reduces the rate of exchange. **(B)** Infrared reflectance spectra of the C-H region after 1 h base-catalyzed **C12Se** displacement (blue trace) compared to 24-h displacement at neutral pH. The methyl symmetric stretch at 2871 cm^{-1} has similar intensity, attributed to similar absolute coverage. Annealing at elevated temperatures in basic solution for 24 h, results in a **C12Se** film largely indistinguishable from the neutral pH control sample. This is further evidence that base-catalyzed exchange disrupts film structure but does not substantially affect the underlying gold substrate.

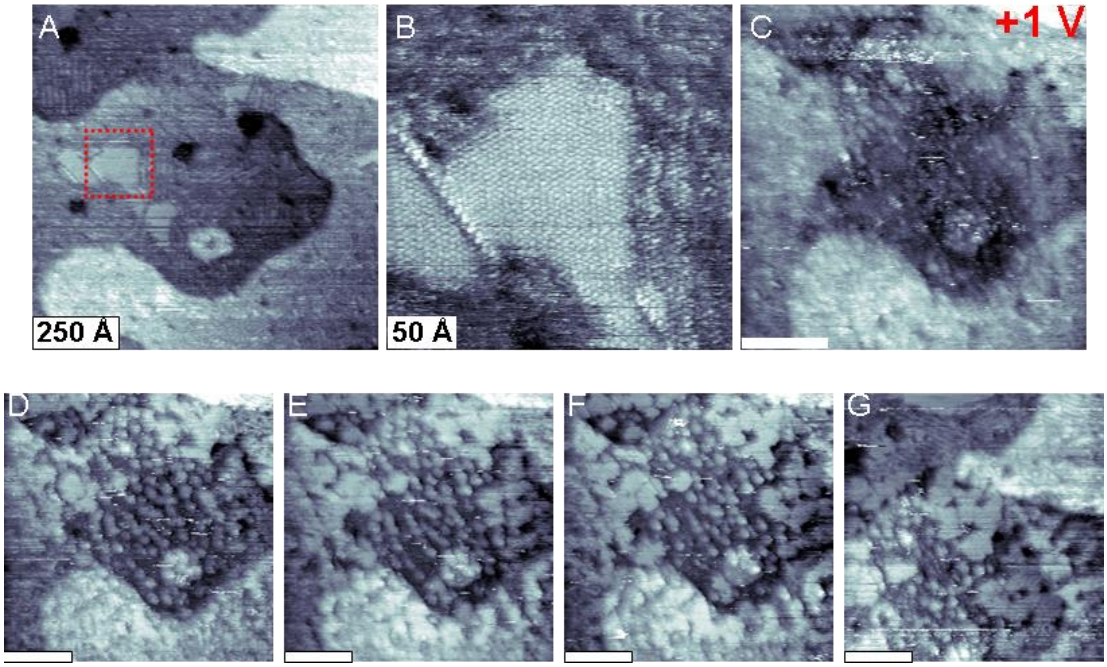

Figure 5.9: Imaging at positive bias at high relative **C12Se** coverage (>25%) results in large-area reconfiguration of the monolayer structure. **(A)** Islands of pristine **C10** remain after significant **C12Se** displacement, as enclosed in the red square. **(B)** High-resolution view of the **C10** island in (A). **(C)** Imaging at +1 V sample bias results in a decrease in image resolution, consistent with molecular motion and place exchange between alkanethiolate and alkaneselenolate. **(D)** Returning to -1 V sample bias reveals a scrambled interface. The discrete **C10** islands and striped features have been replaced with a mottled structure. **(E)-(G)** Continued imaging reveals motion and reconfiguration of the domains in the image. With the exception of (C), images were recorded at V_S = -1 V and I_T = 3 pA. Images (C)-(G) shares the same scale as image (A).

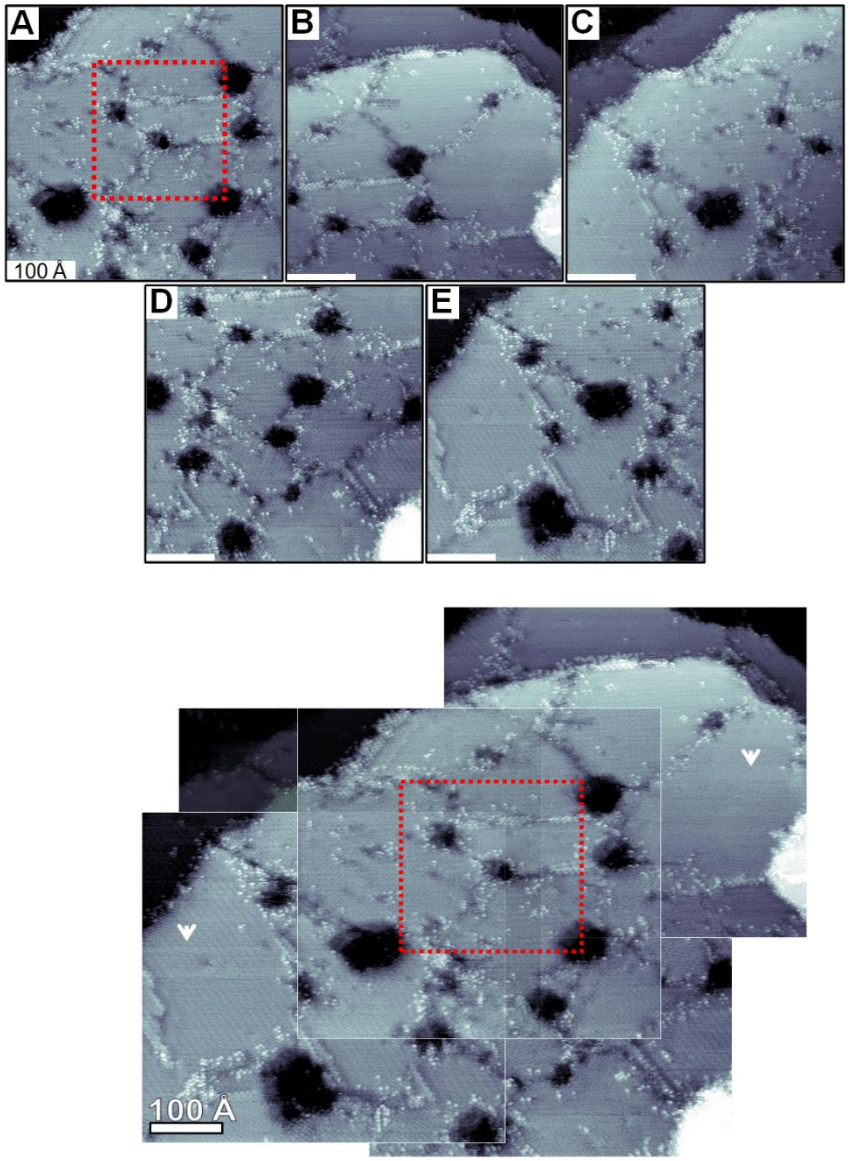

Figure 5.10: Images and aligned composites reveal spatial distributions of molecules induced to move via tip-induced place-exchange reactions. **(A)** The region highlighted by the red square at image center is the region scanned at +1 V sample bias for full image acquisition time (~5 min). Protruding **C12Se** molecules are found in different positions after imaging at +1 V. Domains that are at least 250 Å from the center of the imaged area are largely undisturbed by positive bias imaging, as indicated by the white arrows denoting pristine domains in the composite image (left and right).

5.5 References

1. Stranick, S. J.; Parikh, A. N.; Allara, D. L.; Weiss, P. S. A new mechanism for surface diffusion: motion of a substrate-adsorbate complex. *J. Phys. Chem.* **1994**, *98*, 11136-11142.

2. Maksymovych, P.; Sorescu, D. C.; Yates, J. T. Gold-adatom-mediated bonding in self-assembled short-chain alkanethiolate species on the Au(111) surface. *Phys. Rev. Lett.* **2006**, *97*, 146103.

3. Yu, M.; Bovet, N.; Satterley, C. J.; Bengio, S.; Lovelock, K. R. J.; Milligan, P. K.; Jones, R. G.; Woodruff, D. P.; Dhanak, V. True nature of an archetypal self-assembly system: Mobile Au-thiolate species on Au(111). *Phys. Rev. Lett.* **2006**, *97*, 166102.

4. Jadzinsky, P. D.; Calero, G.; Ackerson, C. J.; Bushnell, D. A.; Kornberg, R. D. Structure of a thiol monolayer-protected gold nanoparticle at 1.1 Å resolution. *Science* **2007**, *318*, 430-433.

5. Mazzarello, R.; Cossaro, A.; Verdini, A.; Rousseau, R.; Casalis, L.; Danisman, M. F.; Floreano, L.; Scandolo, S.; Morgante, A.; Scoles, G. Structure of a CH_3S monolayer on Au(111) solved by the interplay between molecular dynamics calculations and diffraction measurements. *Phys. Rev. Lett.* **2007**, *98*, 4.

6. Maksymovych, P.; Yates, J. T. Au adatoms in self-assembly of benzenethiol on the Au(111) surface. *J. Am. Chem. Soc.* **2008**, *130*, 7518-7519.

7. Cossaro, A.; Mazzarello, R.; Rousseau, R.; Casalis, L.; Verdini, A.; Kohlmeyer, A.; Floreano, L.; Scandolo, S.; Morgante, A.; Klein, M. L.; Scoles, G. X-ray diffraction and computation yield the structure of alkanethiols on gold(111). *Science* **2008**, *321*, 943-946.

8. Kautz, N. A.; Kandel, S. A. Alkanethiol/Au(111) Self-assembled monolayers contain gold adatoms: scanning tunneling microscopy before and after reaction with atomic hydrogen. *J. Am. Chem. Soc.* **2008**, *130*, 6908-6909.

9. Voznyy, O.; Dubowski, J. J.; Yates, J. T.; Maksymovych, P. The role of gold adatoms and stereochemistry in self-assembly of methylthiolate on Au(111). *J. Am. Chem. Soc.* **2009**, *131*, 12989-12993.

10. Kautz, N. A.; Kandel, S. A. Alkanethiol monolayers contain gold adatoms, and adatom coverage is independent of chain length. *J. Phys. Chem. C* **2009**, *113*, 19286-19291.

11. Qian, H.; Eckenhoff, W. T.; Zhu, Y.; Pintauer, T.; Jin, R. Total structure determination of thiolate-protected Au_{38} nanoparticles. *J. Am. Chem. Soc.* **2010**, *132*, 8280-8281.

12. Liu, Y.; Ozolins, V. Self-assembled monolayers on Au(111): structure, energetics, and mechanism of reconstruction lifting. *J. Phys. Chem. C* **2012**, *116*, 4738-4747.

13. Hakkinen, H. The gold-sulfur interface at the nanoscale. *Nat. Chem.* **2012**, *4*, 443-455.

14. Knoppe, S.; Dolamic, I.; Bürgi, T. Racemization of a chiral nanoparticle evidences the flexibility of the gold-thiolate interface. *J. Am. Chem. Soc.* **2012**, *134*, 13114-13120.

15. Fan, X.; Zhang, C.; Liu, Y.; Lau, W. M. Effects of intrinsic surface defects on thiophenol self-assembly on au(111): surface structures and reaction mechanisms. *J. Phys. Chem. C* **2012**, *116*, 19909-19917.

16. Moore, A. M.; Mantooth, B. A.; Donhauser, Z. J.; Yao, Y. X.; Tour, J. M.; Weiss, P. S. Real-time measurements of conductance switching and motion of single oligo(phenylene ethynylene) molecules. *J. Am. Chem. Soc.* **2007**, *129*, 10352-10353.

17. Poirier, G. E. Mechanism of formation of Au vacancy islands in alkanethiol monolayers on Au(111). *Langmuir* **1997**, *13*, 2019-2026.

18. Akihiro, N.; Yoshitada, M. Adsorption states of methylthiolate on the Au(111) surface. *J. Phys.: Condens. Matter* **2007**, *19*, 365245.

19. Jewell, A. D.; Tierney, H. L.; Sykes, E. C. H. Gently lifting gold's herringbone reconstruction: Trimethylphosphine on Au(111). *Phys. Rev. B* **2010**, *82*, 205401.

20. Schlenoff, J. B.; Li, M.; Ly, H. Stability and self-exchange in alkanethiol monolayers. *J. Am. Chem. Soc.* **1995**, *117*, 12528-12536.

21. Shon, Y. S.; Lee, T. R. Desorption and exchange of self-assembled monolayers (SAMs) on gold generated from chelating alkanedithiols. *J. Phys. Chem. B* **2000**, *104*, 8192-8200.

22. Moore, A. M.; Mantooth, B. A.; Donhauser, Z. J.; Maya, F.; Price, D. W.; Yao, Y. X.; Tour, J. M.; Weiss, P. S. Cross-step place-exchange of oligo(phenylene-ethynylene) molecules. *Nano Lett.* **2005**, *5*, 2292-2297.

23. Kassam, A.; Bremner, G.; Clark, B.; Ulibarri, G.; Lennox, R. B. Place exchange reactions of alkyl thiols on gold nanoparticles. *J. Am. Chem. Soc.* **2006**, *128*, 3476-3477.

24. Patole, S. N.; Baddeley, C. J.; O'Hagan, D.; Richardson, N. V. Reversible exchange of self-assembled monolayers of semifluorinated *n*-alkanethiols and *n*-alkanethiols on Au/mica surfaces. *J. Phys. Chem. C* **2008**, *112*, 13997-14000.

25. Ballav, N.; Terfort, A.; Zharnikov, M. Mixing of nonsubstituted and partly fluorinated alkanethiols in a binary self-assembled monolayer. *J. Phys. Chem. C* **2009**, *113*, 3697-3706.

26. Monnell, J. D.; Stapleton, J. J.; Jackiw, J. J.; Dunbar, T.; Reinerth, W. A.; Dirk, S. M.; Tour, J. M.; Allara, D. L.; Weiss, P. S. Ordered local domain structures of decaneselenolate and dodecaneselenolate monolayers on Au{111}. *J. Phys. Chem. B* **2004**, *108*, 9834-9841.

27. Monnell, J. D.; Stapleton, J. J.; Dirk, S. M.; Reinerth, W. A.; Tour, J. M.; Allara, D. L.; Weiss, P. S. Relative conductances of alkaneselenolate and alkanethiolate monolayers on Au{111}. *J. Phys. Chem. B* **2005**, *109*, 20343-20349.

28. Bashir, A.; Käfer, D.; Müller, J.; Wöll, C.; Terfort, A.; Witte, G. Selenium as a key element for highly ordered aromatic self-assembled monolayers. *Angew. Chem., Int. Ed.* **2008**, *47*, 5250-5252.

29. Cyganik, P.; Szelagowska-Kunstman, K.; Terfort, A.; Zharnikov, M. Odd-even effect in molecular packing of biphenyl-substituted alkaneselenolate self-assembled monolayers on Au(111): Scanning tunneling microscopy study. *J. Phys. Chem. C* **2008**, *112*, 15466-15473.

30. Track, A. M.; Rissner, F.; Heimel, G.; Romaner, L.; Käfer, D.; Bashir, A.; Rangger, G. M.; Hofmann, O. T.; Bucko, T.; Witte, G.; Zojer, E. Simultaneously understanding the geometric and electronic structure of anthraceneselenolate on Au(111): A combined theoretical and experimental study. *J. Phys. Chem. C* **2010**, *114*, 2677-2684.

31. Weidner, T.; Ballav, N.; Grunze, M.; Terfort, A.; Zharnikov, M. Modification of biphenylselenolate monolayers by low-energy electrons. *Phys. Status Solidi B* **2009**, *246*, 1519-1528.

32. Hohman, J. N.; Kim, M.; Schüpbach, B.; Kind, M.; Thomas, J. C.; Terfort, A.; Weiss, P. S. Dynamic double lattice of 1-adamantaneselenolate self-assembled monolayers on Au{111}. *J. Am. Chem. Soc.* **2011**, *133*, 19422-19431.

33. Yokota, K.; Taniguchi, M.; Tsutsui, M.; Kawai, T. Molecule-electrode bonding design for high single-molecule conductance. *J. Am. Chem. Soc.* **2011**, *132*, 17364-17365.

34. Cometto, F. P.; Patrito, E. M.; Paredes Olivera, P.; Zampieri, G.; Ascolani, H. electrochemical, high-resolution photoemission spectroscopy and vdW-DFT study of the thermal stability of benzenethiol and benzeneselenol monolayers on Au(111). *Langmuir* **2012**, *28*, 13624-13635.

35. Kurashige, W.; Yamaguchi, M.; Nobusada, K.; Negishi, Y. Ligand-induced stability of gold nanoclusters: thiolate versus selenolate. *J. Phys. Chem. Lett.* **2012**, *3*, 2649-2652.

36. Pathem, B. K.; Claridge, S. A.; Zheng, Y. B.; Weiss, P. S. Molecular switches and motors on surfaces. *Annu. Rev. Phys. Chem.* **2013**, *64*, 605-630.

37. Romashov, L. V.; Ananikov, V. P. Self-assembled selenium monolayers: from nanotechnology to materials science and adaptive catalysis. *Chem. Eur. J.* **2013**, *19*, 17640-17660.

38. Huang, F. K.; Horton, R. C.; Myles, D. C.; Garrell, R. L. Selenolates as alternatives to thiolates for self-assembled monolayers: A SERS study. *Langmuir* **1998**, *14*, 4802-4808.

39. Szelągowska-Kunstman, K.; Cyganik, P.; Schupbach, B.; Terfort, A. Relative stability of thiol and selenol based SAMs on Au(111) - exchange experiments. *Phys. Chem. Chem. Phys.* **2010**, *12*, 4400-4406.

40. Stipe, B. C.; Rezaei, M. A.; Ho, W. Single-molecule vibrational spectroscopy and microscopy. *Science* **1998**, *280*, 1732-1735.

41. Bumm, L. A.; Arnold, J. J.; Dunbar, T. D.; Allara, D. L.; Weiss, P. S. Electron transfer through organic molecules. *J. Phys. Chem. B* **1999**, *103*, 8122-8127.

42. Weiss, P. S.; Eigler, D. M. Site dependence of the apparent shape of a molecule in scanning tunneling micoscope images: Benzene on Pt{111}. *Phys. Rev. Lett.* **1993**, *71*, 3139-3142.

43. Donhauser, Z. J.; Mantooth, B. A.; Kelly, K. F.; Bumm, L. A.; Monnell, J. D.; Stapleton, J. J.; Price, D. W.; Rawlett, A. M.; Allara, D. L.; Tour, J. M.; Weiss, P. S. Conductance switching in single molecules through conformational changes. *Science* **2001**, *292*, 2303-2307.

44. Camillone, N.; Eisenberger, P.; Leung, T. Y. B.; Schwartz, P.; Scoles, G.; Poirier, G. E.; Tarlov, M. J. New monolayer phases of n-alkanethiols self-assembled on Au(111) – preparation, surface characterization, and imaging. *J. Chem. Phys.* **1994**, *101*, 11031-11036.

45. Poirier, G. E.; Tarlov, M. J. The *c*(4 × 2) superlattice of *n*-alkanethiol monolayers self-assembled on Au(111). *Langmuir* **1994**, *10*, 2853-2856.

46. Poirier, G. E. Characterization of organosulfur molecular monolayers on Au(111) using scanning tunneling microscopy. *Chem. Rev.* **1997**, *97*, 1117-1127.

47. Weiss, P. S. functional molecules and assemblies in controlled environments: formation and measurements. *Acc. Chem. Res.* **2008**, *41*, 1772-1781.

48. Love, J. C.; Estroff, L. A.; Kriebel, J. K.; Nuzzo, R. G.; Whitesides, G. M. Self-assembled monolayers of thiolates on metals as a form of nanotechnology. *Chem. Rev.* **2005**, *105*, 1103-1169.

49. Bent, S. F. Heads or tails: Which is more important in molecular self-assembly? *ACS Nano* **2007**, *1*, 10-12.

50. Han, P.; Kurland, A. R.; Giordano, A. N.; Nanayakkara, S. U.; Blake, M. M.; Pochas, C. M.; Weiss, P. S. Heads and tails: simultaneous exposed and buried interface imaging of monolayers. *ACS Nano* **2009**, *3*, 3115-3121.

51. Choi, J.; Lee, Y. J.; Kang, H.; Han, J. W.; Noh, J. Self-assembled monolayers of dioctyl diselenides on au(111). *Bull. Korean Chem. Soc.* **2008**, *29*, 1229-1232.

52. Yang, G.; Liu, G.-y. New insights for self-assembled monolayers of organothiols on Au(111) revealed by scanning tunneling microscopy. *J. Phys. Chem. B* **2003**, *107*, 8746-8759.

53. de la Llave, E.; Scherlis, D. A. Selenium-based self-assembled monolayers: The nature of adsorbate-surface interactions. *Langmuir* **2010**, *26*, 173-178.

54. Dameron, A. A.; Charles, L. F.; Weiss, P. S. Structures and displacement of 1-adamantanethiol self-assembled monolayers on Au{111}. *J. Am. Chem. Soc.* **2005**, *127*, 8697-8704.

55. Dameron, A. A.; Mullen, T. J.; Hengstebeck, R. W.; Saavedra, H. M.; Weiss, P. S. Origins of displacement in 1-adamantanethiolate self-assembled monolayers. *J. Phys. Chem. C* **2007**, *111*, 6747-6752.

56. Mullen, T. J.; Dameron, A. A.; Saavedra, H. M.; Williams, M. E.; Weiss, P. S. Dynamics of solution displacement in 1-adamantanethiolate self-assembled monolayers. *J. Phys. Chem. C* **2007**, *111*, 6740-6746.

57. Saavedra, H. M.; Barbu, C. M.; Dameron, A. A.; Mullen, T. J.; Crespi, V. H.; Weiss, P. S. 1-adamantanethiolate monolayer displacement kinetics follow a universal form. *J. Am. Chem. Soc.* **2007**, *129*, 10741-10746.

58. Bumm, L. A.; Arnold, J. J.; Cygan, M. T.; Dunbar, T. D.; Burgin, T. P.; Jones, L.; Allara, D. L.; Tour, J. M.; Weiss, P. S. Are single molecular wires conducting? *Science* **1996**, *271*, 1705-1707.

59. Cygan, M. T.; Dunbar, T. D.; Arnold, J. J.; Bumm, L. A.; Shedlock, N. F.; Burgin, T. P.; Jones, L.; Allara, D. L.; Tour, J. M.; Weiss, P. S. Insertion, conductivity, and structures of conjugated organic oligomers in self-assembled alkanethiol monolayers on Au{111}. *J. Am. Chem. Soc.* **1998**, *120*, 2721-2732.

60. Donhauser, Z. J.; Price, D. W.; Tour, J. M.; Weiss, P. S. Control of alkanethiolate monolayer structure using vapor-phase annealing. *J. Am. Chem. Soc.* **2003**, *125*, 11462-11463.

61. Weck, M.; Jackiw, J. J.; Rossi, R. R.; Weiss, P. S.; Grubbs, R. H. Ring-opening metathesis polymerization from surfaces. *J. Am. Chem. Soc.* **1999**, *121*, 4088-4089.

62. Kim, M.; Hohman, J. N.; Cao, Y.; Houk, K. N.; Ma, H.; Jen, A. K.-Y.; Weiss, P. S. Creating favorable geometries for directing organic photoreactions in alkanethiolate monolayers. *Science* **2011**, *331*, 1312-1315.

63. Zheng, Y. B.; Pathem, B. K.; Hohman, J. N.; Thomas, J. C.; Kim, M.; Weiss, P. S. Photoresponsive molecules: photoresponsive molecules in well-defined nanoscale environments. *Adv. Mater.* **2013**, *25*, 293-293.

64. Poirier, G. E.; Tarlov, M. J.; Rushmeier, H. E. 2-Dimensional liquid-phase and the $p \times \sqrt{3}$ phase of alkanethiol self-assembled monolayers on Au(111). *Langmuir* **1994**, *10*, 3383-3386.

65. Dishner, M. H.; Feher, F. J.; Hemminger, J. C. Formation and photooxidation of n-dodecanethiol self-assembled monolayers on Au(111): 'Pits' formed during chemisorption disappear upon oxidation. *Chem. Commun.* **1996**, 1971-1972.

66. Smith, R. K.; Lewis, P. A.; Weiss, P. S. Patterning self-assembled monolayers. *Prog. Surf. Sci.* **2004**, *75*, 1-68.

67. Yang, G.; Amro, N. A.; Starkewolfe, Z. B.; Liu, G.-y. Molecular-level approach to inhibit degradations of alkanethiol self-assembled monolayers in aqueous media. *Langmuir* **2004**, *20*, 3995-4003.

68. Stranick, S. J.; Parikh, A. N.; Allara, D. L.; Weiss, P. S. A new mechanism for surface-diffusion - motion of a substrate-adsorbate complex. *J. Phys. Chem.* **1994**, *98*, 11136-11142.

69. Kim, M.; Hohman, J. N.; Morin, E. I.; Daniel, T. A.; Weiss, P. S. Self-assembled monolayers of 2-adamantanethiol on Au{111}: Control of structure and displacement. *J. Phys. Chem. A* **2009**, *113*, 3895-3903.

70. Saavedra, H. M.; Thompson, C. M.; Hohman, J. N.; Crespi, V. H.; Weiss, P. S. Reversible lability by in situ reaction of self-assembled monolayers. *J. Am. Chem. Soc.* **2009**, *131*, 2252-2259.

71. Saavedra, H. M.; Mullen, T. J.; Zhang, P. P.; Dewey, D. C.; Claridge, S. A.; Weiss, P. S. Hybrid strategies in nanolithography. *Rep. Prog. Phys.* **2010**, *73*, 036501.

72. Shaporenko, A.; Ulman, A.; Terfort, A.; Zharnikov, M. Self-assembled monolayers of alkaneselenolates on (111) gold and silver. *J. Phys. Chem. B* **2005**, *109*, 3898-3906.

73. Yee, C. K.; Ulman, A.; Ruiz, J. D.; Parikh, A.; White, H.; Rafailovich, M. Alkyl selenide- and alkyl thiolate-functionalized gold nanoparticles: chain packing and bond nature. *Langmuir* **2003**, *19*, 9450-9458.

74. Fonder, G.; Cecchet, F.; Peremans, A.; Thiry, P. A.; Delhalle, J.; Mekhalif, Z. Conformational order of n-dodecanethiol and n-dodecaneselenol monolayers on polycrystalline copper investigated by PM-IRRAS and SFG spectroscopy. *Surf. Sci.* **2009**, *603*, 2276-2282.

75. Fonder, G.; Delhalle, J.; Mekhalif, Z. Exchange versus intercalation of *n*-dodecanethiol monolayers on copper in the presence of n-dodecaneselenol and *vice versa*. *Appl. Surf. Sci.* **2011**, *256*, 2968-2973.

76. Aizenberg, J.; Black, A. J.; Whitesides, G. M. Controlling local disorder in self-assembled monolayers by patterning the topography of their metallic supports. *Nature* **1998**, *394*, 868.

77. Black, A. J.; Paul, K. E.; Aizenberg, J.; Whitesides, G. M. Patterning disorder in monolayer resists for the fabrication of sub-100-nm structures in silver, gold, silicon, and aluminum. *J. Am. Chem. Soc.* **1999**, *121*, 8356-8365.

78. Collard, D. M.; Fox, M. A. Use of electroactive thiols to study the formation and exchange of alkanethiol monolayers on gold. *Langmuir* **1991**, *7*, 1192-1197.

79. Baralia, G. G.; Duwez, A.-S.; Nysten, B.; Jonas, A. M. Kinetics of exchange of alkanethiol monolayers self-assembled on polycrystalline gold. *Langmuir* **2005**, *21*, 6825-6829.

80. Hohman, J. N.; Claridge, S. A.; Kim, M.; Weiss, P. S. Cage molecules for self-assembly. *Mater. Sci. Eng., R* **2010**, *70*, 188-208.

81. Kamenetska, M.; Quek, S. Y.; Whalley, A. C.; Steigerwald, M. L.; Choi, H. J.; Louie, S. G.; Nuckolls, C.; Hybertsen, M. S.; Neaton, J. B.; Venkataraman, L. Conductance and geometry of pyridine-linked single-molecule junctions. *J. Am. Chem. Soc.* **2010**, *132*, 6817-6821.

82. Hill, I. R.; Levin, I. W. Vibrational spectra and carbon--hydrogen stretching mode assignments for a series of n-alkyl carboxylic acids. *J. Chem. Phys* **1979**, *70*, 842-851.

83. Porter, M. D.; Bright, T. B.; Allara, D. L.; Chidsey, C. E. D. Spontaneously organized molecular assemblies. 4. Structural characterization of n-alkyl thiol monolayers on gold by optical ellipsometry, infrared spectroscopy, and electrochemistry. *J. Am. Chem. Soc.* **1987**, *109*, 3559-3568.

84. Nuzzo, R. G.; Dubois, L. H.; Allara, D. L. Fundamental-studies of microscopic wetting on organic-surfaces. 1. Formation and structural characterization of a self-consistent series of polyfunctional organic monolayers. *J. Am. Chem. Soc.* **1990**, *112*, 558-569.

85. Choi, J.; Kang, H.; Ito, E.; Hara, M.; Noh, J. Phase transition of octaneselenolate self-assembled monolayers on Au(111) studied by scanning tunneling microscopy. *Bull. Korean Chem. Soc.* **2011**, *32*, 2623-2627.

86. Vericat, C.; Vela, M. E.; Salvarezza, R. C. Self-assembled monolayers of alkanethiols on Au(111): surface structures, defects and dynamics. *Phys. Chem. Chem. Phys.* **2005**, *7*, 3258-3268.

87. Claridge, S. A.; Liao, W.-S.; Thomas, J. C.; Zhao, Y.; Cao, H. H.; Cheunkar, S.; Serino, A. C.; Andrews, A. M.; Weiss, P. S. From the bottom up: dimensional control and characterization in molecular monolayers. *Chem. Soc. Rev.* **2012**, *42*, 2725-2745.

88. Avrami, M. Kinetics of phase change I - General theory. *J. Chem. Phys.* **1939**, *7*, 1103-1112.

89. Avrami, M. Kinetics of phase change. II transformation-time relations for random distribution of nuclei. *J. Chem. Phys.* **1940**, *8*, 212-224.

90. Avrami, M. Kinetics of phase change. III granulation, phase change, and microstructure *J. Chem. Phys.* **1941**, *9*, 177-184.

91. Wang, Y.; Zeiri, O.; Neyman, A.; Stellacci, F.; Weinstock, I. A. Nucleation and island growth of alkanethiolate ligand domains on gold nanoparticles. *ACS Nano* **2012**, *6*, 629-640.

92. Hobara, D.; Sasaki, T.; Imabayashi, S.-i.; Kakiuchi, T. Surface structure of binary self-assembled monolayers formed by electrochemical selective replacement of adsorbed thiols. *Langmuir* **1999**, *15*, 5073-5078.

93. Mullen, T. J.; Dameron, A. A.; Weiss, P. S. Directed assembly and separation of self-assembled monolayers *via* electrochemical processing. *J. Phys. Chem. B* **2006**, *110*, 14410-14417.

94. Eigler, D. M.; Schweizer, E. K. Positioning single atoms with a scanning tunnelling microscope. *Nature* **1990**, *344*, 524-526.

95. Avouris, P.; Lyo, I.-W.; Bozso, F. Atom-resolved surface chemistry: The early steps of Si(111)-7×7 oxidation. *J. Vac. Sci. Technol. B* **1991**, *9*, 424-430.

96. Weiss, P. S.; Eigler, D. M. Adsorption and accommodation of Xe on Pt{111}. *Phys. Rev. Lett.* **1992**, *69*, 2240-2243.

97. Lyding, J. W.; Hess, K.; Abeln, G. C.; Thompson, D. S.; Moore, J. S.; Hersam, M. C.; Foley, E. T.; Lee, J.; Chen, Z.; Hwang, S. T.; Choi, H.; Avouris, P.; Kizilyalli, I. C. Ultrahigh vacuum“scanning tunneling microscopy nanofabrication and hydrogen/deuterium desorption from silicon surfaces: implications for complementary metal oxide semiconductor technology. *Appl. Surf. Sci.* **1998**, *130-132*, 221-230.

98. Liu, M.; Amro, N. A.; Liu, G.-Y. Nanografting for surface physical chemistry. *Annu. Rev. Phys. Chem.* **2008**, *59*, 367-386.

99. Luis, G. R.; Jian, L. Atomic force microscope nanolithography: dip-pen, nanoshaving, nanografting, tapping mode, electrochemical and thermal nanolithography. *J. Phys.: Condens. Matter* **2009**, *21*, 483001.

100. Liu, G.-Y.; Xu, S.; Qian, Y. Nanofabrication of self-assembled monolayers using scanning probe lithography. *Acc. Chem. Res.* **2000**, *33*, 457-466.

101. Cheung, C. L.; Camarero, J. A.; Woods, B. W.; Lin, T. W.; Johnson, J. E.; De Yoreo, J. J. Fabrication of assembled virus nanostructures on templates of chemoselective linkers formed by scanning probe nanolithography. *J. Am. Chem. Soc.* **2003**, *125*, 6848-6849.

102. Kramer, S.; Fuierer, R. R.; Gorman, C. B. Scanning probe lithography using self-assembled monolayers. *Chem. Rev.* **2003**, *103*, 4367-4418.

103. Stranick, S. J.; Kamna, M. M.; Weiss, P. S. Atomic-scale dynamics of a two-dimensional gas-solid interface. *Science* **1994**, *266*, 99-102.

104. Mantooth, B. A.; Sykes, E. C. H.; Han, P.; Moore, A. M.; Donhauser, Z. J.; Crespi, V. H.; Weiss, P. S. Analyzing the motion of benzene on Au{111}: single molecule statistics from scanning probe images. *J. Phys. Chem. C* **2007**, *111*, 6167-6182.

105. Claridge, S. A.; Schwartz, J. J.; Weiss, P. S. Electrons, photons, and force: quantitative single-molecule measurements from physics to biology. *ACS Nano* **2011**, *5*, 693-729.

106. Tarr, S.; Weiss, P. S. Very small horses: visualizing motion at the nanoscale. *Leonardo* **2012**, *45*, 439-445.

107. Nenchev, G.; Diaconescu, B.; Hagelberg, F.; Pohl, K. Self-assembly of methanethiol on the reconstructed Au(111) surface. *Phys. Rev. B* **2009**, *80*, 081401.

108. Zhu, M.; Aikens, C. M.; Hollander, F. J.; Schatz, G. C.; Jin, R. Correlating the crystal structure of a thiol-protected Au_{25} cluster and optical properties. *J. Am. Chem. Soc.* **2008**, *130*, 5883-5885.

109. Maksymovych, P.; Voznyy, O.; Dougherty, D. B.; Sorescu, D. C.; Yates, J. T. Gold adatom as a key structural component in self-assembled monolayers of organosulfur molecules on Au(111). *Prog. Surf. Sci.* **2010**, *85*, 206-240.

110. Lewis, P. A.; Donhauser, Z. J.; Mantooth, B. A.; Smith, R. K.; Bumm, L. A.; Kelly, K. F.; Weiss, P. S. Control and placement of molecules via self-assembly. *Nanotechnology* **2001**, *12*, 231-237.

111. Qian, Y.; Yang, G.; Yu, J.; Jung, T. A.; Liu, G.-Y. Structures of annealed decanethiol self-assembled monolayers on Au(111): an Ultrahigh vacuum scanning tunneling microscopy study. *Langmuir* **2003**, *19*, 6056-6065.

112. Bumm, L. A.; Arnold, J. J.; Charles, L. F.; Dunbar, T. D.; Allara, D. L.; Weiss, P. S. Directed self-assembly to create molecular terraces with molecularly sharp boundaries in organic monolayers. *J. Am. Chem. Soc.* **1999**, *121*, 8017-8021.